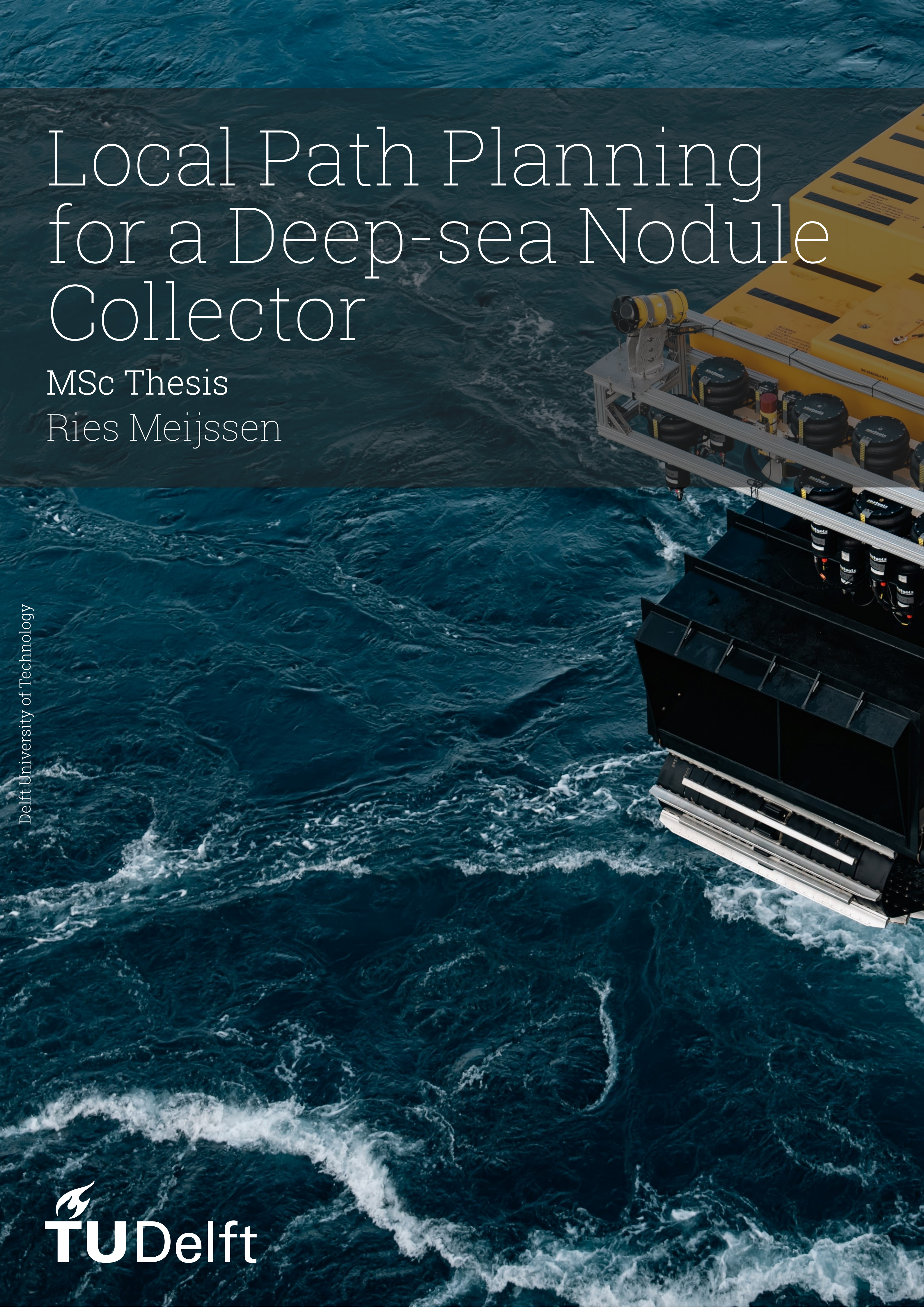

Local Path Planning for a Deep-sea Nodule Collector

MSc Thesis

Ries Meijssen

Delft University of Technology

TU Delft

Local Path Planning for a Deep-sea Nodule Collector

by

Ries Meijssen

to obtain the degree of Master of Science
at the Delft University of Technology,
to be defended publicly on Thursday April 4, 2024 at 13:00 AM.

Student number:	4598830	
Project duration:	May 1, 2023 – April 4, 2024	
Thesis committee:	Ir. K. Xepapa	Allseas Engeering B.V., daily supervisor
	Dr. A. Coraddu	TU Delft, supervisor
	Dr. J. F. P. Kooij	TU Delft, supervisor
	Dr. B. Shyrokau	TU Delft

Cover: Picture of the collector during the Pilot Mining Test, November 2022. Courtesy of Allseas Engineering B.V.
Style: TU Delft Report Style, with modifications by Daan Zwaneveld

An electronic version of this thesis is available at `http://repository.tudelft.nl/`.

TU Delft

Summary

The demand for Energy Transition Metals has been rising due to the worldwide shift towards sustainable energy sources [19]. Deep-sea Nodule Collection (DSNC) has the potential to address current demands for nickel, copper, cobalt, and manganese [13, 17]. In contrast to traditional onshore mining methods, DSNC results in a notable decrease in emissions [25] and a substantial reduction in waste generation [23]. Furthermore, the usage of advanced equipment in DSNC effectively tackles the inherent socioeconomic issues associated with conventional mining.

The current state-of-the-art method for DSNC is to use a large, remotely operated vehicle known as the collector to drive across the deep-sea floor and to collect the nodules. Due to the constraints within the design of the DSNC system and the need for systematic nodule collection, the collector should follow a pre-determined global path. The global path is created from inaccurate presurvey measurements, and is therefore inefficient and hazardous if followed directly. This research aims to examine if a local path planning can be used to improve the imperfect global path.

Existing literature within the field of DSNC is limited, therefore local path planning methods from other applications are examined. From the found local path planning methods, it was found that an Interpolating Curve Planner (ICP) could be most suitable due to its ability to directly incorporate the collector constraints and production rate objectives. This has led to the following research question: *In the context of deep-sea nodule collection, how does an Interpolating Curve Planner perform in terms of reliability, collection rate and area coverage, and how are they influenced by varying presurvey measurement resolutions?*

The ICP was specifically developed to align with the objectives of DSNC. To increase the overall area coverage, it is desired for the collector to follow the path exactly next to the previous track P_{NPT}. This objective conflicts with the objective to follow the global path P_G. To address this, each timestep, a decision-making method was used to choose one of the two as the input path to follow P_F for the ICP. Based on P_F, multiple path candidates are proposed using one of the three examined path proposal methods: the Curvilinear method as defined by Chu et al. [5], and the Local and Global Orthogonal methods, both simplifications of the Curvilinear method. Finally, the collector moves forward on the path with the lowest total cost. This cost function is designed to consider the objectives of obstacle avoidance, production rate maximisation, and adherence to P_F.

The designed ICP is tested in a simulator based on real bathymetric data from a measured section of the Clarion-Clipperton Zone. Before a simulated test, the presurvey measurements are modeled with a certain resolution ρ_{pre}. Based on these presurvey measurements, a global path is created that moves around detected obstacles. The global path and presurvey measurements form the initial knowledge of the ICP. In the simulation, based on the local sensor setup and the simulated environmental noise level $N_e(t)$, the collector measures the environment with a certain accuracy, and responds accordingly. The performance of a simulated test is compared against the oracle performance, which is a standard representing the possible performance if the environment is precisely known before operation. The total area coverage as percentage of the oracle ϕ_a and the mean area coverage per second as percentage of the oracle ϕ_{cps} are used as performance metrics.

A series of experiments were conducted to investigate the impact of ICP parameters. Firstly, the Curvilinear and Local Orthogonal path proposal techniques were deemed unsuitable for DSNC due to intrinsic limitations, which resulted in increased susceptibility to collisions. The Global Orthogonal path proposal method is selected for the other experiments. Secondly, a timestep ΔT larger than 30 seconds is found to decrease ϕ_{cps}, and $\Delta T = 20$ s is used for the subsequent experiments. The third experiment examines the longitudinal path proposal distance $D_{lookahead}$. It is found that for $D_{lookahead} \leq 50$ m and $D_{lookahead} \geq 150$ m, the ICP is susceptible to collisions. Furthermore, a lower $D_{lookahead}$ results in a higher ϕ_a, but at the cost of a decreased ϕ_{cps}. Finally, the influence of changing the weights within the cost function is examined. It is found that increasing priority to maximizing production rate at each

timestep does not result in a higher ϕ_{cps}. Contrary, prioritizing following P_F does result in a greater ϕ_{cps}.

A second set of experiments was performed to examine the influence of the presurvey resolution ρ_{pre} and environmental noise level $N_e(t)$ on the performance of the ICP. It was found that ρ_{pre} does not meaningfully influence ϕ_a or ϕ_{cps}, but it does influence if a test results in a collision. Within the created simulation environment, the ICP cannot safely navigate around undetected obstacles that are wider than 65 meters. Furthermore, along different $N_e(t)$, it was found that the total area coverage does not increase when the ICP follows the path next to the previous track P_{NPT}. This shows that P_{NPT} and P_G cannot be used interchangeably as path to follow within the ICP, and that they should be followed in different manner.

Given that obstacles wider than 65 meters are detected during presurvey, the ICP is able to improve the imperfect global paths. On four large test areas, the ICP achieves more than 95% of the area coverage of the oracle, and more than 93% of the area coverage per second of the oracle. It is a first step towards optimized nodule collection. Further research is needed to examine different cost functions and to find a method of considering P_{NPT} that will increase the total area coverage.

Acknowledgements

I would like to thank the company Allseas for providing me with a place to do my thesis and for the great working environment. In particular, I would like to thank Katerina for always having my back and helping me during the last 11 months. You truly are an inspiration to the people around you and a cornerstone in both the CAM and DSNC department. Secondly, in order of appearance, I would like to thank Niek, Martijn, Mario, Vipul, Ioana, Reinoud, Max, Kjell, Amy, David, and all other unmentioned Allseas employees for making my graduation time a lot more enjoyable. I couldn't have done it without you.

Secondly, I would like to thank my TU Delft supervisors Andrea Coraddu and Julian Kooij for your direction in defining this thesis and for keeping me on the academically relevant path.

I would like to thank my friends and family for your continued support. Coen, thank you for looking after me during stressful times. Lastly, my greatest thanks to my girlfriend Meike for her unending support and for always saying just the right things to get my head organized.

👍👍

Contents

Summary i

Acknowledgements iii

Nomenclature vi

1 Introduction 1
- 1.1 Problem introduction . . . 1
- 1.2 Thesis scope . . . 4
- 1.3 Research Questions . . . 6

2 Related work 7
- 2.1 Path planning methods for DSNC . . . 7
  - 2.1.1 General mining patterns . . . 7
  - 2.1.2 Obstacle avoidance methods . . . 8
  - 2.1.3 Research gaps in DSNC path planning research . . . 9
- 2.2 Local path planning literature . . . 9
  - 2.2.1 Local path planning methods in other applications . . . 9
  - 2.2.2 Local path planner selection . . . 10
- 2.3 Contributions . . . 11

3 Methodology 12
- 3.1 Cost functions . . . 13
  - 3.1.1 Specification of objectives . . . 13
  - 3.1.2 Obstacle avoidance . . . 13
  - 3.1.3 Deviation from the path to follow . . . 14
  - 3.1.4 Expected production rate . . . 14
  - 3.1.5 Combining the cost functions . . . 15
  - 3.1.6 Path candidate optimization . . . 15
- 3.2 Generation of path candidates . . . 16
  - 3.2.1 Cubic spline . . . 16
  - 3.2.2 Arc length parameterization . . . 17
  - 3.2.3 Curvilinear path proposal method . . . 18
  - 3.2.4 Local and global orthogonal path proposal methods . . . 19
  - 3.2.5 Lateral offset of path candidates . . . 20
- 3.3 Environment and sensor representation . . . 21
  - 3.3.1 Environment representation . . . 21
  - 3.3.2 Presurvey map creation . . . 21
  - 3.3.3 Noise level modeling . . . 22
  - 3.3.4 Sensor modeling . . . 22
  - 3.3.5 Obstacle detection . . . 23
- 3.4 Path to follow . . . 24
  - 3.4.1 Global path creation . . . 24
  - 3.4.2 Path to follow decision making method . . . 25
- 3.5 Assumptions and constraints . . . 26

4 Experiments 27
- 4.1 Experimental setup . . . 27
  - 4.1.1 Test locations and shape . . . 27
  - 4.1.2 Environment preprocessing . . . 28
  - 4.1.3 Global path of the test area . . . 28

4.1.4 Variables 29
4.1.5 Performance metrics 29
4.1.6 ICP parameter optimization 30
4.1.7 Code structure and simulation speed 31
4.2 Experiment 1: Influence of path proposal method 32
4.2.1 Setup 32
4.2.2 Results 33
4.3 Experiment 2: Influence of ΔT 36
4.3.1 Setup 36
4.3.2 Results 37
4.4 Experiment 3: Influence of u_c and $D_{lookahead}$ 40
4.4.1 Setup 40
4.4.2 Results 41
4.4.3 Problems with a small $D_{lookahead}$ 43
4.4.4 Problems with a large $D_{lookahead}$ 44
4.5 Experiment 4: Verification on larger areas 46
4.5.1 Setup 46
4.5.2 Results 48
4.5.3 Collisions on undetected obstacles 50
4.6 Experiment 5: Different environmental noise levels 52
4.6.1 Setup 52
4.6.2 Results 53

5 Conclusion **55**

References **58**

A Visualization of oracle global paths **60**

B System structure **62**

C Table results experiment 1 **63**

D Table results experiment 2 **65**

E Table results experiment 3 **66**

F Table results experiment 4 **68**

G Table results experiment 5 **70**

H Experiment: Influence of presurvey resolutions **71**
H.1 Setup 71
H.2 Results 72

Nomenclature

Abbreviations

Abbreviation	Definition
ACO	Ant Colony Optimization
AUV	Autonomous Underwater Vehicle
CCZ	Clarion-Clipperton Zone
DRL	Deep Reinforcement Learning
DSNC	Deep-sea Nodule Collection
ICP	Interpolating Curve Planner
ISA	International Seabed Authority
MBES	Multibeam Echo Sounder
PMT	Pilot Mining Test
PSO	Particle Swarm Optimization
SLAM	Simultaneous Localization and Mapping
TMC	The Metals Company
USBL	Ultra Short Baseline
VTS	Vertical Transport System

Symbols

Symbol	Definition	Unit
$\mathbf{A}_M$	Accuracy of the measurements within $\mathbf{E}_M$	-
C_{dist}	Cost associated with the distance from the path to follow P_F	-
C_{nod}	Cost associated with maximizing production rate PR	-
C_{obs}	Cost associated with obstacle avoidance	-
C_{tot}	Total cost of a path candidate	-
$d_{final,i}$	Lateral deviation from global path of path candidate $p_{c,i}$	[m]
$D_{lookahead}$	Longitudinal path proposal distance	[m]
d_{max}	Maximum lateral deviation of all path candidates	[m]
$\mathbf{E}_M$	Measured environment	-
$\mathbf{E}_P$	Presurvey map	-
$\mathbf{E}_T$	Ground truth environment	-
L_{tot}	Total length of a path or path candidate	[m]
M	Arbitrarily large number for calculating C_{obs}	-
NA_a	Assumed constant nodule abundance on the test areas	[kg/m^2]
$\mathrm{NA}(x, y)$	Nodule abundance at location (x, y)	[kg/m^2]
$N_e(t)$	Modeled noise level in the environment at time t	-
$p_{c,i}$	Path candidate	-
P_F	Path to follow	-
P_G	Global path	-
P_{NPT}	Path next to previous track	-
P_{PT}	Previous track	-
$\mathrm{PR}_{expected}$	Expected production rate of a path candidate	[kg/s]

Symbol	Definition	Unit
$PR_{nominal}$	Nominal production rate	[kg/s]
$r(s)$	Radius of the curvature of a path at a given arc length	[m]
R_{col}	Distance to the collector	[m]
R_s	Simulated sensor range	[m]
s	Arc length along a path or curve	[m]
T_{noise}	Duration of environmental noise	[s]
$T_{noiseless}$	Duration of period of low environmental noise	[s]
T_{tot}	Total time of a path or path candidate	[s]
u_c	Variable to change the weights of C_{dist} and C_{nod}	-
V	Velocity of the collector	[m/s]
V_G	General direction of global path	-
V_{cruise}	Cruising velocity of the collector	[m/s]
W_c	Width of the collector	[m]
ΔT	Timestep of simulator	[s]
η_p	collection efficiency	-
Θ_s	Angle of the sensor cone	[°]
$\kappa(s)$	Curvature of a path at a given arc length	[m^{-1}]
ρ_{pre}	Presurvey resolution	[m]
ρ_T	Ground truth resolution	[m]
ϕ_a	Total area coverage of an ICP configuration, as percentage of the oracle	-
ϕ_{cps}	Mean area coverage per second an ICP configuration, as percentage of the oracle	-

1
Introduction

1.1. Problem introduction

There is a growing emphasis on reducing greenhouse gas emissions as a response to the global climate problem. To achieve this goal, society must shift away from reliance on fossil fuels and embrace more environmentally friendly technologies such as electric vehicles. The growing demand for batteries and similar green technologies is leading to an increasing demand for various elements, which are recognized as the 20 Energy Transition Metals [19]. Among those metals are copper (Cu), cobalt (Co) and nickel (Ni) [13].

Currently, these metals are mined predominantly in onshore mines. These onshore mines have drawbacks which will only grow with the increasing demand for metals. The first drawback is related to the declining ore grades, requiring more raw material to produce the same amount of desired material [2, 14]. Meeting the increasing demand will necessitate mining operations to delve deeper into the earth and extract more materials, resulting in elevated waste production and energy consumption.

The second drawback of onshore mining is related to its inherent socioeconomic problems. While the extraction of resources from onshore mines holds the potential to strengthen the economic standing of a developed nation, it frequently gives rise to pervasive issues such as corruption and exploitation, exemplified vividly by the cobalt mines in the Democratic Republic of the Congo [33]. Likewise, in Tanzania, the operations of gold mines have given rise to issues such as increased unemployment, the forced displacement of local inhabitants, the involvement of children in labor, and heightened challenges in land acquisition for Tanzanians [16]. The combination of these socio-economic challenges, along with growing environmental concerns, emphasizes the necessity for a departure from conventional mining practices.

Figure 1.1: Picture of a polymetallic nodule collected by Allseas.

One potential solution to address the increasing need for materials is the collection of polymetallic nodules [13]. These black, potato-shaped mineral concretions, known as nodules, are found unattached on the deep-sea floor, particularly on the abyssal plains of the Clarion Clipperton Zone (CCZ). An example of a nodule can be seen in figure 1.1. They are rich in manganese, nickel, cobalt and copper, and could be used as an alternative for onshore resources [7, 13]. Estimates indicate that the CCZ harbors over 21 billion tonnes of nodules, surpassing global land reserves for manganese, nickel and cobalt [17].

At this moment, the state-of-the-art method for collecting polymetallic nodules includes using a remotely operated vehicle known as a collector or mining robot. The collector employs a suction mechanism to gather nodules from the seafloor. The nodules are then transported to the main vessel through an airlift riser system, also referred to as the vertical transport system (VTS) [1, 20]. From the main vessel, they are transported to the shore by offloading vessels. A schematic overview of deep-sea nodule collection (DSNC) can be seen in figure 1.2.

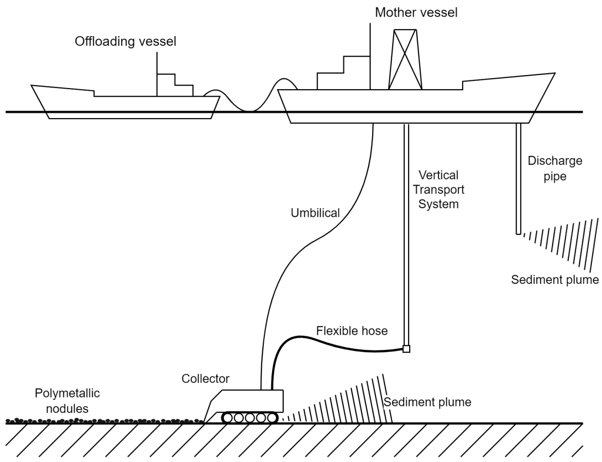

Figure 1.2: Overview of the current state of the art for DSNC.

DSNC provides an answer to the drawbacks inherent to onshore mining. The unique characteristic of nodules resting atop the seafloor allows for collection without excavation, and the process produces less waste of lower quantities compared to onshore mining [23]. Furthermore, the production of battery metals from polymetallic nodules has the potential to decrease CO2 emissions produced during the mining process by over 70% [24, 25]. Additionally, deep sea mining involves advanced automated technologies, minimizing the reliance on manual, strenuous labor. The process of collecting minerals from the bottom of the deep sea is by definition without human involvement, making it a significant stride towards eradicating child labor from the mining industry.

DSNC is currently in its developmental phase, with industry leaders such as Allseas actively working to advance the state of the art technologies. Together with The Metals Company (TMC), a Canadian mining company, Allseas aims to develop a commercially viable DSNC system. By the end of 2022, a successful pilot mining test (PMT) in the CCZ was conducted using a 6-meter wide collector. During that test, an estimated 4500 tonnes of polymetallic nodules were collected, showing the feasibility of the proposed DSNC system. This research is performed in collaboration with Allseas.

DSNC has a range of technological, regulatory, and economical challenges. Firstly, the deep-sea environment poses significant engineering and logistical obstacles. The polymetallic nodules are situated between 4.5 and 6 km beneath the sea surface, subject to extreme pressure, near-freezing temperatures, absence of sunlight, and fast light dispersion [1, 36]. The complexity goes beyond the mere extraction of nodules, as there is also a need for a system for transporting nodules from the mining vessel to the shore via bulk carriers. Additionally, it is essential to build new processing factories to convert the raw material into usable resources.

Secondly, environmental concerns arise during the collection process [4]. The spading and disturbance of the deep-sea floor during nodule extraction result in the suction mechanism not only picking up nodules, but also organisms and a thin top layer of sediment [13]. The sediment is separated from the nodules partly on the collector, and partly on the vessel, as visualized in figure 1.2. The sediment gets released both around the collector and from a discharge pipe in the sea at a depth of 1.5 kilometers. The resulting sediment plumes could suffocate organisms living in the deep-sea or in the sea around the discharge pipe. Though there is significantly less biomass in the deep-sea compared to shallow waters, it consists of largely undiscovered species using living mechanisms not well understood [8, 9, 32].

Furthermore, lack of understanding about the deep-sea ecosystem makes it difficult to evaluate the environmental impacts of deep-sea mining [13]. The International Seabed Authority (ISA), responsible for managing the deep-sea beyond national jurisdictions, faces the challenge of regulating DSNC while ensuring marine environmental protection. The uncertainties in the deep-sea environment make the formulation of regulatory guidelines a difficult task.

Lastly, DSNC has yet to achieve economical viability [4]. No company has successfully rendered DSNC economically feasible, given the substantial resources required for nodule collection and transportation to the vessel. The implementation of new infrastructure, including a 4.5 km long Vertical Transport System (VTS) and umbilical for power and communication, poses technical and financial challenges. Additionally, the vehicle must exhibit exceptional robustness to endure continuous collection in the harsh conditions of the deep-sea [4]. These challenges collectively underscore the intricate nature of transitioning to DSNC as an alternative to conventional mining practices.

The economical, environmental and regulatory obstacles have impeded the widespread adoption of commercial DSNC. Nevertheless, with the depletion of onshore mines and the resultant rise in metal prices, there is a growing interest in DSNC. This thesis concentrates on optimized continuous operation, as it is a crucial part in making DSNC economically viable.

There is a need for a systematic approach to collecting nodules, because the collector is subject to several constraints. As can be seen in figure 1.2, the collector is connected to the VTS using a flexible hose at the bottom, and it cannot deviate too much from the VTS to avoid damaging the system. Furthermore, an umbilical is attached to the collector and may be destroyed or entangled if the collector turns around too quickly or drives in reverse. Additionally, there are multiple offloading vessels continuously moving to the mother ship, so the location of the mining vessel should be known several days in advance. Combined with the objectives to collect nodules efficiently and consistently, these limitations highlight the necessity for the collector to adhere to a pre-determined global path.

It is not possible to plan a global path before operation that avoids all obstacles, collects as many nodules as possible and maximizes area coverage. The route is planned based on pre-operation measurements performed by an Autonomous Underwater Vehicle (AUV). These measurements will be referred to as presurvey measurements. The cost related to surveying the area is exponential to the desired resolution and the acquisition and post processing time is also a significant factor considered when defining the specifications of the presurvey measurements. Therefore, it is accepted that ahead of operation, certain obstacles and local seabed characteristics may be missed. In order to minimize the imperfections of the global path, a conservative approach is selected with large buffering around known objects and buffering in between parallel paths. Additionally, a requirement for during operation is posed to be able to independently detect and react on obstacles, with the primary objective being equipment safety. This process necessitates the use of a local path planning algorithm, that takes an imperfect global path as input and locally improves it using live sensor measurements.

While a human operator is capable of performing local path planning, there are inherent drawbacks to this approach. Human operators may encounter challenges in maintaining a consistently high production rate and are vulnerable to fluctuations in concentration. Additionally, the response time of a human is lower than a control system, posing potential risks to the collector's efficiency and safety. For a DSNC system to achieve sustainable profitability, depending on a human operator is neither economically scalable nor practical. Conversely, a local path planner maintains steadfast attention, potentially enhancing safety and ensuring a more consistent and possibly higher collection efficiency compared to human operators. This research centers on evaluating the effectiveness of a local path planning algorithm specifically designed for DSNC applications.

1.2. Thesis scope

This research will concentrate on developing a local path planning algorithm to improve mining efficiency and achieve continuous operation for DSNC, as discussed in the preceding section. Designing a local path planning algorithm poses a complex challenge with various potential approaches. Testing the algorithm on the deep-sea mining robot itself is not possible, as it would inhibit testing hazardous edge cases. A hardware-in-the-loop solution can be created to approximate the collector's control system. However, for this thesis, it will be too time consuming to integrate the algorithm in the embedded system and combine it with simulated sensor measurements. Consequently, the local path planner's performance is evaluated within a novel simulation environment. This approach offers a cost-effective means to comprehensively analyze the algorithm's performance without the constraints of practical testing in the deep-sea environment.

For this research, a new simulator is constructed from scratch, given the absence of an existing simulator at Allseas. The construction of a 3D simulator is a conceivable option, as demonstrated in prior research by Wiberg et al. [37], where a local path planning algorithm for an off-road vehicle was developed. However, a 3D simulator will be too computationally expensive and often real-time, which will be limiting for this study. Furthermore, Wiberg's research had a large focus on developing a dynamical model, while this research concentrates on the local path planner. Dynamics such as roll, pitch, and slip are not incorporated, as this would add unnecessary complexity to the model and shift the focus too far away from local path planning. Therefore, the environment is built in 2D, instead of opting for a 3D representation.

An overview of the components essential for the control of a deep-sea nodule collector can be seen in figure 1.3. On the left side, the route planning before a mining operation is shown. Using low-resolution presurvey measurements and the physical constraints of the collector, an imperfect global route is planned. Within Zoetmulder's thesis, process is called short-term route planning, but will be called global path in this thesis [42]. The global path forms the foundation for the directions that the collector should follow during DSNC operation.

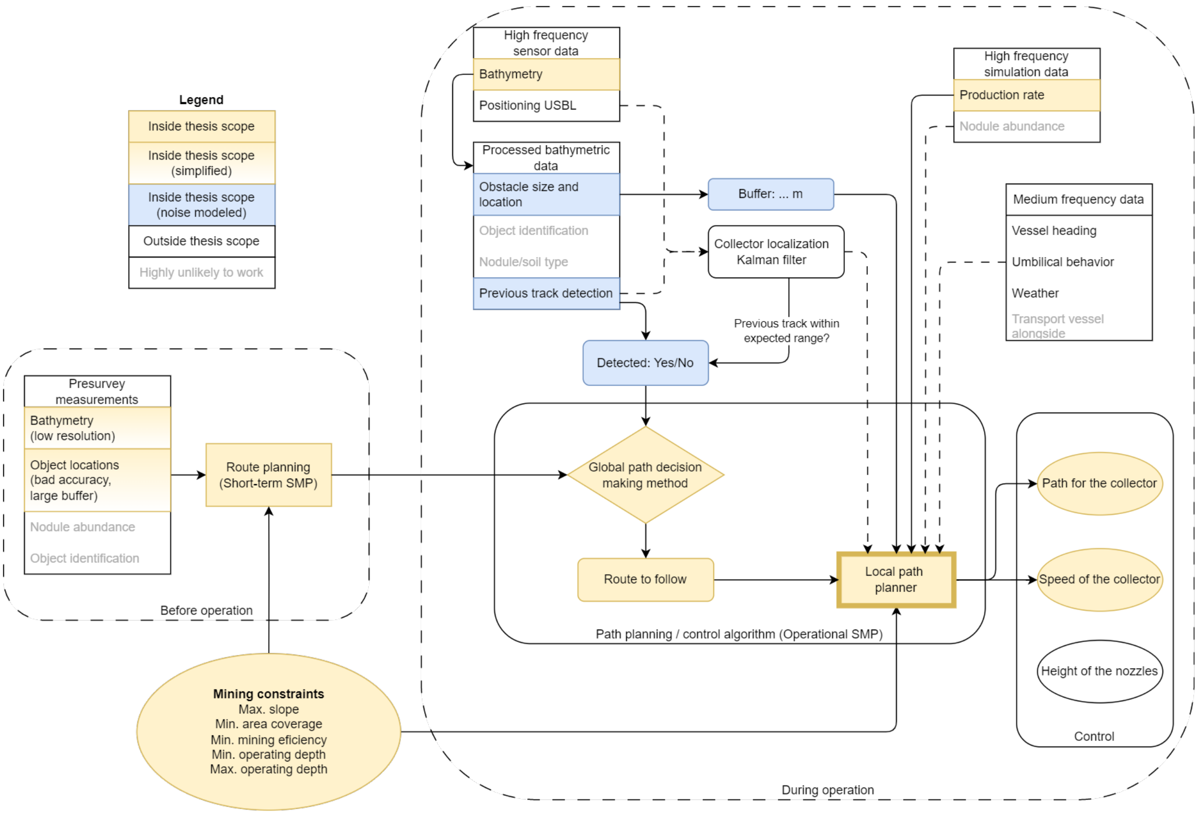

Figure 1.3: Overview of the scope of this thesis.

On the right in the diagram, the main local path planning control algorithm is described. Beside the global path, it incorporates two types of high frequency sensor input. Firstly, bathymetric data from a Multibeam Echo Sounder (MBES) in front of the collector is used. The MBES measures the ground's topology, enabling the identification of traversable and non-traversable areas on the map [6, 28]. To account for measurement noise, a buffer is added to each identified obstacle. The buffer size is determined by the collector's distance to the obstacle and a time-dependent variable specifying noise levels within the simulator. This buffered obstacle map is an important input for the path planner.

To optimize area coverage, it is advantageous to follow the path exactly next to the previous track. The location of the previous track can be derived from the MBES data, as the collector leaves an imprint in the sand. However, due to noise and inaccurate sensors, the previous track may not always be accurately measured. This unreliability is modelled using the same time-dependent noise variable used for determining obstacle certainty.

The other sensor input is positional data from the Ultra Short Baseline Acoustic Sensor (USBL). In depths of more than 4 km, the USBL has a relatively low accuracy of about 5 meters. However, this can be increased using simultaneous localization and mapping (SLAM) on local features measured by the MBES [26]. The positions found by both methods can be combined using a Kalman filter to improve positioning accuracy. For the purpose of this research, however, positioning is assumed to be error-free.

Beside data coming from sensors, the local path planner should also predict the production rate and choose its path based on how much it expects to collect. It depends on the velocity of the collector and the nodule abundance on the ground. While it is highly unlikely that it will be possible to measure the nodule abundance in front of the collector, it is possible to avoid areas that are already covered by the collector. The production rate is a crucial metric within the scope of this thesis.

Other data, such as vessel heading, umbilical behavior and weather are excluded from consideration. Though these factors will play an important role during actual DSNC operation, the impact on the local path planning is assumed to be small, and it would add unnecessary complexity to the model.

After careful consideration from available research, the Interpolating Curve Planner (ICP) is selected as the local path planning method for implementation. This choice is motivated by its flexibility in incorporating complex objective functions, computational efficiency, and its ability to follow the general direction of the global path. More information regarding the selection of the path planner can be found in chapter 2, and information about the setup of the ICP and the associated cost functions is provided in chapter 3.

1.3. Research Questions

Following the thesis scope described in the previous section, this research aims to develop an ICP model for the application of DSNC. Along multiple hyperparameters, the performance of the model is evaluated based on various metrics. Firstly, the ICP should ensure the safety of the collector by steering around previously undetected obstacles. Additionally, the model is examined in terms of total area coverage and collection rate, serving as indicators of the profitability of a mining operation. This results in the following research question:

> In the context of deep-sea nodule collection, how does an Interpolating Curve Planner (ICP) perform in terms of reliability, collection rate and area coverage, and how are they influenced by varying presurvey measurement resolutions?

To answer this research question, it is divided into several sub-questions that assess the influence of different simulator and ICP model hyperparameters:

> What path proposal method is most suitable for an ICP in the context of DSNC?

> What is the influence of the timestep for an ICP in the context of DSNC?

> What is the influence of changing the weights of the cost functions and the path proposal distance on the performance of an ICP in the context of DSNC?

> What is the performance of an ICP on larger DSNC areas, when different presurvey resolutions are used?

> What is the performance of an ICP on larger DSNC areas, when different simulated environmental noise levels are used?

2

Related work

As outlined in chapter 1, this research centers around the evaluation of a local path planning method for DSNC. In section 2.1, an examination of existing literature about path planning methods for DSNC is conducted. It will focus on both global and local path planning methods, along with general mining patterns, considering the limited availability of research in this domain. Subsequently, section 2.2 explores local path planning methods used in various other applications, from which a suitable method will be chosen for this research. Finally, the contributions of this research are outlined in section 2.3

2.1. Path planning methods for DSNC

Research specifically dedicated to local path planning methods for DSNC is currently lacking. However, a limited body of literature exists on the broader subject of path planning for DSNC. This literature can be broadly categorized into two main groups. Firstly, there are studies that concentrate on exploring general mining patterns, exemplified by works such as those by Park et al. and Ponguillo-Intriago [22, 27]. These methods, falling under the category of mining patterns, are discussed in section 2.1.1. Secondly, there are studies that delve into methods for obstacle avoidance and navigating from one point to another in the deep-sea environment, as elaborated in section 2.1.2. The following research gaps are described in section 2.1.3.

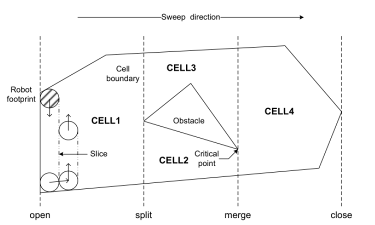

Figure 2.1: Illustration of the cellular decomposition method and the direction-parallel path planning method proposed by Park et al. [22].

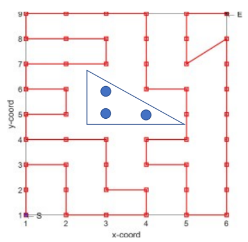

Figure 2.2: Visualization of a collector path resulting from the Genetic Algorithm proposed by Ponguill-Intriago et al. [27].

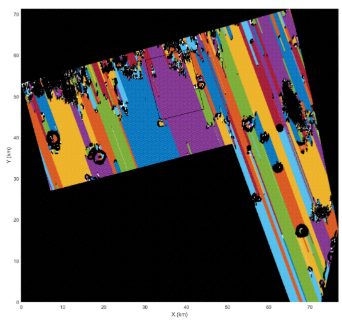

Figure 2.3: Mining areas as determined by Zoetmulder [42].

2.1.1. General mining patterns

Park et al. conducted an examination of general driving patterns suitable for deep-sea nodule collection and their application to a larger map [22]. The initial step in their approach involves dividing the two-dimensional map into obstacle-free cells. Subsequently, for each cell, a mining pattern is added, which could be either a contour-parallel pattern or a direction-parallel pattern. The direction-parallel method is depicted in figure 2.1. Both patterns ensure total area coverage within each cell. However, as obstacle density and complexity increase, the resulting paths tend to be short and contain numerous turns. The study acknowledges the importance of minimizing turns for optimizing collection efficiency, yet practical considerations may not have been fully addressed.

Ponguillo-Intriago et al. propose the use of a Genetic Algorithm to determine a path that covers the entire area with a focus on minimizing turns for enhanced system safety [27]. Figure 2.2 illustrates a path created using this model. While the proposed paths in the visualized area could be okay, the real-life topology looks very different than the shown map. This is a giant limitation of this method, as the resulting paths are far from practically usable.

Zoetmulder conducted a study on the hypothetical production rate of deep-sea mining sites, using bathymetric data collected by Allseas [42]. This research introduces a standardized methodology for delineating mining fields within a licensed area and determining the direction of the mining pattern within that region, utilizing the direction-parallel method proposed by Park et al. [22]. An example of the mining fields can be seen in figure 2.3. The study extensively explores the process of proposing paths tailored to specific mining areas. While the resulting paths are effective and practical, they cannot be directly used as input for the collector due to the potential oversight of obstacles during the planning phase. Therefore, a local path planner remains essential.

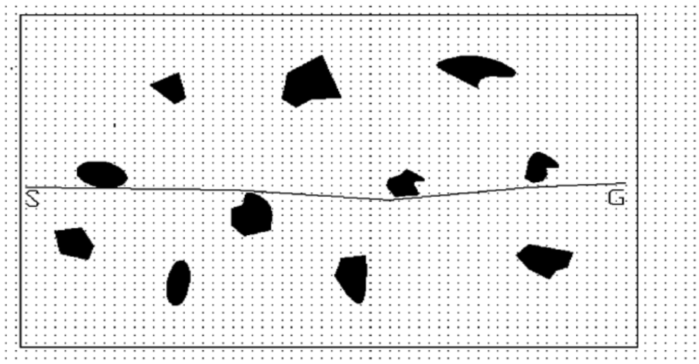

Figure 2.4: Visualization of a path created by the hybrid ACO-PSO path planning algorithm, as designed by Shi et al. [29].

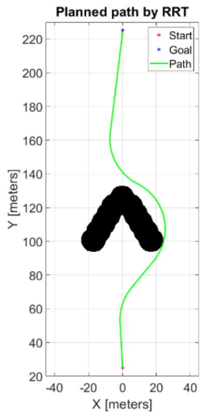

Figure 2.5: Visualization of a path created using a sample-based planner as proposed by Surewaard [34].

2.1.2. Obstacle avoidance methods

Shi et al. have performed a study on a path planning method for DSNC applications using an ant colony optimization (ACO) algorithm, from which the parameters are optimized by particle swarm optimization (PSO) [29]. The objective of the ACO-PSO method is solely to minimize the total length of the path from startpoint S to endpoint G through a given two-dimensional obstacle map. A visualization of one of such paths can be seen in figure 2.4. It provides a path that steers clear of obstacles, but does not take into account other important objectives, such as area coverage or production rate.

Surewaard researched using a sample-based planner to perform path planning for a deep-sea nodule collector [34]. Four planners were compared on several maps, and it was found that a RRT planner performed best in terms of deviation from the original path. One of the tests can be seen in figure 2.5. The collector used a simulated MBES to do live obstacle detection. A limitation of the model, as stated in the thesis, is that the previous track of the collector is seen as an obstacle, instead of traversable terrain. Also, while the RRT planner did aim to minimize deviation from the straight line between the start and end goal, it did not consider the effect on the nodule production rate.

While both models offer secure approaches for navigating from one point to another, their representation may not align with real-life DSNC. Firstly, both studies have been exclusively conducted on fictional maps, and the applicability of their performance in an actual deep-sea environment remains uncertain. Secondly, these methods solely evaluate the efficiency of point-to-point navigation and do not address the broader context of collection efficiency within a larger test area incorporating a mining pattern, as discussed in section 2.1.1.

2.1.3. Research gaps in DSNC path planning research

The existing literature on path planning methods for DSNC is notably limited, as summarized in table 2.1. While some studies delve into general mine planning, only one such study, Zoetmulder's thesis, incorporates actual bathymetric data [42]. However, his approach uses the unrealistic simplification that the collector will drive on obstacle-free patches, and cannot move around obstacles. While all studies examine parts of the bigger picture, they all fall short of proposing a method that can be used during the DSNC process.

To achieve optimized nodule collection, incorporating a local path planner is essential. While the studies by Shi et al. and Surewaard present methods for navigating from one point to another, they overlook crucial considerations such as production rate and area coverage over an extended period [29, 34]. This identified gap underscores the necessity for a comprehensive study focused on developing a local path planner that not only addresses the objectives mentioned earlier but also integrates into the larger context of DSNC operations.

Paper Title	**Author**	**Year**	**Real bathymetric data**	**Live sensor simulation**	**Considers production rate**	**Considers area coverage**	**Moves path around obstacles**
A study of sweeping coverage path planning method for deep-sea manganese nodule mining robot	Park	2011	No	No	**Yes**	**Yes**	No
Genetic Algorithm for Solving Coverage Issues in Undersea Mining	Ponguillo -Intriago	2021	No	No	No	**Yes**	**Yes**
Developing concepts for the mine planning of deep-sea polymetallic nodules	Zoetmulder	2020	**Yes**	No	**Yes**	**Yes**	No
Path planning for deep sea mining robot based on ACO-PSO hybrid algorithm	Shi	2008	No	No	No	No	**Yes**
Obstacle Detection and Collision Avoidance for Deep Sea Bottom Mining	Surewaard	2021	No	**Yes**	No	No	**Yes**

Table 2.1: An overview of existing literature in path planning methods for deep-sea nodule collection.

2.2. Local path planning literature

In the absence of extensive research on local path planning methods for DSNC, other applications need to be examined. Section 2.2.1 introduces various local path planning methods studied in other applications, and section 2.2.2 identifies a method deemed suitable for DSNC.

2.2.1. Local path planning methods in other applications

In the absence of specific studies on local path planning methods for Deep-Sea Nodule Collection (DSNC), an examination of local path planning strategies designed for other applications is warranted. Firstly, off-road vehicles are examined, as their environment shares notable similarities with the deep-sea environment, where obstacles are static, and the vehicle can drive anywhere that is traversable. For this application, an Interpolating Curve Planner (ICP) has been investigated for local path planning [5]. Additionally, reactive methods utilizing Deep Reinforcement Learning (DRL) have been explored in various studies, including those by Josef et al. [15], Wiberg et al. [37], and Zhang et al. [40].

Local path planning for road vehicles are thoroughly researched. The environment and objectives are slightly different than for DSNC, as a road vehicle needs to consider dynamic obstacles, road rules and passenger comfort. It is found that the main algorithms used in this field are either an ICP or a State Lattice combined with Graph Search [11, 38, 41]. A modified A* algorithm could also be used [10].

Harvesting robots, like a nodule collector, face a similar coverage path planning problem. One research proposes Quantum-behaved Particle Swarm Optimization (QPSO) for obstacle avoidance [39]. Another source implemented an Artificial Potential Field method, though this method is shown to be subjective to local minima [18, 21].

Furthermore, the environment of Mars resembles the harshness and bareness of the deep-sea, so Mars rovers are also examined. The main method for this application seems to be a grid search approach[3, 30].

Moreover, the environment of Mars resembles the harsh and desolate conditions of the deep-sea. Thus, an examination of path planning methods employed by Mars rovers becomes relevant. The primary method prevalent in this application appears to be the utilization of a grid search approach [3, 30]. While these methods provide a safe route around obstacles, they do not systematically consider factors such as area coverage or the velocity of the rover.

2.2.2. Local path planner selection

This section will compare the four most recognized local path planning algorithms found in existing literature. They consist of a state lattice with graph search, a grid search utilizing methods like A*, an Interpolating Curve Planner (ICP), and reactive methods such as Deep Reinforcement Learning (DRL) or Particle Swarm Optimization (PSO). Each of these methods provides viable strategies for obstacle avoidance and the following of a global path.

To determine the suitability of these local path planning methods for deep-sea nodule collection, it is crucial to align them with the specific objectives of the application. Firstly, a deep-sea mining robot needs to follow the global path as closely as possible to minimize deviation from the VTS. Additionally, when the previous track is detected, the robot should aim to drive alongside it to optimize area coverage. Thirdly, the collector has to keep moving in the general direction of the global path to prevent entanglement of the umbilical and the VTS. Lastly, optimizing production rate is of utmost importance, suggesting that the incorporation of the a production rate objective function into the local path planner would be a valuable addition. Keeping these DSNC-specific objectives in mind, a comparison of the local path planning methods can be made.

A state lattice constructed around the global path is effective in maintaining the required lateral distance, and its systematic search through the state space allows for the incorporation of production rate objectives by adding them to the graph search objective. However, it requires careful tuning of lattice resolution and shape, as the optimal solution must lie on the lattice. A larger lattice with better resolution could potentially yield more optimal routes, but it comes with significant computational expense [11].

Reactive methods, such as DRL, offer speed and flexibility in incorporating various objectives and constraints, including the lateral movement and maintaining the collector's general direction on the global path. However, the performance of such a model is largely dependent on the training data it receives, and without a substantial training database, there is a risk of learning incorrect behaviors.

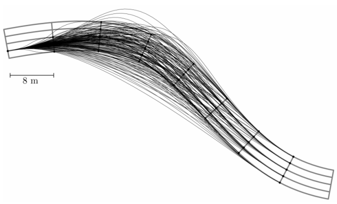

Figure 2.6: Visualization of a state lattice from [41].

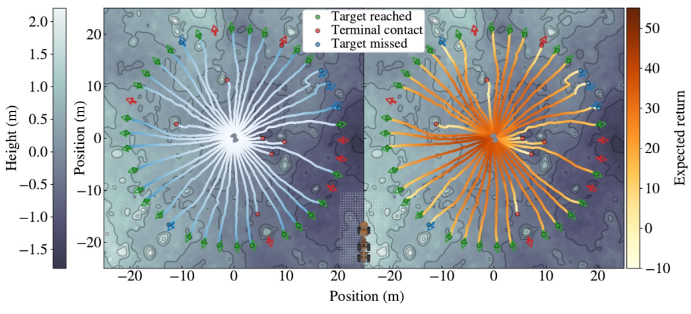

Figure 2.7: Visualization of a path driven using DRL [37].

A grid search method, adapted to take into account the constraints mentioned above, could be an option to traverse along the global path. However, the planning relies on a grid with a given resolution. For DSNC, where the precise path is very important, a small grid size will be needed and this will have large implications on the computational efficiency. Therefore, this method is not ideal for DSNC.

An ICP operates by proposing paths at each timestep based on the global path and advancing one timestep along the path with the lowest cost. This setup inherently addresses two constraints in DSNC: ensuring the collector maintains movement in the general direction of the global path and limiting lateral deviation from the global path. The objective of maximizing production rate could be directly considered as a cost function for path selection. A potential drawback of the method is its dependence on how paths are proposed and the quantity of proposed paths, which may impact the ability to find the optimal route. Nevertheless, it is computationally inexpensive as the costs only need to be calculated from a discrete one-dimensional array of paths [11].

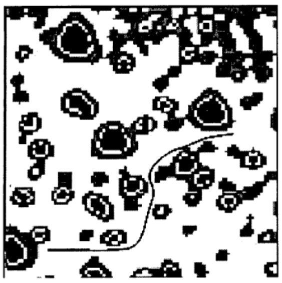

Figure 2.8: Visualization of a grid search method [30].

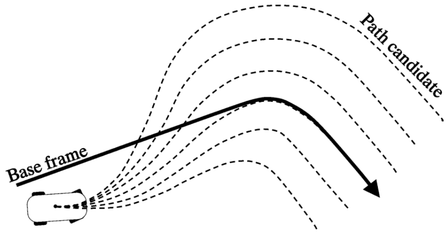

Figure 2.9: Visualization of an ICP [5].

The key points of the identified local path planning methods are summarized in table 2.2. Based on the straightforward implementation of the production rate objective and the incorporated direction and lateral distance constraints, the ICP is the selected local path planning method for testing in the created simulation environment.

Planner type	From	Positives	Negatives
State lattice with graph search	[11, 41]	Can directly implement collector constraints and production rate objectives.	Is computationally expensive. Optimality is dependent on lattice resolution.
Reactive methods	[15, 29, 31, 37, 40]	Could incorporate collector constraints and production rate objectives.	Needs good training data. Risk of the model showing wrong behaviour in different scenarios.
Grid search	[3, 10, 30]	Could incorporate collector constraints and production rate objectives.	Optimality is dependent on grid resolution.
Interpolating curve planner	[5, 11, 38, 39]	Can directly implement collector constraints and production rate objectives. Computationally inexpensive.	Optimality is dependent on path proposal method and proposal resolution.

Table 2.2: Comparison of types of path planners

2.3. Contributions

Given the research gaps as presented in section 2.1.3, and the selected ICP model from section 2.2.2, this research aims to make the following contributions:

- Research the performance of an Interpolating Curve Planner in a DSNC application. Building upon the foundation of Chu et al. [5], this ICP implementation incorporates modified path proposal methods and cost functions, and extended logic to follow both the previous track and the global path. All novelties are further explained in section 3.
- Create novel simulation tool that can include live sensor inputs for a deep-sea nodule collector.
- Use real-life bathymetric data to examine the performance of the ICP along its hyperparameters.

3 Methodology

As mentioned in section 2.2.2, this thesis will implement an Interpolating Curve Planner (ICP) as the local path planner for the nodule collector. The ICP and its place within the larger simulation loop is visualized in figure 3.1. The ICP model is based on the model as proposed by Chu et al. [5]. It contains the following key steps:

1. Propose i path candidates $p_{c,i}$, each with a distinct lateral offset $d_{final,i}$ from P_F, the path that the collector should follow.
2. For each path candidate, calculate the total cost C_{tot} based on several objectives.
3. Move forward ΔT seconds on the path candidate with the lowest total cost.

The cost functions are designed specifically for the DSNC application and are described in section 3.1. Multiple path proposal methods are examined, both based on the ICP model by Chu et al. and modifications of that method. They are all presented in section 3.2.

The other components of the simulator introduce novel features specifically designed for DSNC requirements. One distinctive feature involves the modeling of local sensor measurements to construct an image of the environment. The details of this process is outlined in section 3.3. Another novel feature is the consideration of the previous track P_{PT}. While the collector should primarily follow the predetermined global path P_G, the collector should aim to drive exactly next to the previous track to maximize area coverage if the previous track is detected. The creation of the global path and the process of determining the path to follow P_F are described in section 3.4. Other assumptions and constraints within the simulator are outlined in section 3.5.

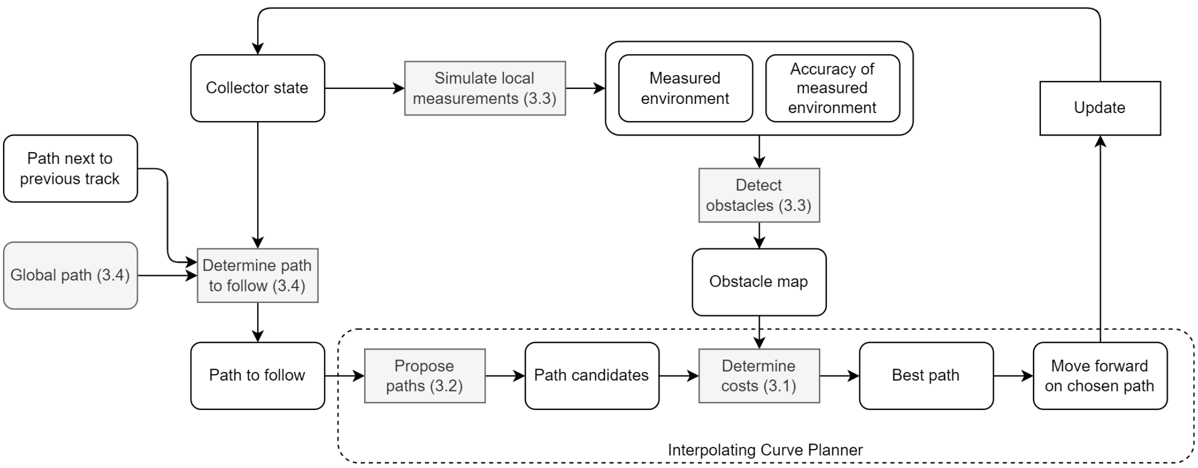

Figure 3.1: Overview of the ICP method as implemented within the simulator. The novelties and corresponding sections are accentuated in grey.

3.1. Cost functions

3.1.1. Specification of objectives

A crucial aspect of determining the behaviour of the ICP is the definition of the cost functions used to select the optimal path from a list of candidate paths. Five primary objectives are identified:

1. Avoid obstacles.
2. Minimize deviation from the predetermined global path P_G.
3. If the previous track P_{PT} is detected, follow the path next to the previous track P_{NPT}.
4. Maximize production rate.
5. Maximize area coverage.

The second and third objectives present a contradiction, as they both guide the ICP to follow different paths. To address this contradiction and provide the ICP with a single directive on which path to follow, a decision-making method is implemented, resulting in either P_G or P_{NPT} as input for the ICP. Detailed reasoning for this decision is further highlighted in section 3.4. The objective for the ICP changes to follow one input path P_F.

Additionally, economic viability is considered the most crucial factor, which is directly dependent on the quantity of nodules collected within a specific timeframe. While final area coverage remains important, it primarily serves as a standard to meet environmental considerations. Therefore, priority is given to the maximization of production rate over the maximization of area coverage. Area coverage is not directly incorporated into the ICP but will be assessed during the experiments.

The implementation of these decisions changes the five objectives mentioned before into the following three:

1. Avoid obstacles.
2. Minimize deviation from the given path to follow P_F.
3. Maximize production rate.

Each objective is captured into its own cost function, as specified in sections 3.1.2 to 3.1.4. Section 3.1.5 describes how the different cost functions are combined into a single path candidate cost, and section 3.1.6 describes how the optimal path is found.

3.1.2. Obstacle avoidance

The most important feature of the ICP is to ensure the safety of the collector. For this, it is important to determine if a path candidate will collide with an obstacle. This process works by buffering each path candidate, and see if the buffered path candidate overlaps with an obstacle. If it overlaps, this means that a part of the collector will, at one point, collide with an obstacle. The collision detection process is visualized in figure 3.2. The creation of the obstacle map is explained in section 3.3.5.

It should not be a valid option to drive towards an obstacle, if other paths are also available. Therefore, the cost associated with obstacle avoidance, C_{obs}, is set to be equal to M if the path candidate collides with an obstacle, as seen in equation 3.1, where M is an arbitrarily large number.

$$C_{obs} = \begin{cases} M & \text{if buffered path candidate overlaps with obstacle} \\ 0 & \text{otherwise} \end{cases} \tag{3.1}$$

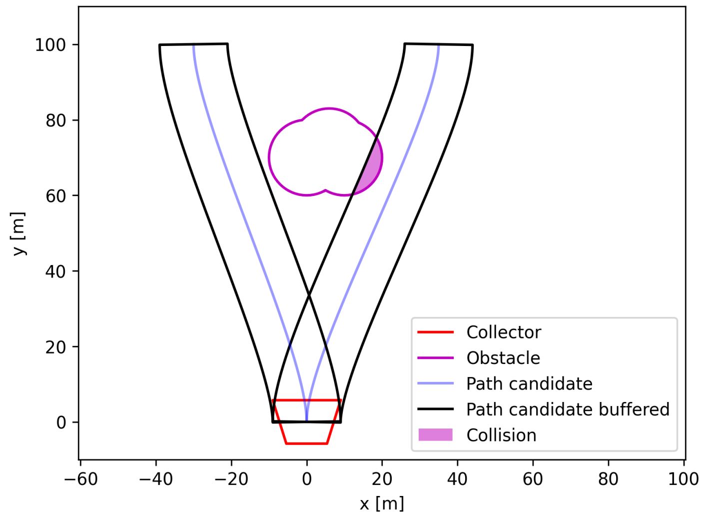

Figure 3.2: Visualization of the obstacle detection process for two path candidates in a hypothetical scenario.

3.1.3. Deviation from the path to follow

One of the objectives is to follow a given path as closely as possible. C_{dist}, the cost associated to this objective, is based on the consistency cost function by Chu et al. [5]. It is set to be equal to the final lateral distance to the global path $d_{final,i}$ divided by the maximum proposed distance d_{max}, as can be seen in equation 3.2. By dividing by d_{max}, the cost is normalized to be on the interval $[0, 1]$.

$$C_{dist} = d_{final}/d_{max} \tag{3.2}$$

3.1.4. Expected production rate

One of the novel additions of this research is that the ICP considers the production rate during path selection. This is done using the cost associated with the nodule collection rate C_{nod}. For determining C_{nod}, it is assumed that the test area has a constant nodule abundance NA_a kg/m^2. For a given path candidate, C_{nod} is designed to be equal to 1 when the path will not collect any nodules. On the other hand, if the projected production rate of a path candidate is equal to that of a straight path driving through an area with nodule abundance NA_a, C_{nod} is equal to 0. It results in equation 3.3.

$$C_{nod} = 1 - (\text{PR}_{expected}/\text{PR}_{nominal}) \tag{3.3}$$

$\text{PR}_{nominal}$ is the constant nominal production rate of nodules in kg/s. This value is determined by the collector's production rate when it follows a straight path in an area with the assumed constant nodule abundance. The calculation of $\text{PR}_{nominal}$ is illustrated in equation 3.4. W_c is the width of the collector in meters, η_p is the collection efficiency, and V_{cruise} is the straight line cruising velocity in m/s.

$$\text{PR}_{nominal} = W_c * \eta_p * \text{NA}_a * V_{cruise} \tag{3.4}$$

The expected production rate for a proposed path, in kg/s, can be calculated using equation 3.5. It depends on T_{tot}, the total time a path will take in seconds, the length of the path L_{tot} and the average nodule abundance that the collector will collect NA_{avg}. T_{tot} can be numerically approximated using equation 3.6. The average nodule abundance for a path candidate can be calculated using equation 3.7, where S is the set of all discrete coordinates that the driven path will cover.

$$\text{PR}_{expected} = W_c * \eta_p * \text{NA}_{avg} * \frac{L_{tot}}{T_{tot}} \tag{3.5}$$

$$T_{tot} = \sum_{0}^{L_{tot}} V(s)^{-1} \Delta s \tag{3.6}$$

$$\mathrm{NA}_{avg} = \frac{1}{|S|} \sum_{(x,y)\in S}^{N} \mathrm{NA}(x, y) \tag{3.7}$$

Substituting equation 3.4 and 3.5 in equation 3.3 results in the following definition of C_{nod}:

$$C_{nod} = 1 - \frac{\mathrm{NA}_{avg} * L_{tot}/T_{tot}}{\mathrm{NA}_a * V_{cruise}} \tag{3.8}$$

3.1.5. Combining the cost functions

The costs C_{obs}, C_{dist}, and C_{nod} are combined linearly into the total cost of a path, as can be seen in equation 3.9. To change priority between C_{dist} and C_{nod}, the variable u_c is introduced. By choosing u_c between 0 and 1, more priority can be given to either of the affected objectives.

$$C_{tot} = C_{obs} + u_c * C_{dist} + (1 - u_c) * C_{nod} \tag{3.9}$$

An important addition needs to be made for the case where all path candidates collide with an obstacle. In this case, following the research by Chu et al. [5], the collector should follow the path where the collision happens the furthest away.

3.1.6. Path candidate optimization

Each timestep, the goal is to find the path candidate with the lowest associated cost C_{tot}. Every path candidate p_c can be uniquely defined by its final lateral deviation d_{final} from the path to follow P_F. d_{final} should not exceed the limit set by the physical design of the VTS, d_{max}. For each path, the total cost C_{tot} can be calculated using equation 3.9. The resulting optimization problem is as follows:

$$\text{Minimize } C_{tot} \text{ subject to } |d_{final}| \leq d_{max} \tag{3.10}$$

The equation for C_{tot} is nonlinear and non-differentiable. Additionally, the only input variable is d_{final}. Therefore, finding p_c with the lowest C_{tot} is a single-variable continuous nonlinear non-differentiable optimization problem.

While there are approaches to iteratively solving this problem, this research uses the method used by Chu et al. [5]. This method approximates the global optimum by calculating the costs for a discrete set of paths, using the same set of lateral deviations at each timestep. The values for d_{final} are specified in section 3.2.5.

3.2. Generation of path candidates

Path candidates are generated in three different ways, as described in section 3.2.3 and 3.2.4. The paths are based on cubic splines, from which the background is explained in section 3.2.1 and section 3.2.2.

3.2.1. Cubic spline

Following the definition from Chu et al. [5], a 2D parametric cubic spline is described by the following formula:

$$\begin{cases} v_x(t) = a_x t^3 + b_x t^2 + c_x t + d_x \\ v_y(t) = a_y t^3 + b_y t^2 + c_y t + d_y \end{cases} \tag{3.11}$$

or in general:

$$v_i(t) = a_i t^3 + b_i t^2 + c_i t + d_i \tag{3.12}$$

$$v_i'(t) = 3a_i t^2 + 2b_i t + c \tag{3.13}$$

$$v_i''(t) = 6a_i t + 2b_i \tag{3.14}$$

where t is a unitless parameter defining the shape of the curve, which does not represent in any way the physical parameter Time. a_i, b_i, c_i and d_i are the coefficients of the polynomial that further describe the shape of the curve. The coefficients can be determined by adding constraints to the cubic spline. No clear guidelines within the literature have been found, so for this study, the constraints are defined by the start position and direction at $t = 0$, and end position and direction at $t = 1$.

$$v_i(0) = v_{start,i} \tag{3.15}$$

$$v_i(1) = v_{end,i} \tag{3.16}$$

$$v_i'(0) = u_{start,i} * C_{curvature} * L_{spline} \tag{3.17}$$

$$v_i'(1) = u_{end,i} * C_{curvature} * L_{spline} \tag{3.18}$$

$$L_{spline} = \|v_{end} - v_{start}\| \tag{3.19}$$

The vectors v_{start} and v_{end} are the vectors pointing towards the start and endpoint of the cubic spline, respectively. Meanwhile, u_{start} and u_{end} represent the normalized vectors describing the directions at the start and endpoint. The roundness of the path is determined by $C_{curvature}$ and L_{spline}, where L_{spline} signifies the length between the start and endpoint, serving as a factor to render the spline shape independent of its size. The vectors that define a cubic spline, and the impact of constant $C_{curvature}$ is illustrated in figure 3.3. The figure shows that preferable paths are achieved when $C_{curvature}$ is set to 1.

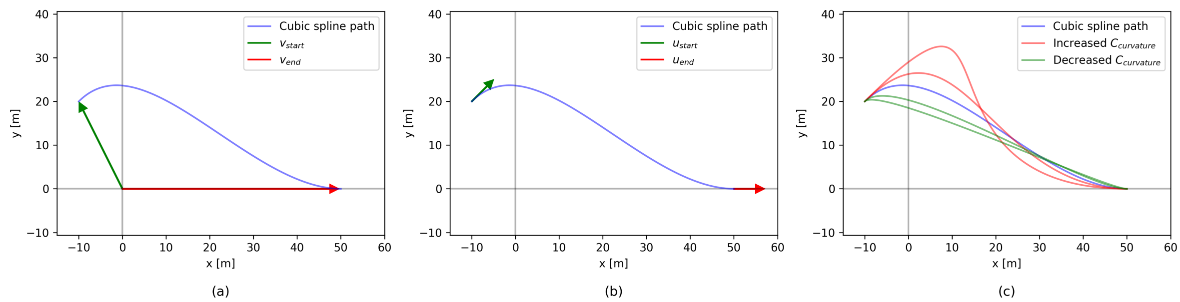

Figure 3.3: Visualization of the parameters used for the creation of a cubic spline path. (a) shows vectors v_{start} and v_{end}, (b) shows direction vectors u_{start} and u_{end}, and (c) shows the influence of curvature constant $C_{curvature}$.

From the cubic spline definition of equation 3.11, the curvature of the spline κ can be calculated for each value of $t = [0, 1]$ using equation 3.20 [5]. The curvature can be transformed in the turning radius using equation 3.21. The turning radius of the curve is used in equation 3.29 for the calculation of the collector's velocity.

$$\kappa(t) = \frac{v'_x(t)v''_y(t) - v''_x(t)v'_y(t)}{(v'_x(t) + v'_y(t))^{3/2}} \tag{3.20}$$

$$r(t) = \frac{1}{\kappa(t)} \tag{3.21}$$

3.2.2. Arc length parameterization

One of the difficult parts of working with parametric curves such as the cubic spline is the parameter t, as it has no physical meaning. Incrementally increasing t does not iterate over the spline in equal arc lengths, as can be seen in figure 3.4. However, in characterizing movement along the curve, establishing a relationship between parameter values and the arc length becomes crucial. This is called arc length parameterization, and the used method is grounded in the research contributions of Guenter and Parent [12], as well as Wang et al. [35].

The arc along a cubic spline between t_0 and t_1 can be calculated using equation 3.22. This integration is performed using the `quad` function from the `scipy.integrate` module in Python. This function implements a technique from the QUADPACK library, a collection of Fortran subroutines, for numerical integration. The `quad` function attempts to achieve an accuracy where the absolute error between the integral and the numerical approximation is smaller than $\max(\epsilon_{abs}, \epsilon_{rel} * |I|)$, where I is the integral of the function, and ϵ_{abs} and ϵ_{rel} are the absolute and relative error tolerances. Figure 3.5 shows a visualization of points on a cubic spline, evenly spaced along the arc length.

$$s(t) = \int_{t_0}^{t_1} ((v'_x(t)^2 + v'_y(t)^2)^{1/2} dt \tag{3.22}$$

Performing the integration for arc length calculation each time, or, conversely, determining the t at a specific arc length proves inefficient. To address this, the relationship between s and t is approximated using a subdivision table, as proposed by Guenter and Parent [12]. With N_{sub} subdivisions, the arc length is computed with $t_0 = 0$, and for each subsequent $t_1 = t_i$ defined in equation 3.23. The resulting arc lengths are then stored for these values. Subsequently, the arc lengths between the calculated values are approximated by linear interpolation, achieved through the `interp1d` function from the `scipy.interpolate` module. By establishing the relationship between arc length s and parameter t, the spline can now be expressed as a function of its arc length, thereby enhancing its utility for the path planner.

$$t_i = \frac{i-1}{N_{sub}-1}, \quad \text{for } i = 1, 2, \ldots, N_{sub} \tag{3.23}$$

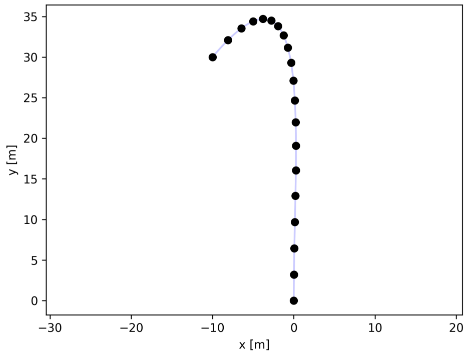

Figure 3.4: Points on a cubic spline, evenly spaced in parameter t.

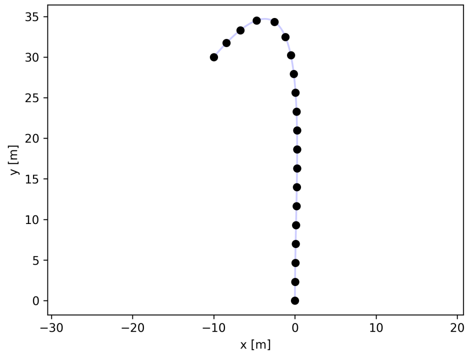

Figure 3.5: Points on a cubic spline, evenly spaced along the arc length.

3.2.3. Curvilinear path proposal method

The method to create path candidates for the ICP is based on the research by Chu et al. [5]. This method works using the following steps:

1. Transform the collector location and direction into the curvilinear space of the global path.
2. Within the curvilinear space, propose paths as a cubic spline from the initial position and direction of the collector to a distance $D_{lookahead}$ meter ahead. Propose multiple paths with final lateral offsets d_{final} as defined in section 3.2.5.
3. Transform each path candidate back into Cartesian space.

The process of creating path candidates using the curvilinear path proposal method can be seen in figure 3.6.

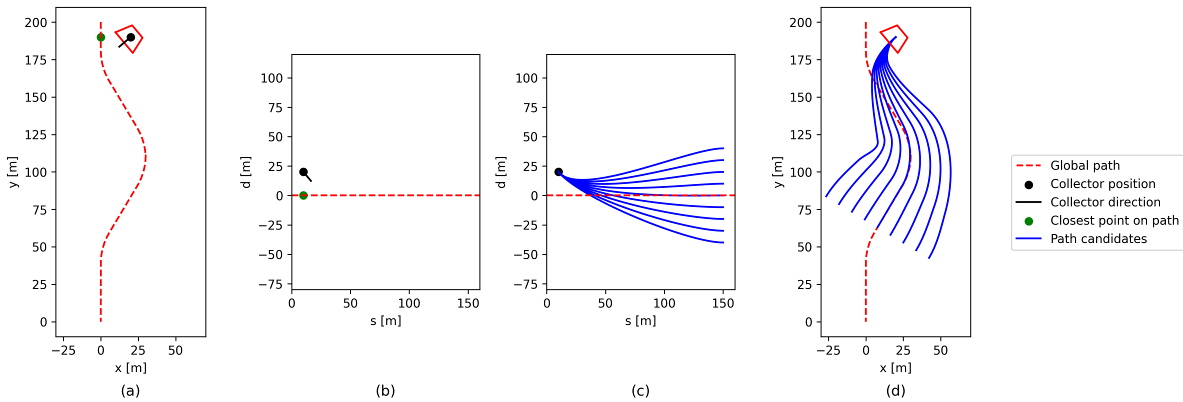

Figure 3.6: Visualization of the process of creating curvilinear path candidates. (a) shows the initial position of the collector and the global path in Cartesian space. (b) shows the collector position transformed into curvilinear space. (c) is a visualization of the path candidates in curvilinear space, and (d) shows the path candidates transformed back into Cartesian space.

As noted by Chu et al. [5], one limitation of this method is the fact that paths cannot deviate more from a given global path than the radius of the curvature of the global path r. A lateral distance d larger than r results in the path candidate moving in the opposite direction of the global path. Figure 3.7 shows three examples of paths that are parallel in curvilinear space. Paths where $d > r$ should be discarded, following the procedure set by Chu et al. [5].

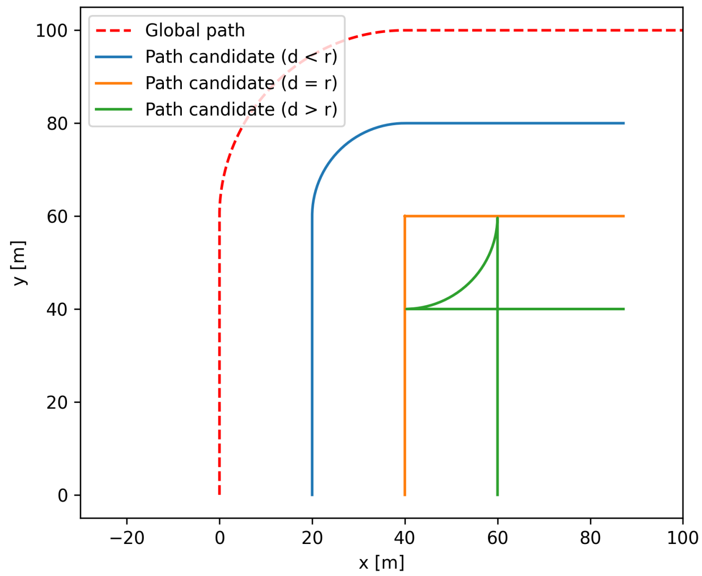

Figure 3.7: Three examples of paths that are parallel in curvilinear space. All paths where $d > r$ should be discarded.

3.2.4. Local and global orthogonal path proposal methods

To omit the path pruning limitation of the curvilinear path proposal method, two simplified models are also taken into consideration. These have been named the local orthogonal and global orthogonal path proposal methods. Both methods propose cubic spline paths straight in the Cartesian space, based on two points.

The local orthogonal path proposal method works as follows:

1. Find the closest point on the global path.
2. Find the point on the global path $D_{lookahead}$ meter ahead.
3. Propose paths perpendicularly to the global path in that point ahead using the lateral offsets as described in section 3.2.5, and using the direction of the global path at the point ahead.

The global orthogonal path proposal method works in a similar way to the local orthogonal method, as it also creates path candidates based on two points. However, it makes use of the larger direction of the global path:

1. By examining the start and endpoint of the global path, find the general direction of the global path $\mathbf{v}_G$.
2. Find the intersection of the global path, and the line that both crosses the collector location and is perpendicular to $\mathbf{v}_G$.
3. Find the point on the global path $D_{lookahead}$ meter ahead of the found point.
4. Propose paths perpendicularly to $\mathbf{v}_G$ in that point ahead using the lateral offsets as described in section 3.2.5.

A visualization of both path proposal methods can be seen in figure 3.8.

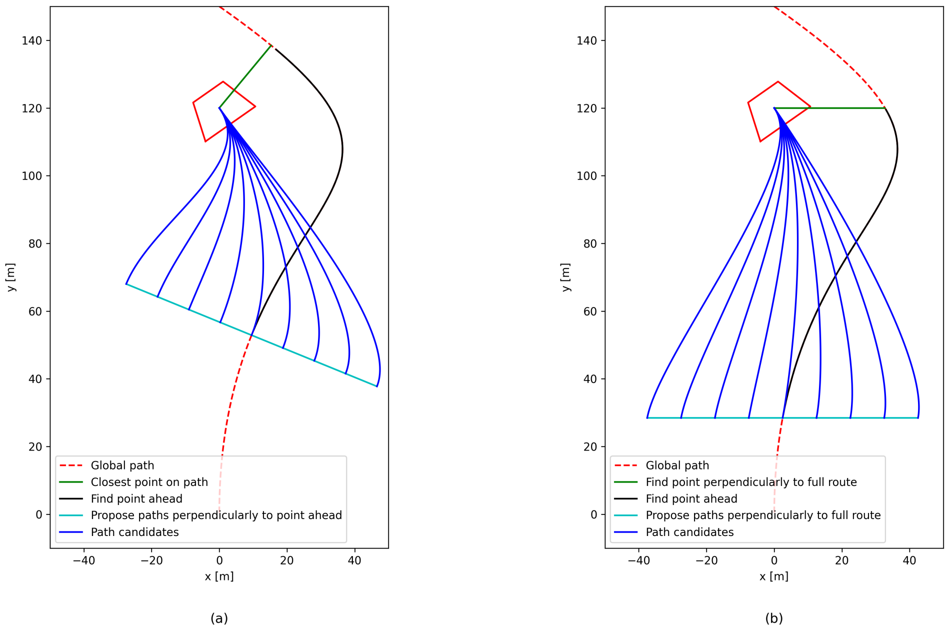

Figure 3.8: Visualization of two path proposal methods for a hypothetical scenario. (a) shows the local orthogonal path proposal method. (b) shows the global orthogonal path proposal method.

3.2.5. Lateral offset of path candidates

The lateral offsets of the path candidates d_{final} are set to a range of values. As specified in section 3.5, the collector cannot deviate more than 100 meters from the global path. Therefore, the maximum lateral offset is chosen to 100 meters.

Furthermore, a nonuniform distribution of d_{final} is chosen along the 100 meters. Increasing the amount of path candidates has a direct impact on the simulation speed. Because of this, and because the collector should especially make precise movements closer to the path to follow, a higher path candidate density is chosen for smaller lateral deviations. Specifically, the path density ranges from a 1 meter interval for $|d_{final}| \leq 10$ m to a 10 meter interval for $|d_{final}| \geq 50$ m.

3.3. Environment and sensor representation

In section 3.3.1 to 3.3.4, it is shown how the measured topology of the deep-sea is stored and updated during simulation. Section 3.3.5 shows how obstacle detection is performed.

3.3.1. Environment representation

The deep-sea environment can be represented as either two-dimensional or three-dimensional. A three-dimensional environment can add complexity within the simulation for dynamics and more realistic sensor measurements. However, the focus of this thesis is local path planning for a nodule collector. Dynamics of the collector like slip, pitch and roll are not taken into account. And while a complex acoustic sensor simulation could make the model more realistic, a two-dimensional approximation will suffice. For this reason, a two-dimensional environmental representation is chosen for this research.

The ground truth for the environment, $\mathbf{E}_T$, is represented as a two-dimensional array with a resolution ρ_T of 1 meter. Each entry in the array $e_{T,(x,y)}$ represents the true height of the sea-floor at location (x, y). Within a simulation, the collector keeps track of the measured environment $\mathbf{E}_M$, which is an array of the same size and resolution as $\mathbf{E}_T$. Each timestep during a simulation, $\mathbf{E}_M$ is updated to better approximate $\mathbf{E}_T$.

3.3.2. Presurvey map creation

The measured environment $\mathbf{E}_M$ that the collector starts a simulation with is the presurvey map $\mathbf{E}_P$. This map is created from presurvey bathymetric measurements performed by an AUV. The resolution of these measurements ρ_{pre} is larger than the ground truth resolution ρ_T, as a more accurate ρ_{pre} is directly correlated to higher AUV costs.

For a given $\rho_{pre} = N\rho_T$ and $\mathbf{E}_T$, the presurvey map $\mathbf{E}_P$ can be determined by the following steps:

1. Split the map into blocks of size N by N.
2. For each block with bottom left corner (X_b, Y_b), calculate the mean of the true heights using equation 3.24.

$$\mu_b = \frac{1}{N^2} \sum_{i=X_b}^{X_b+N} \sum_{j=Y_b}^{Y_b+N} e_{T,(i,j)} \tag{3.24}$$

3. Create a mesh that places all means in the center of each block.
4. Perform bivariate spline interpolation using the created mesh to determine $\mathbf{E}_P$.

Within the developed simulator, the `RectBivariateSpline` class from the `scipy.interpolate` module is used for step 4. A visualization of 1 slice of $\mathbf{E}_T$, the bivariate spline and resulting $\mathbf{E}_P$ can be seen in figure 3.9.

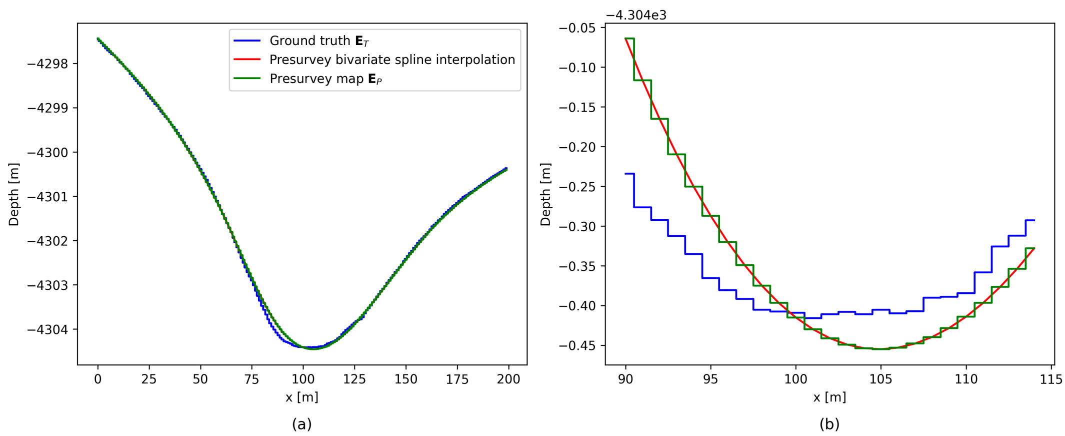

Figure 3.9: Visualization of a slice of the ground truth environment $\mathbf{E}_T$ and the presurvey map $\mathbf{E}_P$ resulting from the bivariate spline. (a) shows the full slice, and (b) shows a section of the slice.

3.3.3. Noise level modeling

The environment surrounding the collector is characterized by the presence of noise generated by both the VTS and the collector itself, thereby hindering the functionality of acoustic sensors such as the MBES. Furthermore, the surrounding sediment plume consists of suspended particles in the water, which change the acoustic properties of water and worsen the quality of performed measurements. To precisely and truthfully model the noise level within the environment and the acoustic sensor interference, too many contributing factors have to be taken into account for this research.

This thesis simplifies the environmental noise level as a single time-dependent variable $N_e(t)$. This variable is defined as a pulse wave function with total period $T_N = T_{noise} + T_{noiseless}$, where T_{noise} and $T_{noiseless}$ are parameters specifying the durations of noise presence and absence, respectively. The duty cycle of the pulse wave is characterized by T_{noise}/T_N. This lead to the following equation for determining the noise level:

$$N_e(t) = \begin{cases} 1 & \text{if } 0 \leq t \bmod T_N < T_{noise} \\ 0 & \text{else} \end{cases} \tag{3.25}$$

This variable influences two processes. Firstly, it influences the accuracy of performed sensor measurements, as described in section 3.3.4. Secondly, it determines if the previous track is detected. This is further explained in section 3.4.2.

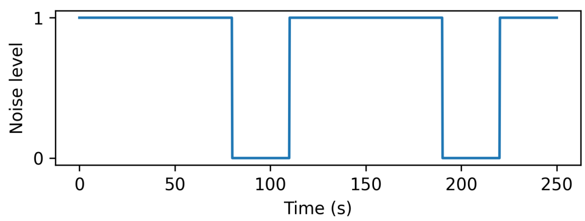

Figure 3.10: Visualization of $N_e(t)$ over time for $T_{noise} = 60$ and $T_{noiseless} = 30$.

3.3.4. Sensor modeling

A novel addition of this thesis is the consideration of live sensor inputs into the simulator. The collector measures the topology of the surrounding environment through a MBES in front of the collector. It measures the topology by emitting acoustic pulses towards the sea-floor and calculating the depth based on the reflected waves. For accurate modeling of these waves and reflections, a three-dimensional environment would be needed. However, as this thesis uses a two-dimensional environment, an approximation is needed.

The sensor's reach is approximated as a two-dimensional conical shape in front of the collector, characterized by the angle of the cone Θ_s and a sensor range R_s. In accordance with specifications from Kongsberg MBESs and practical insights from Allseas, Θ_s is set at 140°, with $R_s = 45$ m.

Each timestep, the measured environment $\mathbf{E}_M$ is updated using the local sensor measurements. Let S_M represent the set of discrete coordinates covered by the sensor cone. These coordinates are then set to be equal to the corresponding ones in the ground truth environment $\mathbf{E}_T$.

$$e_{M,(x,y)} = e_{T,(x,y)} \forall (x,y) \in S_M \tag{3.26}$$

The uncertainties of the measurements are individually stored in a two-dimensional array $\mathbf{U}_M$ matching the dimensions of $\mathbf{E}_M$. Each entry $u_{M,(x,y)}$ within $\mathbf{U}_M$ denotes the uncertainty associated with a specific measurement. This value, $u_{M,(x,y)}$, serves as a basis for adding a buffer to any obstacle detected at (x,y), as explained in section 3.3.5.

Given a measurement at (x,y) and at time t, the sensor uncertainty is modeled in relation to the distance to the collector $R_{col}(x,y)$ and the environmental noise $N_c(t)$. First, for a coordinate in S_M, express $R_{col}(x,y)$ with respect to the collector location (x_c, y_c) using equation 3.27. Then, given the environmental noise level $N_e(t)$ as defined in section 3.3.3, the uncertainty of a single measurement u_M at location (x, y) at time t is given by equation 3.28 and is visualized in figure 3.11.

$$R_{col}(x, y) = \sqrt{(x - x_c)^2 + (y - y_c)^2} \tag{3.27}$$

$$u_M(x, y, t) = \begin{cases} u_{R,noise} * R_{col}(x, y) + u_{0,noise} & \text{if } N_e(t) = 1 \\ u_{R,noiseless} * R_{col}(x, y) + u_{0,noiseless} & \text{else} \end{cases} \tag{3.28}$$

The initial environment is generated solely by presurvey measurements, where the uncertainty is denoted as u_P. Throughout the simulation, the measurement uncertainty at location (x, y) is updated only if the new uncertainty is smaller than the preceding measurements.

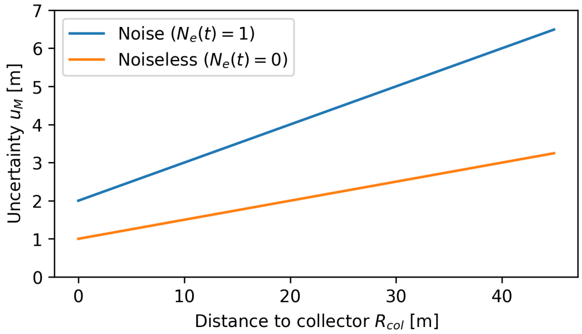

Figure 3.11: Visualization of the measurement uncertainty u_M as a function of the noise level and distance to the environment, as defined in equation 3.28.

3.3.5. Obstacle detection

Obstacle detection is done on the measured map, based on the following criteria as defined by Allseas:

1. Anything higher than 0.3 m is an obstacle
2. a slope of larger than 4 °for longer than 3 meter is an obstacle

To take the measurement uncertainty into account, obstacles detected at each location (x, y) are buffered by $u_{M,(x,y)}$ meter. As a result, if the measurement is performed with a low uncertainty, the collector can drive more closely to the actual obstacle. Conversely, if the measurement uncertainty is high, the collector will avoid the true obstacle with a greater margin.

3.4. Path to follow

Before DSNC operation, a global path P_G is created based on presurvey measurements. However, during operation, the previous track P_{PT} should also be considered to optimize area coverage. Following the path next to the previous track, P_{NPT}, will result in maximal area coverage, as it minimizes the amount of nodules left between the tracks. However, there are three issues with that method of driving:

1. In reality, the previous track is not always detected.
2. In specific cases around obstacles, P_G should be followed instead of P_{NPT}, as visualized in figure 3.12.
3. If the previous track contains many turns, driving exactly next to the previous track will result in a decreased production rate.

These issues are unique for the application of DSNC, and a method needs to be designed to handle this problem. Section 3.4.1 describes how the global path P_G is created based on presurvey measurements. Then, in section 3.4.2, it presents a novel method of deciding whether to use the global path or the previous track as input for the ICP.

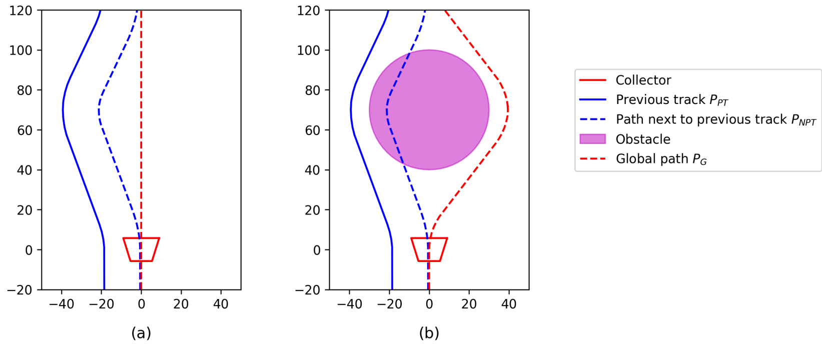

Figure 3.12: Two example scenarios showcasing how the path next to the previous track P_{NPT} should be used. (a) shows a scenario where following P_{NPT} can increase total area coverage by leaving no space between the tracks. (b) shows a scenario where the global path P_G should be followed instead of P_{NPT}.

3.4.1. Global path creation

For this research, a novel global path creation process is performed. There have been researches performed on creating a mining pattern for DSNC, as outlined in section 2.1.1. However, these methods only describe a method of setting up global paths within an area that does not contain obstacles. This is far from reality, where there are many obstacles present that should be considered by the global path planning algorithm.

The process used in this thesis is a modified version of the direction-parallel path planning method by Park et al. [22]. The parallel paths form a basis of the global paths, which are then modified to go around obstacles detected from the presurvey measurements. The full global path creation process is described in the following steps:

1. Based on a given presurvey map, start by proposing straight paths parallel to each other, in direction $\mathbf{v}_p$
2. Move each path around obstacles either clockwise or counterclockwise, whichever route is shortest.
3. Remove all sections of each path where the angle between the section and $\mathbf{v}_p$ is larger than Θ_{max}.
4. Round corners.

A visualization of this process for one of the global paths is shown in figure 3.13.

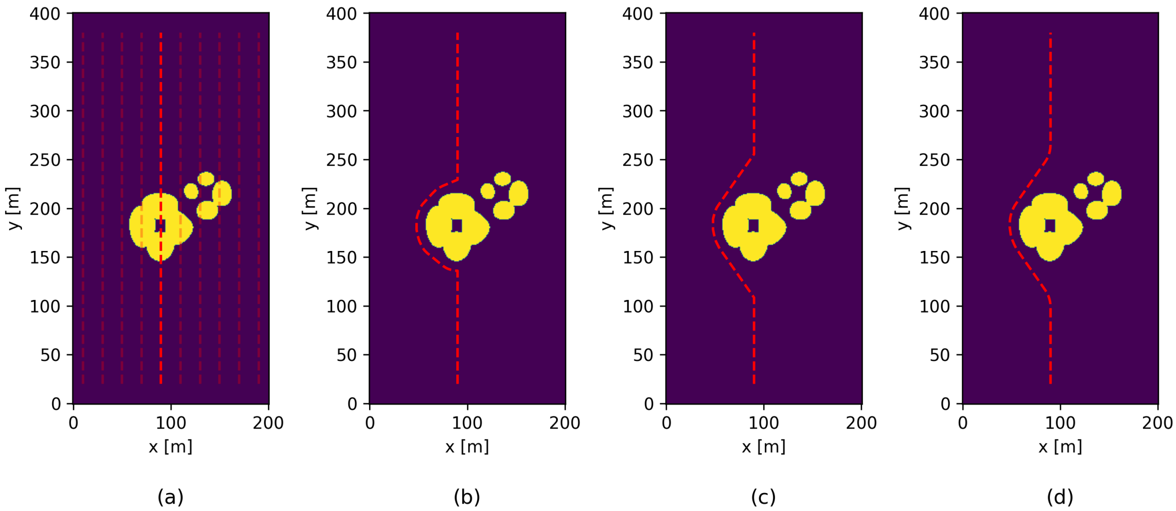

Figure 3.13: Visualization of the global path creation process. (a) shows the initially proposed straight paths in direction $\mathbf{v}_p$, highlighting one path from which the creation process is shown. (b) shows how the path is moved around obstacles. (c) visualizes how all sections are removed where the angle between each section and $\mathbf{v}_p$ is too large. Finally, corners are rounded, as visualized in (d).

3.4.2. Path to follow decision making method

As specified in section 3.1.1, the collector should follow both the pre-determined global path P_G and follow the path next to the previous track P_{NPT}. These objectives can be contradictory, as they tell the ICP to follow two different paths. To tackle this, one of the paths is chosen as the path that the collector should follow, P_F.

P_F can be equal to either P_G or P_{NPT}, depending on the following conditions:

- If the noise level of the environment $N_e(t)$ is high, the previous track cannot be detected and the global path should be followed. $P_F = P_G$.
- If the distance from the collector to the previous track P_{PT} is larger than the sensor range R_s, the previous track cannot be detected and the global path should be followed. $P_F = P_G$.
- To handle both situations from figure 3.12, the directions of P_{NPT} and P_G are compared. First, find the point closest to the collector on both P_{NPT} and P_G. Then, find the direction of both paths $D_{lookahead}$ meter ahead. If the heading difference of each path at that point ahead is larger than a minimum angle α_{min}, it can be derived that both paths are going in a different direction and the global path should be followed. $P_F = P_G$.
- If the previous conditions are not met, the path next to the previous track should be followed. $P_F = P_{NPT}$

3.5. Assumptions and constraints

The following assumptions are made about the environment, the collector and the parts connected to the collector:

- The nodule abundance is assumed to be constant and equal to NA_a over the whole test area, except for the parts where the collector has already driven, where it is 0.
- The size of the collector is 12 x 18 x 6 m (LxWxH).
- The position of the collector is known exactly. This is a large assumption to be made, as positioning in the deep-sea is far from perfect. However, when DSNC operation begins, it is likely that the position of the collector will be more certain due to optimized acoustic positioning sensors and SLAM on local features.
- In accordance with specifications from Kongsberg MBESs and practical insights from Allseas, the sensor cone angle Θ_s is set at 140°, and the sensor range R_s is set to 45 meters.
- The collector can follow a proposed path exactly.
- To safeguard the connection to the VTS, the collector should not deviate more than 100 meters from the global path.
- Pitch, roll, and vertical movements are assumed to be negligible.
- Vehicle dynamics are not considered, and velocity is approximated as a function of the turning radius r of a given path candidate $p_{c,i}$, as given by equation 3.29. This function is visualized in figure 3.14.

$$V(r) = \begin{cases} V_{cruise} & \text{if } r > R_{cruise} \\ \frac{V_{crawl}}{R_{crawl}} \cdot r & \text{if } r < R_{crawl} \\ V_{crawl} + \frac{V_{cruise} - V_{crawl}}{R_{cruise} - R_{crawl}} \cdot (r - R_{crawl}) & \text{otherwise} \end{cases} \tag{3.29}$$

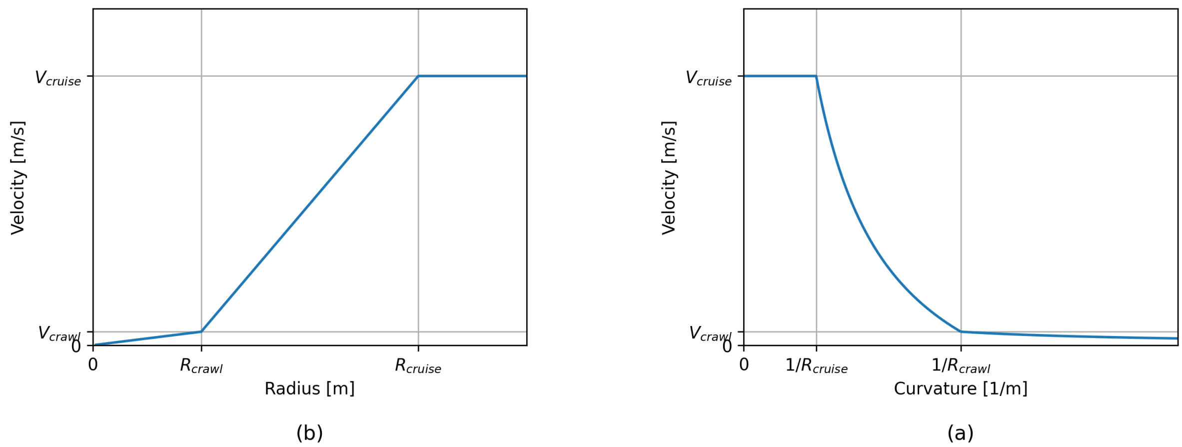

Figure 3.14: Visualization of the collector velocity V. (a) shows V as a function of the turning radius, and (b) shows V as a function of the curvature of the path.

4
Experiments

4.1. Experimental setup

In this section, the main setup of the experiments is described.. In sections 4.1.1, 4.1.2 and 4.1.3, the process of creating the initial test environment is described. In section 4.1.4, the variables that are changed in the experiments are described. Section 4.1.5 describes the used metrics to compare several test configurations, and section 4.1.6 describes how optimality is approximated. Finally, the general structure of the code is described in section 4.1.7.

4.1.1. Test locations and shape

One of the contributions of this study is that real-life deep-sea environmental information is used. Allseas performed high quality bathymetric measurements of an area in the CCZ of 150 km^2, which can be seen in figure 4.1.

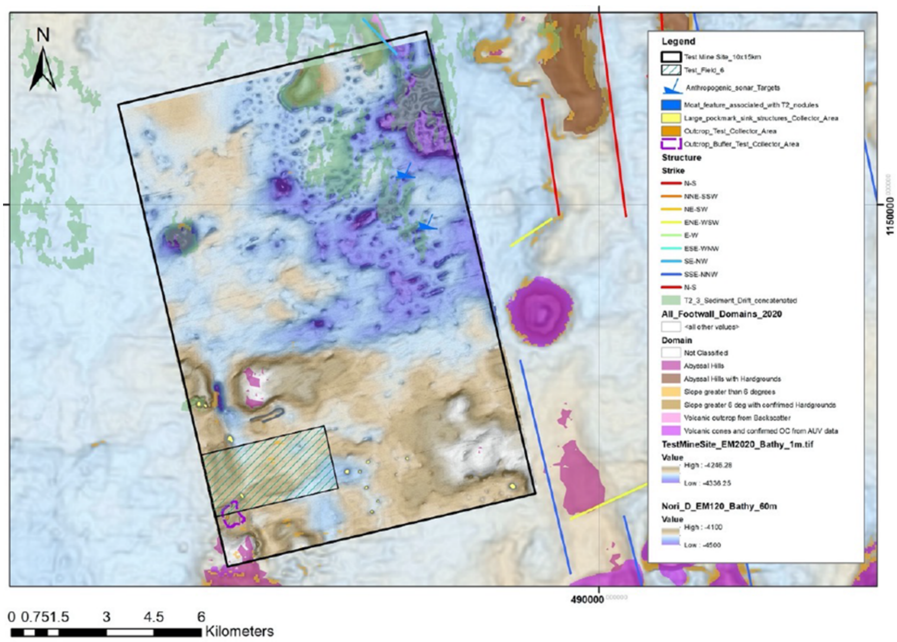

Figure 4.1: Bathymetric data of the measured area in the CCZ.

From this well-mapped area, a representable and interesting test location is chosen. This area can be seen in figure 4.2. The area has a length of 1 km and a width of 285 m. Using the global path creation method described in section 3.4.1, the collector will drive 15 times back and forth over the found test area. 15 passes, with a collector width of 18 m and a distance between tracks of 1 m, results in the map width of 285 m.

The sides of the test area should not be counted as an untraversable obstacle, as this is not representative of the real situation on the deep-sea floor. Therefore, a 200 m buffer is added on both sides of the map to allow avoidance maneuvers. However, this area is does not count for the total area coverage. The collector takes this into account by assuming that there are no nodules present on the buffer zone. This results in a lower average nodule abundance NA_{avg} for path candidates that partly go in the buffer zone, following equation 3.7. 2 buffers of 200 m and a map width of 285 m results in a total map width of 685 m.

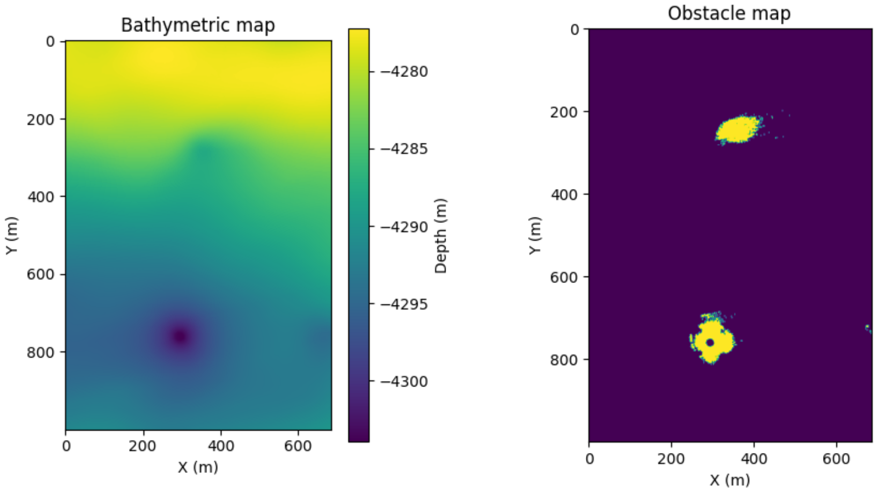

Figure 4.2: Bathymetric data and corresponding obstacle map of the test area.

For experiments four and five, four larger test areas are chosen from the high quality bathymetric map. These areas have the same width as the test area mentioned before, but contain a length of 2 km. The creation process of these larger test areas are further explained in section 4.5.1.

4.1.2. Environment preprocessing

The bathymetric data provided by the Survey department of Allseas has a resolution of 27 cm. However, due to imperfections such as missing values and measurement noise, preprocessing is needed before integrating the data into the simulator.

Firstly, missing values are addressed through a row-by-row iteration process. Each missing value is systematically replaced with the mean of its neighboring values. This interpolation results in a reasonable replacement for the missing value.

Following standard protocols from the Survey department of Allseas, the bathymetric map is downsampled. This is done by calculating the means for blocks of 4 by 4 measurements, combining 16 measurements into a single datapoint. This downsampling significantly reduces noise from the raw bathymetric data. The resultant map has a resolution initially reported as precisely 1.08 meters, and for the subsequent analyses, it is pragmatically assumed to be a true 1-meter resolution.

The presurvey map specifying the collector's initial knowledge of the topology is created using the process specified in section 3.3.2. The presurvey resolution for experiment 1 to 3 is set to 25 meters.

4.1.3. Global path of the test area

The global paths for the test area are created from the presurvey map using the method described in 3.4.1. Figure 4.3 shows how the global paths are planned around the obstacles measured on the presurvey map. The global route and the presurvey map form the basis for the ICP in experiment one to three.

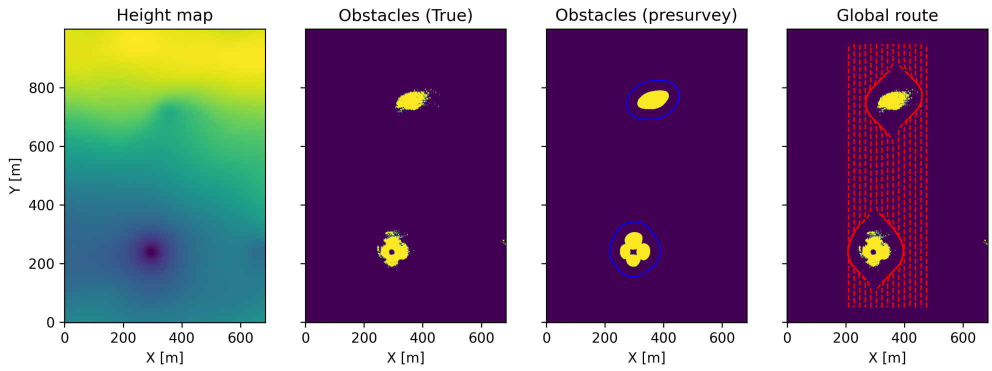

Figure 4.3: Visualization of how the global path is created from the original height map using a presurvey resolution of 25 meters.

4.1.4. Variables

Throughout the experiments, multiple variables are modified. The following variables within the local path planner are changed:

1. The path proposal method. Experiment 1 examines the curvilinear, local orthogonal and global orthogonal methods, as described in section 3.2.3 and 3.2.4.
2. ΔT, the time step of the simulation in seconds. This variable is examined in experiment 2.
3. u_c, the distribution of weights of the costs, as seen in equation 3.9. u_c can be any value between 0 and 1, and its effect on the performance of the ICP is examined in experiment 3.
4. $D_{lookahead}$ in m, the path proposal distance as defined in section 3.2.3 and 3.2.4. This variable can be any positive number, and its effect is examined in experiment 3.

Furthermore, the following environmental parameters are changed:

1. Presurvey resolution ρ_{pre} in m. This influences both the collector's initial knowledge of the topology, and the creation of the global paths, as described in section 3.3.2. The performance of the ICP is tested along different presurvey resolutions in experiment 4.
2. T_{noise} and $T_{noiseless}$, as defined in section 3.3.3. For experiments 1 to 4, T_{noise} is set to 100 seconds, and $T_{noiseless}$ is set to 10 seconds. This is done to make the obstacle uncertainty play a larger role during the simulation. However, it does influence the ability to follow the previous track, as defined in section 3.4.2. The influence of other values of T_{noise} and $T_{noiseless}$ is further examined in experiment 5.

4.1.5. Performance metrics

Each datapoint corresponds to an entire simulation executed with a specific configuration of the variables outlined in section 4.1.4. The performance metrics captured for each test include:

1. **Collision occurred:** A boolean value indicating whether a collision occurred during the test.
2. **Total area coverage (in m^2):** This metric calculates the overall area covered by the collector, considering that areas covered multiple times are counted only once. Given the unknown nodule abundance distribution, total effective area coverage serves as a valuable indicator of expectations.
3. **Mean area coverage per second (in m^2/s):** This metric is computed by dividing the total effective area coverage by the total time of the test. It represents the mean area covered by the collector per second, aligning with the overarching goal of maximizing nodule collection. Assuming constant nodule abundance across the entire area, this metric offers insight into the production rate of the collector.

These metrics are subsequently compared against the following benchmarks:

1. **Expected Performance Based on the Global Path ("Baseline"):** Each simulation is compared against the expected performance derived from the global path created from the presurvey

measurements. During actual DSNC operation, this global path will also serve as a basis for calculating the projected performance on a given mining area. However, a problem with this performance metric is that a global path, created from presurvey measurements, could overlap with obstacles. This makes it not always a fair comparison against the ICP, which actively navigates around obstacles.

2. **Baseline Performance Based on a Perfect Global Path ("Oracle"):** The ICP performance is also be compared against a metric calculated by a global path that is created through the actual obstacle map. This route avoids all the obstacles in the environment, and represents the performance that the collector could achieve if the exact environment is known before operation. The performance metrics associated with the oracle global paths are shown in table 4.1. A visualization of the oracle global paths can be seen in appendix A.

Map	Total area covered [m^2]	Total time [s]	Mean area coverage per second [m^2/s]
Main test area	211305	35331	5.981
Large test area 1	458274	75987	6.031
Large test area 2	497240	75159	6.616
Large test area 3	473721	73854	6.414
Large test area 4	425368	72717	5.850

Table 4.1: Oracle global path performance

4.1.6. ICP parameter optimization

The ICP parameters can be optimized, so the ICP performs as well as possible on the performance metrics as defined in section 4.1.5. As shown in section 4.1.4, the ICP parameters consist of the path proposal method m_p, ΔT, u_c and $D_{lookahead}$.

Define $\phi_a(m_p, \Delta T, u_c, D_{lookahead})$ as the total area coverage of a certain ICP configuration, as percentage of the oracle. Additionally, define $\phi_{cps}(m_p, \Delta T, u_c, D_{lookahead})$ as the mean area coverage per second of a certain ICP configuration, as percentage of the oracle. As there are two objectives, the resulting optimality will be a Pareto front. Given the variable constraints and the constraint that collisions should be avoided at all times, this results in the following optimization problem:

$$
\begin{array}{ll}
\text{Maximize} & \phi_a(m_p, \Delta T, u_c, D_{lookahead}) \\
\text{and} & \phi_{cps}(m_p, \Delta T, u_c, D_{lookahead}) \\
\text{Subject to} & m_p \in \{\text{local orthogonal, global orthogonal, curvilinear}\} \\
 & 0 < \Delta T \\
 & 0 \leq u_c \leq 1 \\
 & 0 < D_{lookahead} \\
 & \text{No collision occurred}
\end{array}
$$

If an ICP will be implemented in the actual DSNC application, it will be necessary to look for an optimal solution. However, due to lack of existing research on local path planning for DSNC and the short timeframe of this thesis, this research focuses on exploring the influences of the recognized ICP parameters in several experiments. Through the experiments, optimality is approximated by choosing a model that has the highest mean area coverage per second. The total area coverage is examined to ensure that it remains within acceptable limits.

4.1.7. Code structure and simulation speed

The code is structured to resemble the simulation loop specified in chapter 3. An overview of the code structure can be seen in appendix B.

The time it takes for 1 simulation to run is dependent on the size of the map, the length of the runs and the chosen timestep ΔT. One test with $\Delta T = 20$ s on the test area of 1 km takes around 40 minutes. As a rule of thumb, halving ΔT will double the time needed for a run, and halving the map size will reduce the total time by half.

An overview of the duration of each function is shown in table 4.2 and 4.3. All functions have a near-constant duration, except the transformation of the obstacle map to polygon objects. The obstacle map is a two-dimensional array of the same shape as the measured environment $\mathbf{E}_M$, consisting of zeros and ones, where a 1 means that that location contains an obstacle. To ensure a path candidate does not overlap with an obstacle, the obstacles on the map need to be transformed into polygon objects. The duration of this process is heavily dependent on the amount of detected obstacles within range of the collector, resulting in the large duration range of this process. Unfortunately, there was not enough time to find a faster method that was just as robust.

Function	**Duration per timestep [s]**
Update bathymetric map	0.005
Update measured accuracy map	0.004
Detect and buffer obstacles	0.001
Obstacle map to polygon objects	[0.0012, 1]
Determine path to follow	0.0003
Propose paths	0.002
Calculate costs	0.24
Move forward on best path	0.0004
Total time per timestep	[0.25, 1.25] seconds

Table 4.2: Indication of the duration of each function per timestep within the main simulation loop.

Function	**Duration per timestep [s]**
C_{obs}	0.010
C_{dist}	0.000
C_{nod}	0.23
Total time per timestep	0.24 seconds

Table 4.3: Indication of the duration of the calculation of each cost function for all path candidates each timestep.

4.2. Experiment 1: Influence of path proposal method

4.2.1. Setup

This section aims to examine the influence of different path proposal methods on the performance metrics as described in section 4.1.5. The tested path proposal methods are the curvilinear, local orthogonal and global orthogonal methods as described in section 3.2.3 and 3.2.4.

For the other parameters, representable values are chosen:

1. $\Delta T \in \{20, 30\}$ s.
2. $u_c \in \{0.4, 0.5, 0.6\}$.
3. $D_{lookahead} \in \{75, 100, 125\}$ m.
4. $\rho_{pre} = 25$ m.

A timestep of 20 and 30 seconds is chosen as it allows for relatively quick test execution. u_c is set to values between 0.4 and 0.6, to equitably weigh C_{nod} and C_{dist}, as can be seen in equation 3.9. The path proposal distance is chosen to be in the range of 75 meters to 125 meters. This is done to plan slightly further than the sensor range of 45 meters, but not too far out of the sensor range. The presurvey resolution ρ_{pre} is set to 25 meters.

4.2.2. Results

As can be seen in figure 4.4, the mean coverage per second does not significantly for different path proposal methods. The most important difference can be seen in figure 4.5, as the local orthogonal and curvilinear path proposal methods both have had instances where the collector collided with an obstacle. A table with the results can be found in appendix C.

An example of a collision, with the collector using the local orthogonal proposal method, can be seen in figure 4.7. The collector got into a position where all of the proposed paths collide with an obstacle. In this case, the optimal path is the one that collides with the obstacle as late as possible, which is visualized by the outline of the area that the collector will cover. It can be seen that it drives over an obstacle. On the other hand, the global orthogonal and curvilinear methods are able to steer the collector around the obstacle, as can be seen in figure 4.8 and 4.6. This shows that the local orthogonal path planning method can not handle curves in the global path well, as opposed to the other two methods.

The curvilinear path proposal method also has instances where the collector collides with an obstacle. A limitation of the method is the pruning of paths on the inside of curves of the global path, as described in section 3.2.3 and in the research by Chu et al. [5]. When the global path only contains large turning radii, and when the deviation from the global path is small, this does not cause any issues. However, as seen in figure 4.9, the collector should steer away from the obstacle, but is unable to because those paths have been pruned. This is only a limitation of the curvilinear path proposal method, as it does not cause issues in the local and global orthogonal methods, as can be seen in figure 4.10 and 4.11.

Based on the limitations from the curvilinear and local orthogonal path proposal method, it is decided to use the global orthogonal path planning method for the next experiments. It is able to avoid obstacles consistently. The next experiments focus more on the area coverage and mean area coverage per second for each ICP instance.

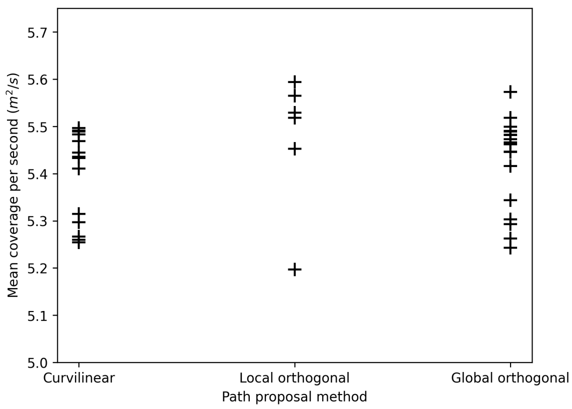

Figure 4.4: Mean coverage per second for the three path planning methods along different simulation configurations.

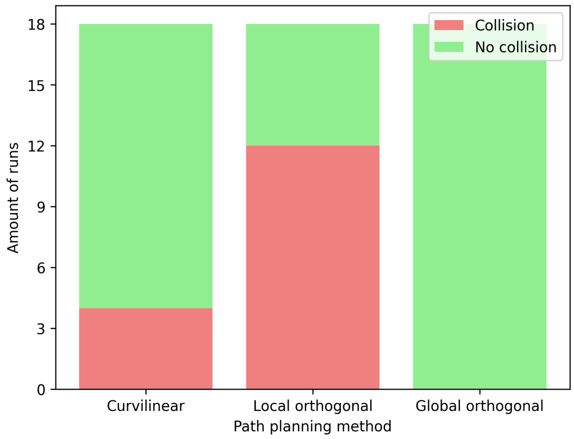

Figure 4.5: Collisions for the three path planning methods along different simulation configurations

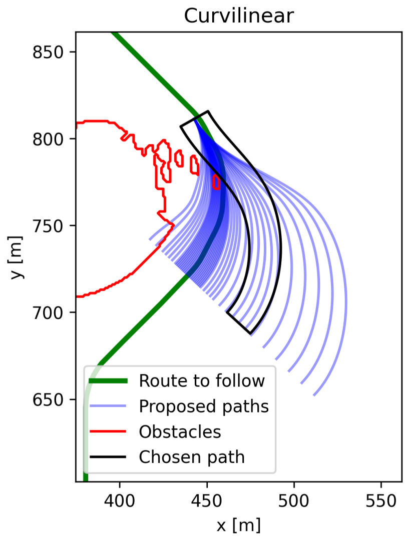

Figure 4.6: An example of paths proposed using the curvilinear path proposal method for the same collector location as in figure 4.7, resulting in a path that drives around the obstacle.

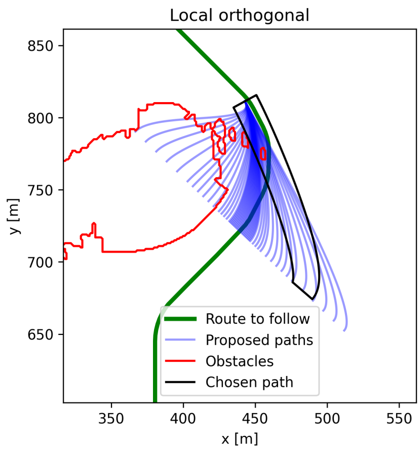

Figure 4.7: An example of paths proposed using the local orthogonal path proposal method, resulting in a collision.

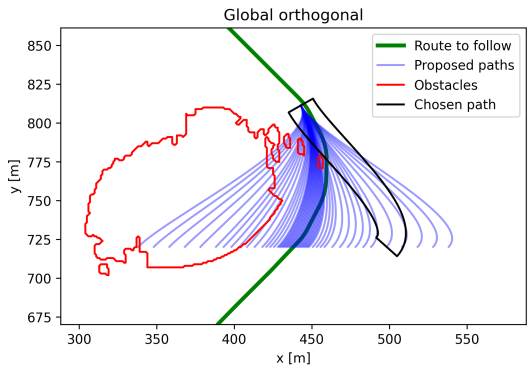

Figure 4.8: An example of paths proposed using the global orthogonal path proposal method for the same collector location as in figure 4.7, which results in a path candidate that steers clear of the obstacle.

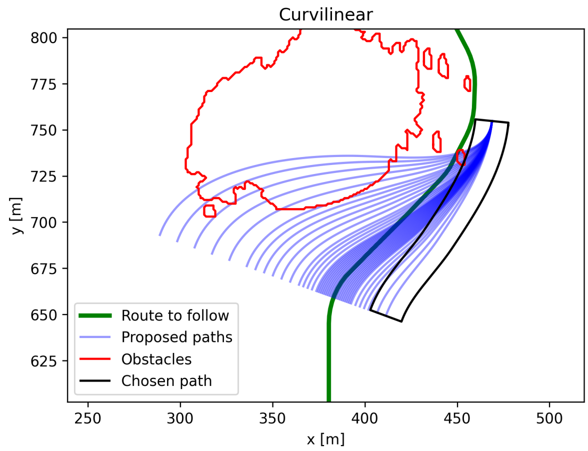

Figure 4.9: An example of path proposed using the curvilinear path proposal method. Paths on the inside of the corner are pruned, and all other paths result in a collision.

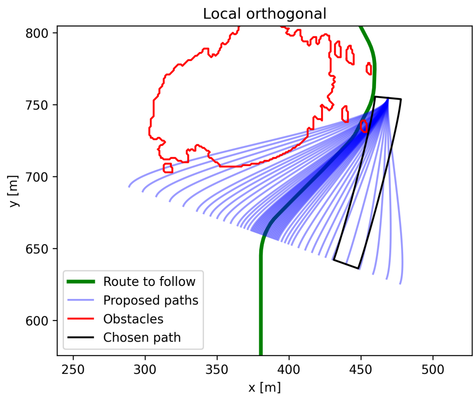

Figure 4.10: An example of paths proposed using the local orthogonal path proposal method for the same collector location as in figure 4.9, showing a path that drives around the obstacle.

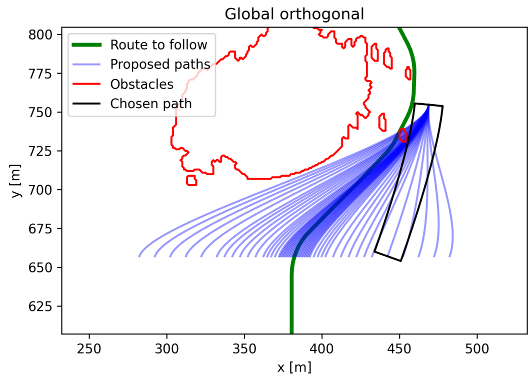

Figure 4.11: An example of paths proposed using the global orthogonal path proposal method for the same collector location as in figure 4.9, showing a path that drives around the obstacle.

4.3. Experiment 2: Influence of ΔT

4.3.1. Setup

One crucial decision involves determining a representable value for ΔT. In the practical application, the path planner should operate at the maximum speed feasible with the available technology. However, in the simulator, a larger timestep is preferable due to its faster execution. Also, given the collector's extremely slow velocity, optimizing path planning every second may not be imperative. The primary objective of the experiment is to assess the impact of varying ΔT on performance and understand how it influences the overall efficiency of the system.

The following parameters are chosen as ICP parameters:

- Global orthogonal path proposal method, as found in experiment 1.
- $\Delta T \in \{5, 10, 15, 20, 25, 30, 45, 60\}$ s.
- $u_c \in \{0.4, 0.6\}$.
- $D_{lookahead} \in \{75, 100\}$ m.

Similar to experiment 1, the values for u_c are set to either 0.4 or 0.6. This choice aims to equitably weigh C_{nod} and C_{dist}, as can be seen in equation 3.9. Likewise, consistent with Experiment 1, two values for $D_{lookahead}$—75 m and 100 m—are explored. These distances extend beyond the acoustic sensor range but remain sufficiently close for considering sensor measurements. For a more comprehensive examination of u_c and $D_{lookahead}$, please refer to section 4.4.

4.3.2. Results

As can be seen in figure 4.12, there is no large difference found in total area coverage along multiple values of ΔT. For some configurations, the total area coverage increases marginally. For example, using a configuration with u_c = 0.6 and $D_{lookahead}$ = 100 m, the collector covers a total area of 1.953e5 m^2 using a ΔT of 5 seconds, and 1.966e5 m^2 with a ΔT of 60 seconds. This indicates a small total area coverage gain of 0.64%. This small gain could be because with a larger timestep, the collector is slightly better at choosing a route that covers more area, but it is a very small difference. A table with the results can be found in appendix D.

A larger difference can be seen when looking at the mean area coverage per second. For all configurations, it shows a general decline in coverage per second when the timestep ΔT is increased. Especially for $\Delta T \geq 30$ s, the mean area coverage per second sharply decreases. This can be explained by the fact that a larger value of ΔT results in the collector having less time to respond to a detected obstacle. For example, a timestep of 45 seconds, combined with a cruising velocity of 0.4 meters per second, results in the collector traversing 18 meters per timestep, which is more than a third of the acoustic sensor range. Therefore, decreasing the ΔT significantly increases the available response time to any detected obstacles. This allows the collector to avoid any obstacles more gradually, and keep a high velocity for longer periods of time. This difference can be seen in figure 4.14.

As can be seen in figure 4.15, the driven routes for a low and high value of ΔT look almost identical. From this and figure 4.12, it can be concluded that the path planner makes the same path planning decisions along different values of ΔT. However, it makes those decisions slightly later and therefore less efficient with higher values of ΔT.

Another downside of large values of ΔT is the increased susceptibility to collisions. This can be explained by the fact that a large ΔT reduces the time that the collector has to respond to newly measured obstacles. One of the examined configurations resulted in a collision with $\Delta T = 60$ s. A visualization of a collided path can be seen in figure 4.16.

Though the total area coverage shows a marginal preference for larger timesteps, it comes with a higher chance of collisions and a decreased collection efficiency. With this information and the observation that the maximum coverage per second occurs at $\Delta T = 20$ s, a timestep of 20 seconds is selected for subsequent experiments.

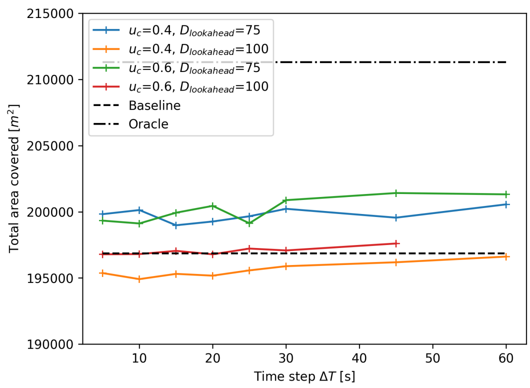

Figure 4.12: Total area coverage along several ΔT, with different ICP configurations.

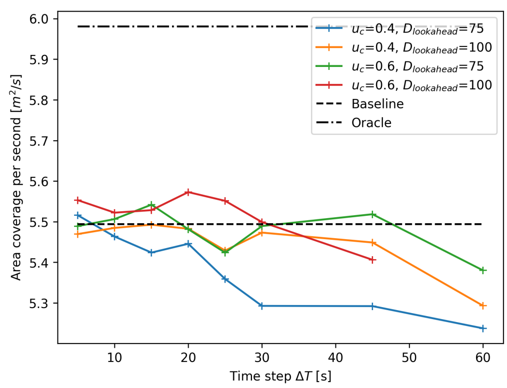

Figure 4.13: Mean area coverage per second along several ΔT, with different ICP configurations.

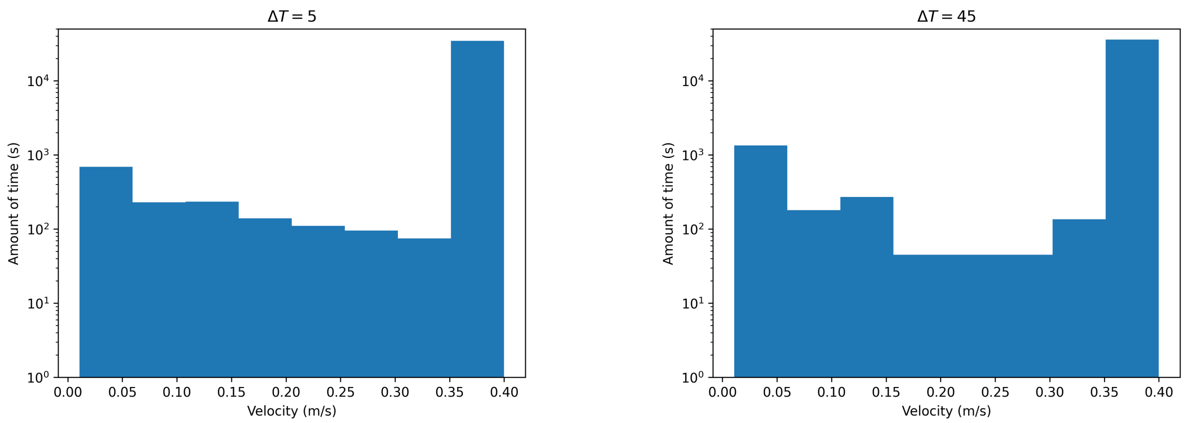

Figure 4.14: Velocity profile of the collector during a simulation with a low value of ΔT on the left, and a high value of ΔT on the right. With a higher ΔT, the collector drives more often with a very low velocity.

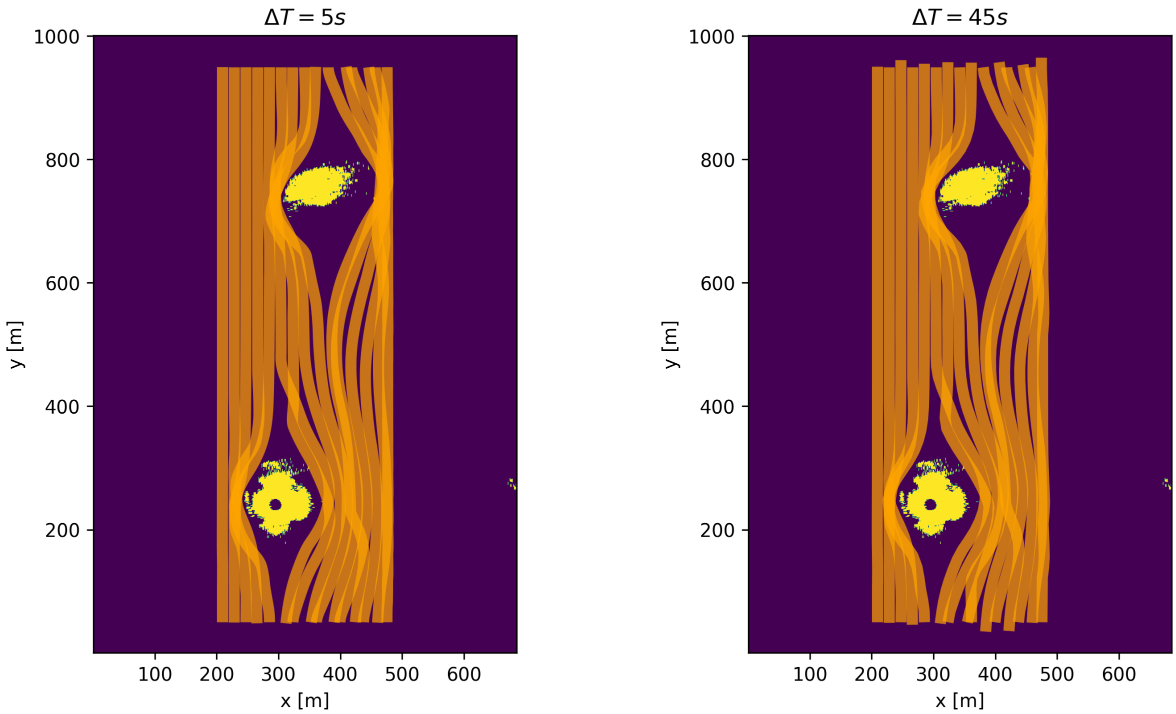

Figure 4.15: Visualization of the driven paths of the collector for a configuration with a low value of ΔT = 5 s on the left, and a high value of ΔT = 45 s on the right. Both use the global orthogonal path proposal method, u_c = 0.4, and $D_{lookahead}$ = 100 m.

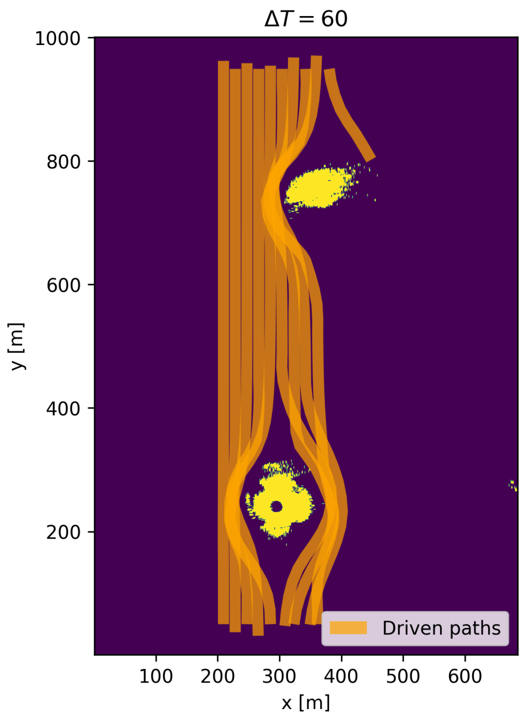

Figure 4.16: Visualization of driven paths of the collector for a configuration where the collector collides with an obstacle due to a large ΔT of 60 seconds. It used the global orthogonal path proposal method, u_c = 0.6, and $D_{lookahead}$ = 100 m

4.4. Experiment 3: Influence of u_c and $D_{lookahead}$

4.4.1. Setup

This experiment aims to assess the performance of ICP parameters $D_{lookahead}$ and u_c. This is done by examining a wide range of values for both of the parameters. Following experiment 1 and 2, the global orthogonal path proposal method is used with a timestep of $\Delta T = 20$ s. The presurvey resolution stays the same at 25 meters.

1. Global orthogonal path proposal method.
2. $\Delta T = 20$ s.
3. $u_c \in \{0, 0.1, 0.2, \ldots, 0.8, 0.9, 1\}$.
4. $D_{lookahead} \in \{50, 75, 100, 125, 150\}$ m.
5. $\rho_{pre} = 25$ m.

Along these parameters, the total area coverage and the mean area coverage per second is calculated and visualized.

4.4.2. Results

As can be seen in figure 4.17, the total area coverage increases with smaller values of $D_{lookahead}$. This can be attributed to the fact that closer proximity of proposed paths allows the collector to execute sharper turns and traverse areas that would otherwise be left unexplored. This can be seen in figure 4.19, where a smaller $D_{lookahead}$ results in paths with more intricate, closer turns, while larger $D_{lookahead}$ exhibits more gradual movements around obstacles, leaving larger unexplored regions. A table with the results can be found in appendix E.

Besides the effect on area coverage, $D_{lookahead}$ also influences the susceptibility to collisions. For a small $D_{lookahead}$ of 50 meters or smaller, the ICP is susceptible to collisions. This phenomenon is further explained in section 4.4.3. Contrary, a large $D_{lookahead}$ of 150 meters or larger makes the ICP also susceptible to collide with obstacles, which is further explained in section 4.4.4.

The impact of changing u_c lies in adjusting the weights of the costs. A higher value of u_c results in more priority being given to following the global path, emphasizing path adherence over production rate, as can be seen in equation 3.9. However, figure 4.18 shows that a lower value of u_c does not necessarily lead to a higher production rate. This counterintuitive outcome can be clarified by examining the cost function and the resulting paths.

Equation 3.3 defines the cost function for calculating the production rate of a path candidate, denoted as C_{nod}. A path candidate that fully covers an already covered area will collect 0 nodules, yielding a C_{nod} of 1. Decreasing u_c places more emphasis on collecting nodules at each instance, prompting the collector to explore every uncovered region of the map. This results in sub-optimal routes, where the driven paths exhibit a lot of lateral movement, diminishing the production rate over the entire map. Conversely, an increased value of u_c results in the collector following the global path more closely. The driven paths for both a small and large u_c can be seen in figure 4.20.

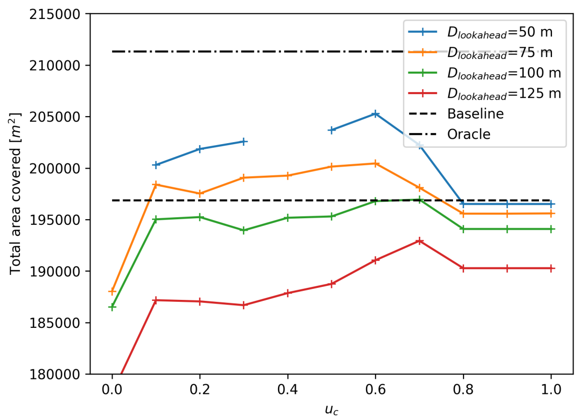

Figure 4.17: Area coverage on test map 1 along several u_c and $D_{lookahead}$, using $\Delta T = 20$ s and path proposal method 2.

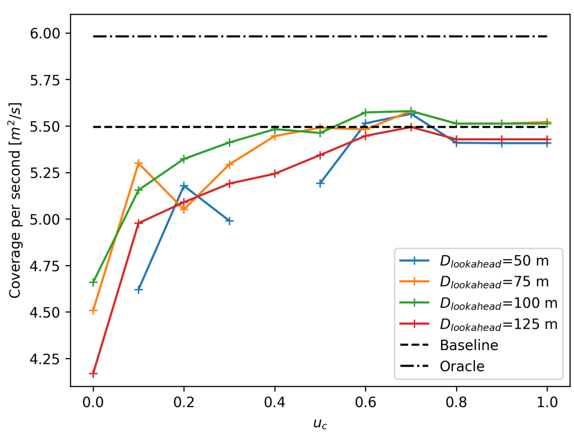

Figure 4.18: Mean area coverage per second on test map 1 along several u_c and $D_{lookahead}$, using $\Delta T = 20$ s and path proposal method 2.

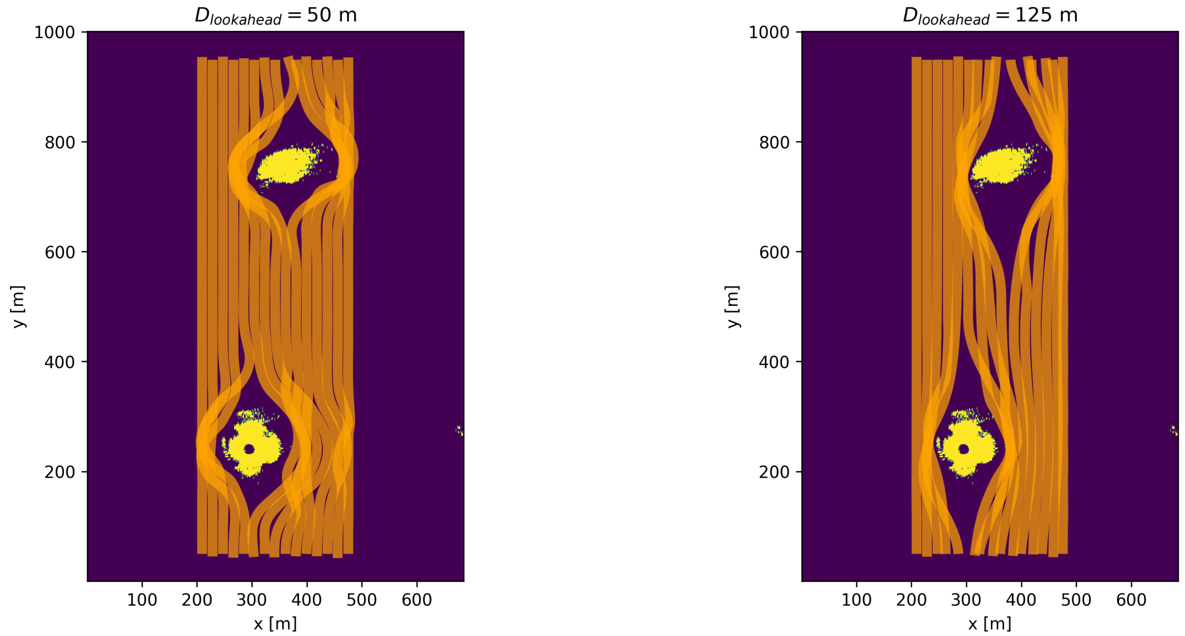

Figure 4.19: The driven paths of the collector with a small $D_{lookahead}$ of 50 meters on the left, and a large $D_{lookahead}$ of 125 meters on the right. Both used the global orthogonal path proposal method, $u_c = 0.6$ and $\Delta T = 20$ s.

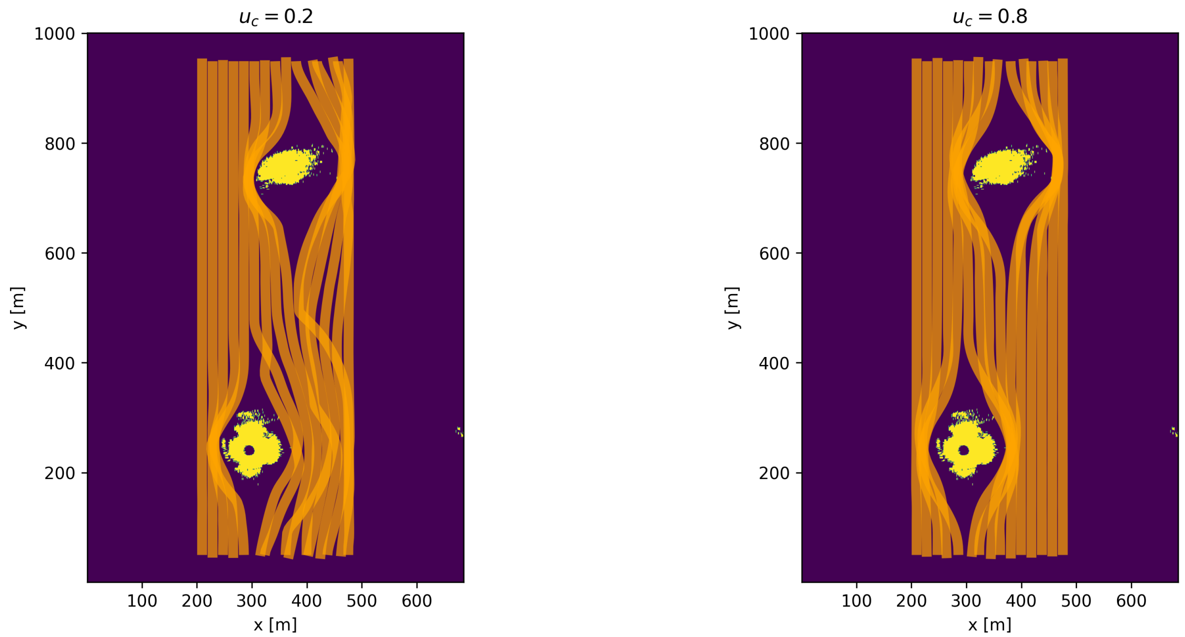

Figure 4.20: The driven paths of the collector with a small u_c of 0.2 on the left, and a large u_c of 0.8 on the right. Both used the global orthogonal path proposal method, $D_{lookahead} = 100$ m and $\Delta T = 20$ s.

4.4.3. Problems with a small $D_{lookahead}$

For a $D_{lookahead}$ of 50 meters or less, the collector has a tendency to collide with obstacles. Because of the small look-ahead distance, the collector occasionally chooses the wrong side of an obstacle to drive towards. An example can be seen in figure 4.21, where the collector chooses to go right of the obstacle, driving itself into a position where it cannot escape from. This example highlights how choosing a small value of $D_{lookahead}$ can lead to collisions.

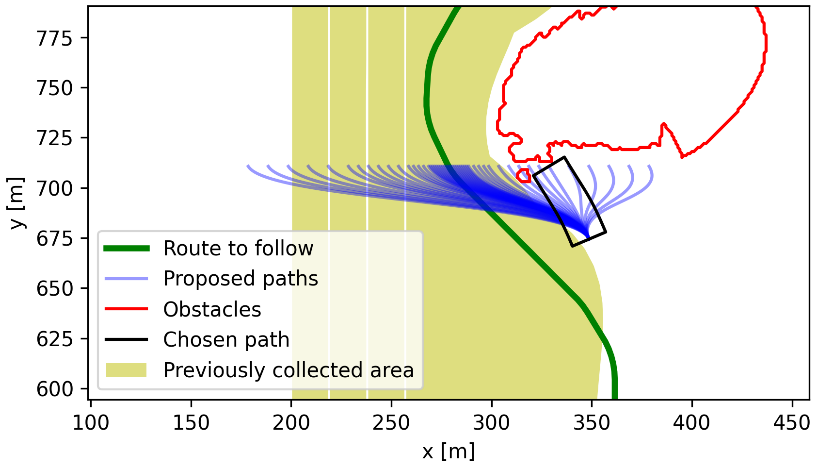

Figure 4.21: Example of a position where the collector chooses to drive towards an obstacle, because the obstacle has not been detected due to the small $D_{lookahead}$.

4.4.4. Problems with a large $D_{lookahead}$

For a $D_{lookahead}$ of 150 meters or larger, the collector also collides with obstacles. This is because, for some combinations of global paths and obstacles, the collector cannot drive around an obstacle. This can be seen in figure 4.22, where all paths collide with an obstacle. It is a limitation of the global orthogonal path proposal method, that paths are proposed only based on 2 points. The global path between the collector and the point ahead is not taken into account, which, for large values of $D_{lookahead}$ and a more complex global path shape, result in collisions. This example illustrates how choosing a large value of $D_{lookahead}$ can lead to collisions.

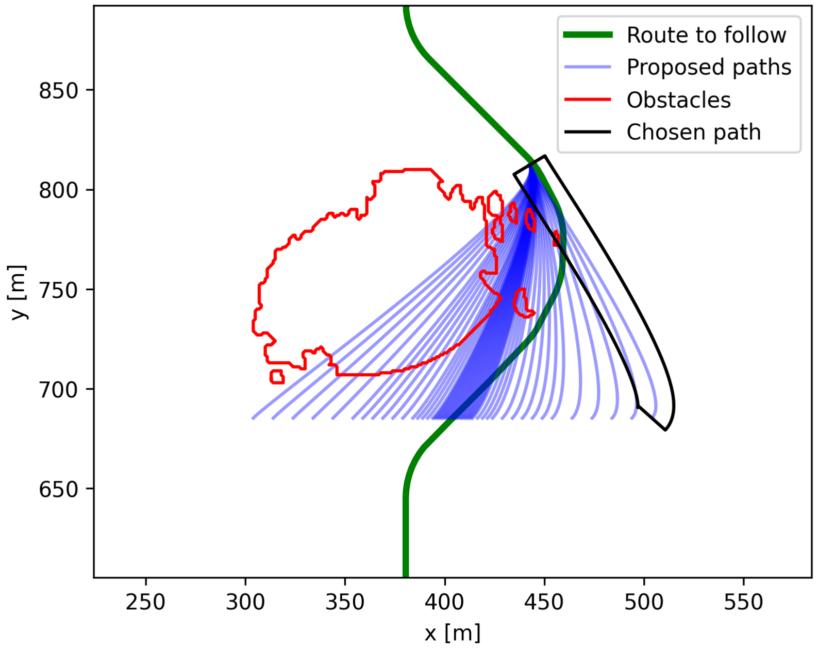

Figure 4.22: Example of a position where the collector cannot evade an obstacle due to the large $D_{lookahead}$.

Driven path by best found solution

Based on the model that covers the most area per second, the best performing solution is chosen to be $u_c = 0.6$, $\Delta T = 20\,\text{s}$, $D_{lookahead} = 100\,\text{m}$ and the global orthogonal path proposal method. A visualization of that configuration's driven path can be seen in figure 4.23. It is used as a basis for the remaining experiments.

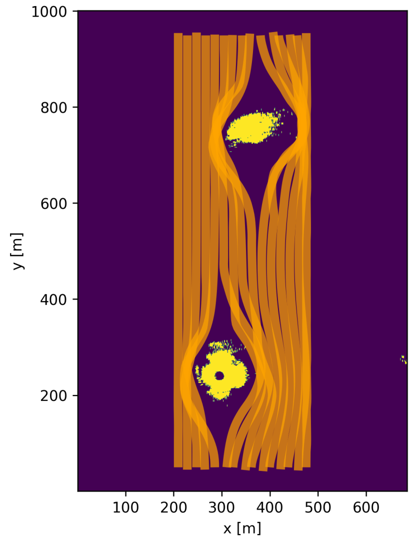

Figure 4.23: Driven path of the best found solution, with $u_c = 0.6$, $\Delta T = 20\,\text{s}$, $D_{lookahead} = 100\,\text{m}$ and the global orthogonal path proposal method.

4.5. Experiment 4: Verification on larger areas

4.5.1. Setup

To assess the performance of the best-identified model, validation is conducted on four larger areas. These areas maintain the same width as the previously utilized map but extend to a length of two kilometers. Selected from the well-measured deep-sea region in the CCZ, the locations of these areas are depicted in figure 4.24.

Detailed views of each area, featuring global paths for two different presurvey resolutions, are presented in figure 4.25 and 4.26. Map one is characterized by a considerable number of obstacles, while map two contains a small amount of obstacles. Map three serves as an extension of the map employed in the initial three experiments, and map four poses a challenge with a path navigating around a very large obstacle. These diverse scenarios are intentionally chosen to evaluate how the path planner navigates and adapts to distinct environmental challenges.

Following from experiments one to three, the chosen configuration for the ICP is described by the following variables: the adoption of the global orthogonal path proposal method, a time increment of $\Delta T = 20$ s, a ratio between the weights of the costs $u_c = 0.6$, and a path proposal distance of $D_{lookahead} = 100$ m. This specific ICP configuration is subsequently tested on the four designated areas, utilizing global paths created from presurvey resolutions $\rho_{pre} \in \{5, 10, 15, 20, 25\}$ m.

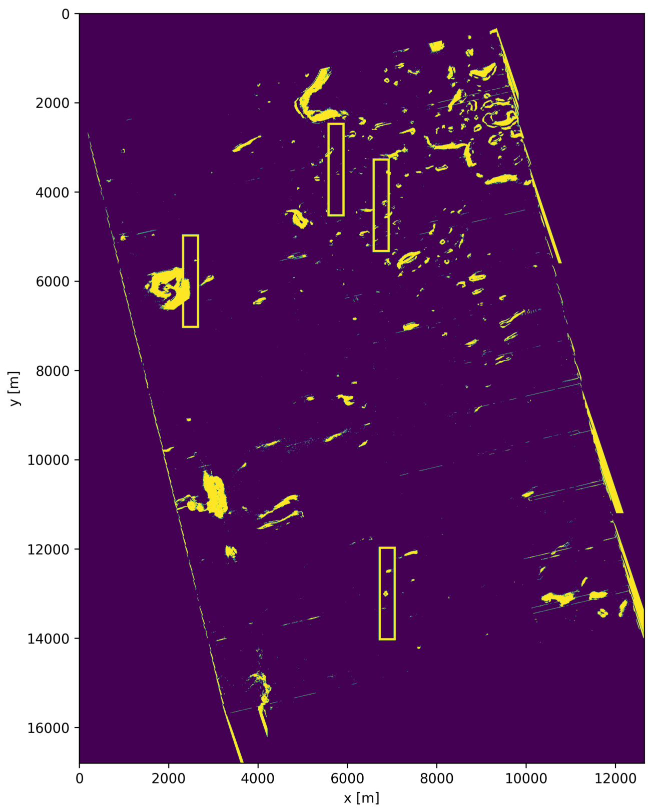

Figure 4.24: Locations of the 4 experiments locations within the full bathymetric map.

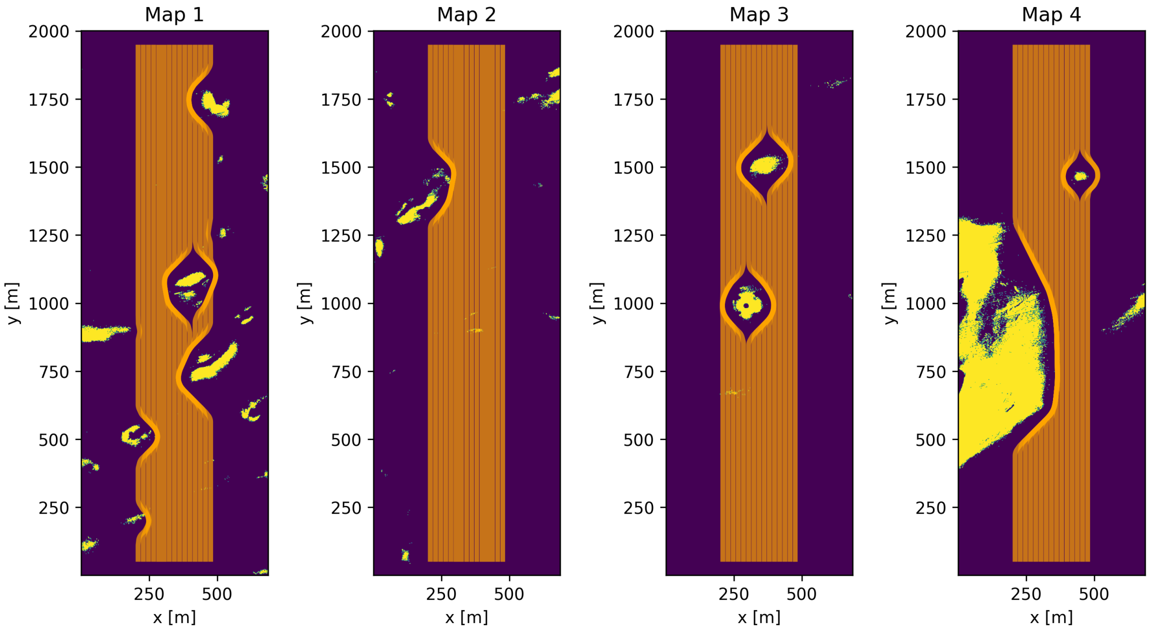

Figure 4.25: Visualization of the global paths of 4 larger test areas, created from a presurvey resolution of 25 meters.

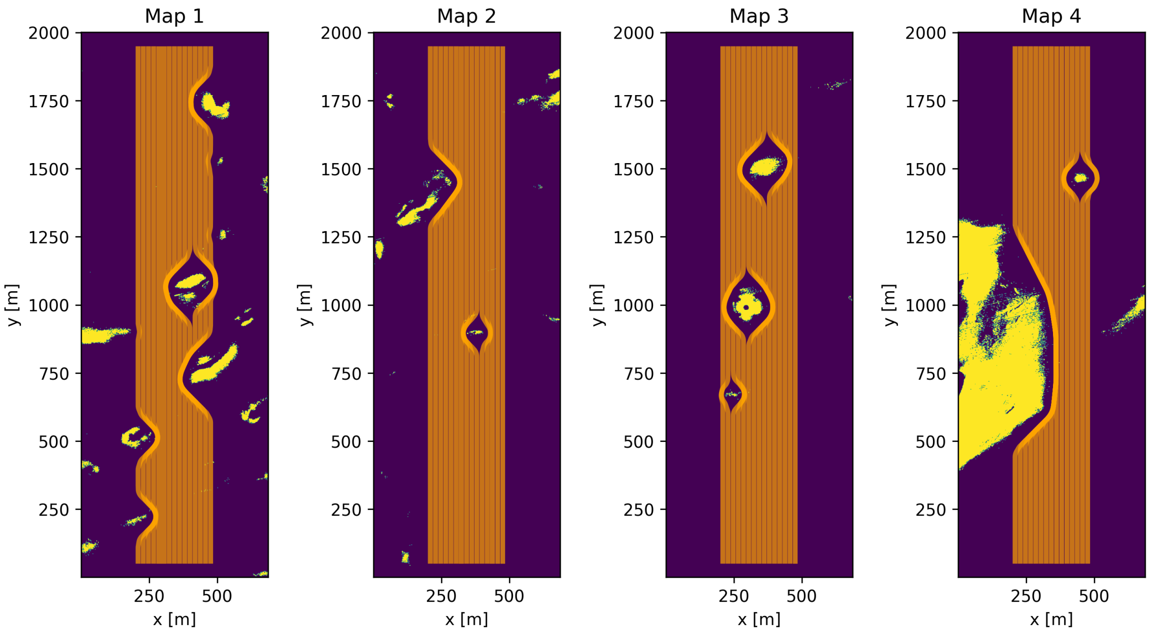

Figure 4.26: Visualization of the global paths of 4 larger test areas, created from a presurvey resolution of 15 meters.

4.5.2. Results

In figure 4.27, the total area coverage on each larger map is visualized as percentage of the oracle performance of each map. Here, it can be seen that the total area coverage does not significantly change along different presurvey resolutions. The total area coverage of all of the configurations stay within 5 percent of the oracle. On test area 4, the ICP even covers more area than the oracle.

Additionally, for each larger test area, the mean area coverage per second relative to the oracle is visualized in figure 4.28. Here, it can be seen that all configurations collect within 7 percent of the oracle. For a presurvey resolution of 5 meters, the performance is even closer to the oracle, achieving a mean production rate of more than 96% of the oracle.

A table with the absolute performance metrics of the four large test areas can be seen in appendix F.

One problem that arises during this experiment is the susceptibility to collisions on some test areas for high presurvey resolutions. As visualized in figure 4.29, the collector collides with obstacles on area 3 and 4 if a presurvey resolution of 25 meters is used. Using a presurvey resolution of 15 meters, the collector safely steers around al obstacles. The reason behind this phenomenon is further examined in section 4.5.3.

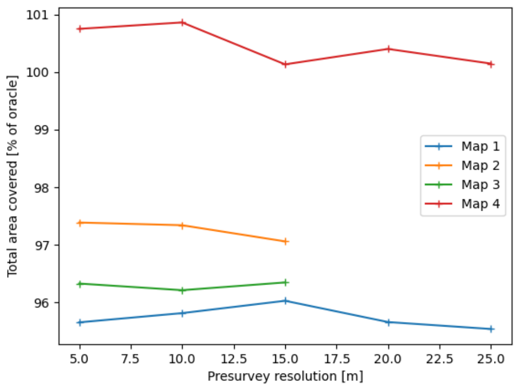

Figure 4.27: Total area coverage along different presurvey resolutions as percentage of the oracle.

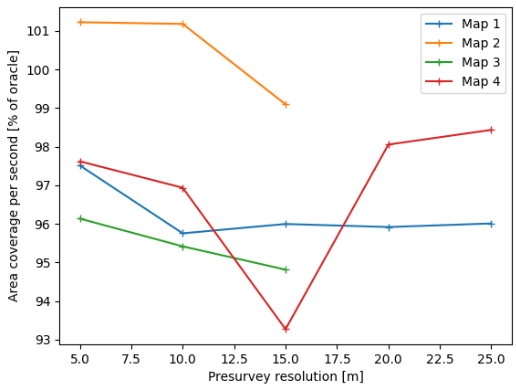

Figure 4.28: Mean area coverage per second along different presurvey resolutions as percentage of the oracle.

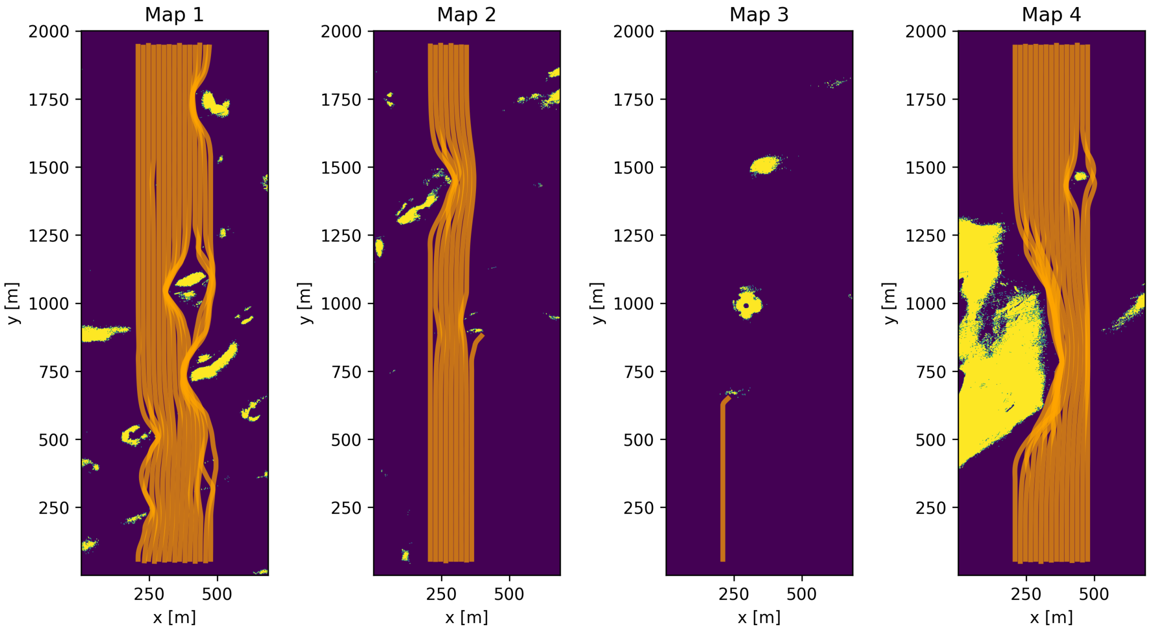

Figure 4.29: Visualization of the driven paths on 4 larger test areas, following the global paths that were created from a presurvey resolution of 25 meters.

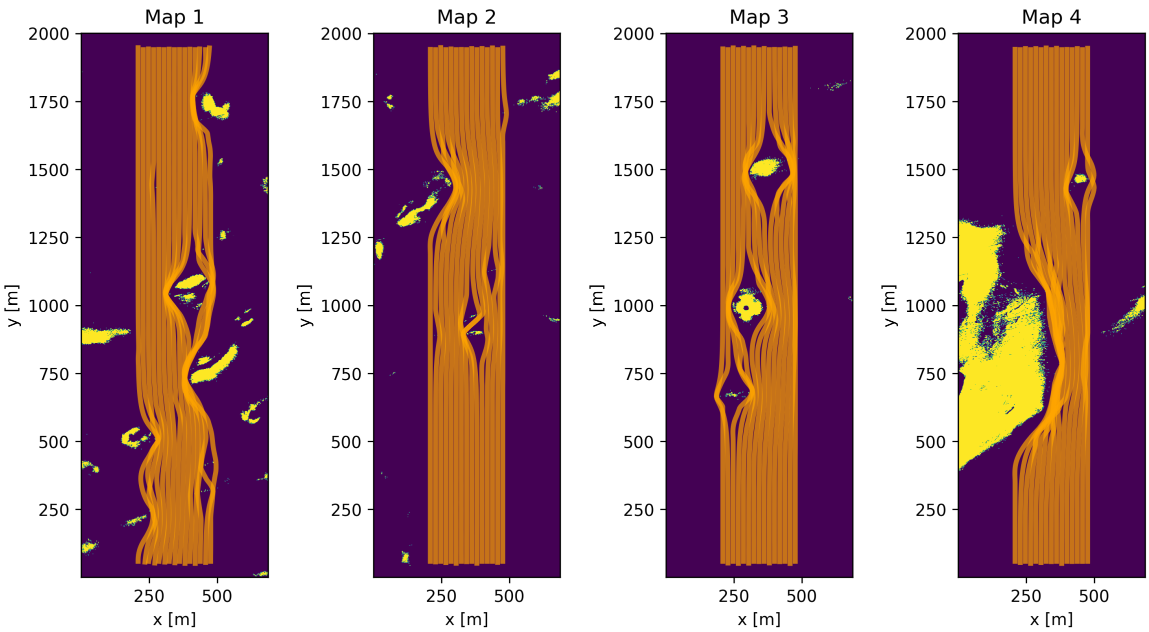

Figure 4.30: Visualization of the driven paths on 4 larger test areas, following the global paths that were created from a presurvey resolution of 15 meters.

4.5.3. Collisions on undetected obstacles

In the case of large test areas 2 and 3, collisions of the collector with an obstacle occurred when employing presurvey resolutions greater than 15 meters. This occurrence can be explained by examining the presurvey map and the global paths created from it.

Figure 4.31 shows the site of the collision on area 2, as measured using a presurvey resolution of 15 meters and of 25 meters. As can be seen, no obstacle is detected with the 25 meter resolution, but the general shape of the obstacle is noted with the better presurvey resolution. The same phenomenon can be seen in figure 4.32.

The detection of the large obstacle is essential for assuring the safety of the collector because of two main reasons. Firstly, the global paths are planned around the obstacle, which creates an incentive for the collector to move in a general direction around it. Secondly, the presurvey map is used as an initial basis for the environment as measured by the collector. When no general shape of the obstacle is detected, the ICP solely relies on the local sensor measurements to decide whether to manoeuvre around the obstacle on the left or right. Given that the local sensor range is only 45 meters, there is very not enough space to avoid an obstacle of the size seen in area two and three.

On area 2, the collector collided with an obstacle with a width of 65 meters, and the obstacle on area 3 had a width of more than 100 meters. Therefore, it can be concluded that obstacles of more than 65 meters wide need to be detected in some way by the presurvey measurements in order to ensure the safety of the collector.

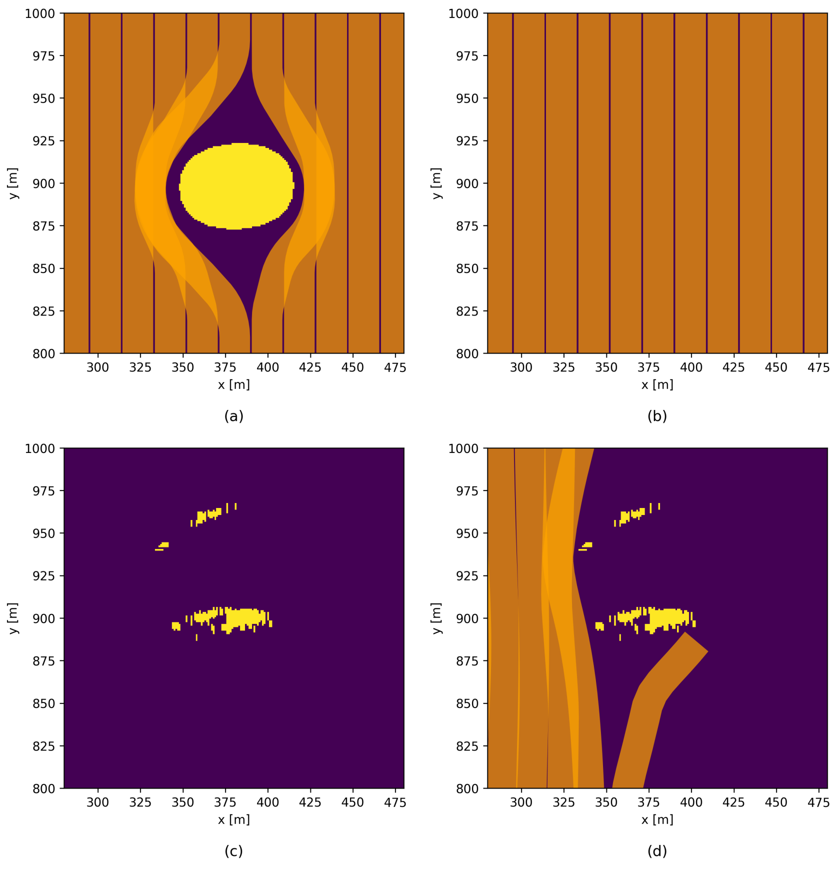

Figure 4.31: Various close-up visualizations of the collision area on large test area 2. (a) shows the presurvey map and the global paths, created using a presurvey resolution of 15 meters. (b) shows the same location, created using a presurvey resolution of 25 meters. (c) depicts the ground truth obstacle map. (d) visualizes the resulting driven path, when a presurvey resolution of 25 meters is used, resulting in a collision.

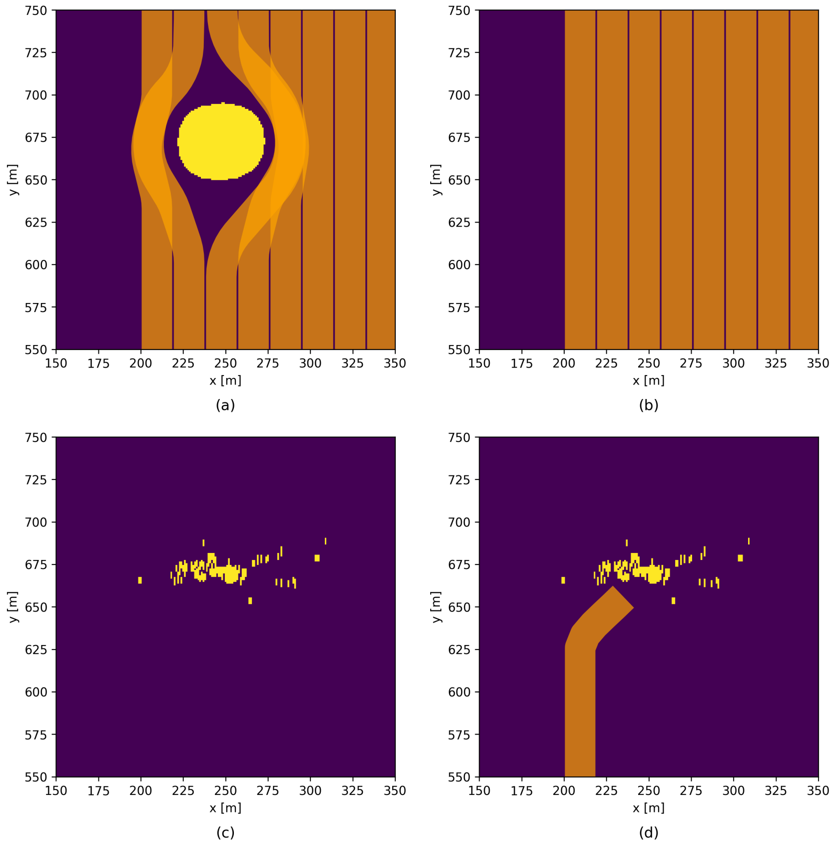

Figure 4.32: Various close-up visualizations of the collision area on large test area 3. (a) shows the presurvey map and the global paths, created using a presurvey resolution of 15 meters. (b) shows the same location, created using a presurvey resolution of 25 meters. (c) depicts the ground truth obstacle map. (d) visualizes the resulting driven path, when a presurvey resolution of 25 meters is used, resulting in a collision.

4.6. Experiment 5: Different environmental noise levels

4.6.1. Setup

Experiments 1 to 4 have been performed with a large amount of environmental noise $N_e(t)$, as T_{noise} was set to 100 seconds, and $T_{noiseless}$ was set to 10 seconds. This was done because it would place more emphasis on the uncertainty of obstacles. However, it also makes it harder for the collector to follow the previous track, as specified in section 3.4.2. This experiments aims to assess the influence of different environmental noise levels approximations $N_e(t)$.

The experiment is performed on the four larger test areas, defined in experiment 4. Three environmental noise levels are compared:

1. High noise level, with $T_{noise} = 100$ s and $T_{noiseless} = 10$ s.
2. Medium noise level, with $T_{noise} = 300$ s and $T_{noiseless} = 300$ s.
3. Low noise level, with $T_{noise} = 0$ s and $T_{noiseless} = 100$ s.

The ICP configuration used in the simulation is the one following the previous experiments. The presurvey resolution ρ_{pre} is set to 5 meters, as it ensures a safe crossing of all test environments, as found in experiment four. This results in the following ICP parameters:

- Global orthogonal path proposal method.
- $\Delta T = 20$ s.
- $u_c = 0.6$.
- $D_{lookahead} = 100$ m.
- $\rho_{pre} = 5$ m.

4.6.2. Results

As can be seen in figure 4.33 and 4.34, the performance of the ICP is better on areas with a high noise level instead of areas with a low noise level. A table with the results can be found in appendix G. This is counterintuitive, and shows a limitation of the ICP model as it is implemented.

As seen in section 3.3.3, low environmental noise level $N_e(t)$ results in two things:

1. Obstacles are detected with higher certainty, and therefore receive a smaller buffer.
2. The previous track is detected, and the path next to the previous track P_{NPT} is used as an input for the ICP.

The first point results in the collector being able to steer more precisely around obstacles, which should increase the total area coverage and increase the mean production rate. However, it results in the opposite. This has to do with the second point.

Using P_{NPT} as an input for the tested ICP model results in both a worse area coverage and a worse area coverage per second. This is because, in the current model, the ICP makes no distinction between following P_{NPT} or the global path P_F. However, in reality, there should be a difference in how both paths are followed. P_G serves as a general direction in which to drive, and deviations from the global path are not of great importance. On the other hand, if the previous track is detected, P_{NPT} should be either be followed without deviations, or not at all. This nuance is not created within the implemented ICP model, and as the best ICP instance is found in test simulations with a lot of noise, it became especially good at following the general direction of P_G, and not at precisely following P_{NPT}.

A visualization of the driven paths in the noiseless environment is given in figure 4.35. As can be seen in the enlarged plots of figure 4.36, the collector still leaves spaces between the tracks, even though the objective is to follow P_{NPT}. The collector shows this behavior, because every path candidate that quickly moves towards P_{NPT} also overlaps with the previous track, resulting in an increased cost C_{nod}. This results in the collector moving extremely slowly towards the P_{NPT}, losing the profit of following the previous track.

Considering both the previous track and a global route is far from a trivial problem. An novel approach was needed to consider them both within the local path planner. Initially, using either P_G or P_{NPT} as input for the ICP seemed like a valid solution. However, from this experiment, it can be concluded that both of the paths should be followed differently, and that they cannot be used interchangeably as input for the ICP.

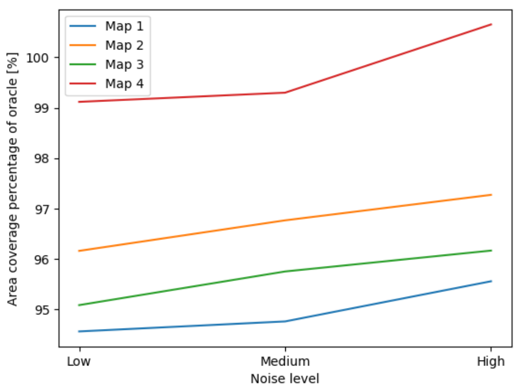

Figure 4.33: Total area coverage for different noise levels as percentage of the oracle performance.

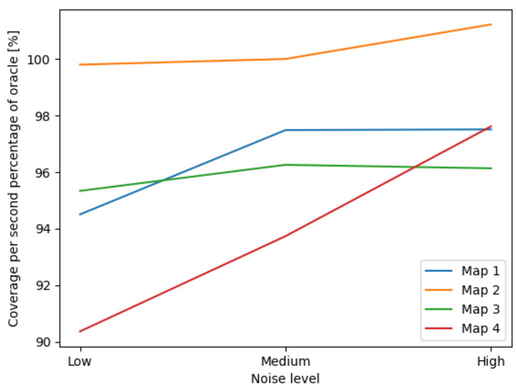

Figure 4.34: Mean area coverage per second for different noise levels as percentage of the oracle performance.

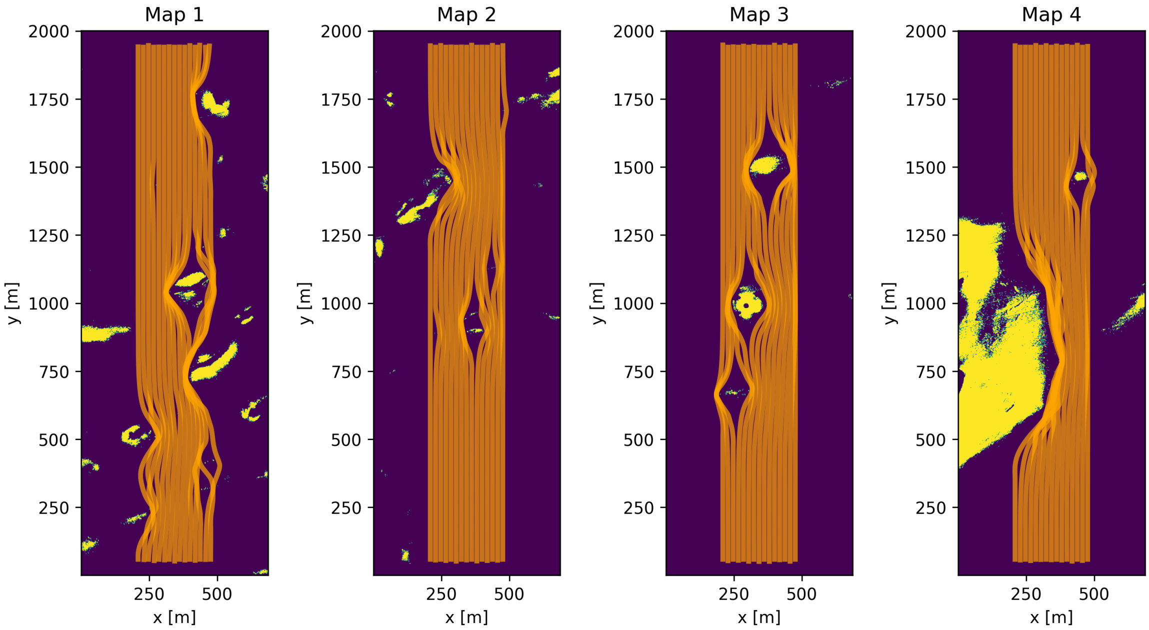

Figure 4.35: Visualization of the driven paths with low environmental noise. T_{noise} = 0 s and $T_{noiseless}$ = 100 s.

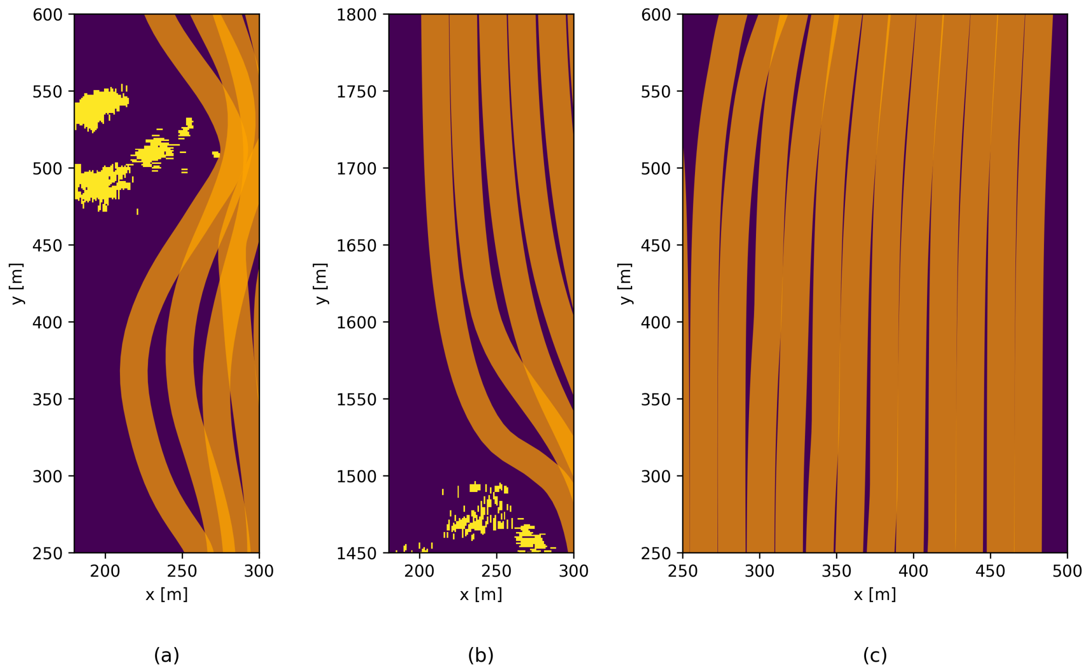

Figure 4.36: Enlarged sections of the driven path in an environment with low environmental noise. (a), (b) and (c) show sections of map 1, 2 and 3, respectively. All of them show space between the tracks, even though the objective is to follow the path next to the previous track.

5 Conclusion

This section will answer the research question and sub-questions as defined in section 1.3. First, each sub-question will be answered individually. Then, the main research question will be answered. Lastly, recommendations for future work are proposed.

What path proposal method is most suitable for an ICP in the context of DSNC?

The utilization of an ICP with a curvilinear path proposal method, as proposed by Chu et al. [5], is deemed unsuitable for DSNC due to one of its inherent limitations. This limitation restricts the collector from deviating from the global path by more than the radius of curvature of the global path. This limitation is less stringent in applications where the environment is better known before operation, as this allows for better global path planning, which results in less deviations by the collector from the global path. However, given the costliness of presurvey measurements, the global path will be far from perfect. This requires the collector to deviate more from the global path than the radius of the global path, resulting in collisions.

Additionally, two simplifications of the curvilinear path proposal method are examined, proposing cubic spline paths based on one point $D_{lookahead}$ meter ahead on the global path. One of these methods, the global orthogonal path proposal method, is found to be the most suitable for creating path candidates for DSNC, as it can allow for large deviations from the global path and can consistently create path candidates that do not collide with an obstacle.

What is the influence of the timestep for an ICP in the context of DSNC?

It is found that the timestep has a negligible effect on the resulting driven path and the total area coverage of a test. However, increasing the timestep makes the collector both susceptible to collisions and decreases the mean area covered per second. Both can be attributed to the fact that a large ΔT reduces the available time to respond to new measurements, as obstacle detection occurs less often. This results in the collector having to steer more abruptly, more often. For $\Delta T \geq 30$ seconds, this phenomenon results in a decreased production rate, and for $\Delta T \geq 60$ seconds, it could result in a collision. A timestep of 20 seconds is chosen for the following experiments.

What is the influence of changing the weights of the cost functions and the path proposal distance on the performance of an ICP in the context of DSNC?

With a smaller path proposal distance $D_{lookahead}$, the total area covered by the collector increases as the collector can execute sharper turns to cover small areas that would otherwise be left unexplored. However, this comes at the cost of a decreased mean area coverage per second. Additionally, a $D_{lookahead} \leq 50$ m and $D_{lookahead} \geq 150$ m makes the ICP more susceptible to collisions.

While a low value of u_c increases the priority given to maximizing production rate at a single timestep, it does not necessarily result in a higher area coverage or mean area coverage per second. Contrary, a larger u_c generally results in a better area coverage per second. The maximum area coverage per second is found to be at $u_c = 0.6$ and $D_{lookahead} = 100$ m.

> What is the performance of an ICP on larger DSNC areas, when different presurvey resolutions are used?

The ICP is tested on four larger test areas, along different presurvey resolutions ranging from 5 meters to 25 meters. Each configuration is compared in terms of area coverage and mean area coverage per second against both the baseline performance of the global path, and the oracle performance. The oracle performance is determined by calculating the performance that the collector could achieve if the exact environment is known before operation.

The total area coverage of each configuration does not change significantly over different presurvey resolutions, and it stays within 5% of the oracle performance of a global path created through a perfect environment. Secondly, there is not a clear correlation found between the presurvey resolution and the mean area coverage per second, and all configurations stay within 7% of the oracle area coverage per second.

The performance of each configuration is comparable with the baseline, which is the performance of the predetermined, imperfect global path. All configurations show a mean area coverage per second of higher than 95% of the baseline, and a total area coverage greater than 97% of the baseline. The ICP does not consistently outperform the baseline, which can be attributed to the fact that the baseline is based on paths that collide with obstacles and are infeasible.

The presurvey resolution does influence if the ICP causes a collision. With a large presurvey resolution, obstacles in the environment can be missed. It is found that the ICP is able to steer the collector safely around small obstacles when they are detected during operation. However, with obstacles wider than 65 meters, the local sensor measurements do not give enough information to safely drive around the obstacle, resulting in a collision. On the performed test areas, all large obstacles are detected with a presurvey resolution of 15 meter or less.

> What is the performance of an ICP on larger DSNC areas, when different simulated environmental noise levels are used?

From an experiment examining different environmental noise levels, it is found that the ICP was not able to increase its performance by using the path next to the previous track P_{NPT} as input path to follow, instead of using the global path P_G. A unique problem of DSNC is that the collector should follow either P_{NPT} or P_G, depending on if the previous track is detected and if the P_{NPT} collides with obstacles. To omit having two path inputs for the ICP, a decision-making method was added to select either P_G or P_{NPT} as input path for the ICP, depending mainly on the simulated environmental noise level. Most experiments have been performed with a high level of noise, resulting in the collector successfully following only P_G. However, when reducing the simulated noise level, the ICP was not able to follow the previous track as closely as intended, due to poorly chosen cost functions that allowed for a less strict following of P_{NPT}. Further research is needed to find a better method of considering P_{NPT}.

> **In the context of deep-sea nodule collection, how does an interpolating curve planner (ICP) perform in terms of reliability, collection rate and area coverage, and how are they influenced by varying presurvey measurement resolutions?**

Within the created simulation environment, it is found that an ICP is able to reliably steer the collector around obstacles, given that obstacles wider than 65 meters have been detected during presurvey. Additionally, using local sensor measurements, the ICP is able to improve the path created from imperfect presurvey measurements. The resulting performance is comparable with the oracle, which is an indication of the performance if the ground truth environment is known before operation. On four large examined test areas, the collector covered more than 95% of the oracle. The mean area coverage per second is found to be at least 93% of the oracle on the four test areas, which could be increased to 96% if the presurvey resolution is reduced to 5 meters.

This research integrates novel production rate objectives, previous track following, and real-time sensor measurements within an environment generated from bathymetric data. By incorporating more realistic objectives and constraints, it extends the limited existing research in path planning for DSNC. The findings of this study show that local path planning has potential as a viable strategy for DSNC operations. It serves as a first step towards optimized nodule collection.

Based on the findings of this research, several recommendations for future studies are proposed:

- Further research is needed to find a superior way of considering the previous track. In the developed model, if the previous track is detected, the path next to the previous track was used as input for the ICP, instead of the global path. It was found that this is not a suitable solution for DSNC, as both paths need to be followed differently. Further research is needed to find a method that can use the previous track to maximize area coverage.
- The cost functions within the ICP could be set up to better represent the DSNC objectives. Different approaches to maximize area coverage, like driving as close to an obstacle as possible, or giving more priority to driving exactly next to the previous track, could have a large impact on the overall performance.
- It would be valuable to perform a deeper study into presurvey measurements, and what kinds of obstacles are detected with different resolutions. The obstacles detected during presurvey greatly influence the performance of the local path planner. However, in this research, a large assumption was made on how the presurvey map is created from the ground truth. If there is a better understanding of which obstacles are detected during presurvey, better decisions can be made on the required resolution of the presurvey measurements.
- While a form of obstacle detection is performed within the created simulator, it could be modeled to be closer to reality. For example, the acoustic shadow behind obstacles is not considered in this study. This phenomenon can be better modeled if the simulation was in a 3D environment. Additionally, in a 3D environment, the sensor uncertainty and environmental noise could be modeled to be more like real life. With a more representational obstacle detection method, the performance of the local path planner will also be more representative of real life.
- An ICP is chosen as the local path planner to be examined in this study. However, it would be valuable to perform a study on different local path planning algorithms. Specifically, a robust local path planning algorithm based on control logic could a valid option. Using control logic, the collector could the determine the direction to drive based on a set of logical statements, which could be tuned to reflect the desired behaviour of the collector. This is also possible within an ICP, but control logic will not be bound by the set of path candidates.
- The pre-determined global path is very important in determining the overall production rate of the collector, but the research for global path planning methods for DSNC is very limited and far from practically usable. While there are methods available to plan global paths in mining patches between obstacles, there is no method to propose a global path that move around obstacles. It would be valuable if an extensive study is performed into setting up valid and profitable global paths.

References

[1] M. A. Atmanand and G. A. Ramadass. "Concepts of deep-sea mining technologies". In: *Deep-Sea Mining: Resource Potential, Technical and Environmental Considerations* (Jan. 2017), pp. 305–343.

[2] G. Calvo et al. "Decreasing Ore Grades in Global Metallic Mining: A Theoretical Issue or a Global Reality?" In: *Resources* 5.4 (Nov. 2016), p. 36. ISSN: 2079-9276.

[3] J. Carsten et al. "Global path planning on board the mars exploration rovers". In: *2007 IEEE Aerospace Conference* (2007).

[4] Y. Cheng et al. "Status and Prospects of the Development of Deep-Sea Polymetallic Nodule-Collecting Technology". In: *Sustainability* 15.5 (Mar. 2023), p. 4572. ISSN: 2071-1050.

[5] K. Chu, M. Lee, and M. Sunwoo. "Local path planning for off-road autonomous driving with avoidance of static obstacles". In: *IEEE transactions on intelligent transportation systems* (2012).

[6] Y. Cong et al. "Underwater robot sensing technology: A survey". In: *Fundamental Research* 1.3 (May 2021), pp. 337–345. ISSN: 2667-3258.

[7] David S. Cronan. "Manganese Nodules". In: *Encyclopedia of Ocean Sciences* (Jan. 2019), pp. 607–614.

[8] R. Danovaro, P. V. R. Snelgrove, and P. Tyler. "Challenging the paradigms of deep-sea ecology". In: *Trends in Ecology \& Evolution* 29.8 (Aug. 2014), pp. 465–475. ISSN: 0169-5347.

[9] R. Danovaro et al. "The deep-sea under global change". In: *Current Biology* 27.11 (June 2017), R461–R465. ISSN: 0960-9822.

[10] S. Erke et al. "An improved A-Star based path planning algorithm for autonomous land vehicles". In: *International Journal of Advanced Robotic Systems* 17.5 (2020).

[11] D. González et al. "A Review of Motion Planning Techniques for Automated Vehicles". In: *IEEE Transactions on Intelligent Transportation Systems* 17.4 (2016), pp. 1135–1145.

[12] B. Guenter and R. Parent. "Computing the arc length of parametric curves". In: *IEEE Computer Graphics* (1990).

[13] J. Hein, A. Koschinsky, and T. Kuhn. "Deep-ocean polymetallic nodules as a resource for critical materials". In: *Nature Reviews Earth \& Environment* 1.3 (Feb. 2020), pp. 158–169. ISSN: 2662-138X.

[14] G. R.T. Jenkin et al. "Ore deposits in an evolving Earth: an introduction". In: *Geological Society Special Publication* 393 (2015), pp. 1–8. ISSN: 03058719.

[15] S. Josef and A. Degani. "Deep Reinforcement Learning for Safe Local Planning of a Ground Vehicle in Unknown Rough Terrain". In: *IEEE Robotics and Automation Letters* 5.4 (Oct. 2020), pp. 6748–6755. ISSN: 23773766.

[16] A.G.N. Kitula. "The environmental and socio-economic impacts of mining on local livelihoods in Tanzania: A case study of Geita District". In: *Journal of Cleaner Production* 14.3-4 (Jan. 2006), pp. 405–414. ISSN: 0959-6526.

[17] T. Kuhn et al. "Composition, formation, and occurrence of polymetallic nodules". In: *Deep-Sea Mining: Resource Potential, Technical and Environmental Considerations* (Jan. 2017), pp. 23–63.

[18] J. C. Latombe. *Robot motion planning*. Springer Science \& Business Media, 2012.

[19] É. Lèbre et al. "The social and environmental complexities of extracting energy transition metals". In: *Nature Communications 2020 11:1* 11.1 (Sept. 2020), pp. 1–8. ISSN: 2041-1723.

[20] D. Leng et al. "A brief review of recent progress on deep sea mining vehicle". In: *Ocean Engineering* 228 (May 2021), p. 108565. ISSN: 0029-8018.

[21] Z. D. Liu et al. "Design of obstacle avoidance controller for agricultural tractor based on ROS". In: *International Journal of Agricultural and Biological Engineering* 12.6 (2019), pp. 58–65.

[22] S. J. Park et al. “A study of sweeping coverage path planning method for deep-sea manganese nodule mining robot”. In: *OCEANS'11 MTS/IEEE KONA* (2011).

[23] D. Paulikas et al. “Deep-sea nodules versus land ores: A comparative systems analysis of mining and processing wastes for battery-metal supply chains”. In: *Journal of Industrial Ecology* 26.6 (Dec. 2022), pp. 2154–2177. ISSN: 1530-9290.

[24] D. Paulikas et al. “Life cycle climate change impacts of producing battery metals from land ores versus deep-sea polymetallic nodules”. In: *Journal of Cleaner Production* 275 (Dec. 2020), p. 123822. ISSN: 0959-6526.

[25] D. Paulikas et al. *Where should metals for the green transition come from?* Tech. rep. Apr. 2020.

[26] L. Paull et al. “AUV navigation and localization: A review”. In: *IEEE Journal of Oceanic Engineering* 39.1 (Jan. 2014), pp. 131–149. ISSN: 03649059.

[27] R. Ponguillo-Intriago et al. “Genetic Algorithm for Solving Coverage Issues in Undersea Mining”. In: *7th International Conference on Engineering and Emerging Technologies, ICEET 2021*. 2021. ISBN: 9781665427142.

[28] X. Shang, J. Zhao, and H. Zhang. “Obtaining High-Resolution Seabed Topography and Surface Details by Co-Registration of Side-Scan Sonar and Multibeam Echo Sounder Images”. In: *Remote Sensing 2019, Vol. 11, Page 1496* 11.12 (June 2019), p. 1496. ISSN: 2072-4292.

[29] C. Shi, Y. Bu, and Z. Li. “Path planning for deep sea mining robot based on ACO-PSO hybrid algorithm”. In: *Proceedings - International Conference on Intelligent Computation Technology and Automation, ICICTA 2008* 1 (2008), pp. 125–129.

[30] Z. Shiller. “Obstacle traversal for space exploration”. In: *Proceedings - IEEE International Conference on Robotics and Automation* 2 (2000), pp. 989–994. ISSN: 10504729.

[31] N. H. Singh and K. Thongam. “Neural network-based approaches for mobile robot navigation in static and moving obstacles environments”. In: *Intelligent Service Robotics* 12.1 (Jan. 2019), pp. 55–67. ISSN: 18612784.

[32] C. R. Smith et al. “Abyssal food limitation, ecosystem structure and climate change”. In: *Trends in Ecology \& Evolution* 23.9 (Sept. 2008), pp. 518–528. ISSN: 0169-5347.

[33] B. K. Sovacool. “The precarious political economy of cobalt: Balancing prosperity, poverty, and brutality in artisanal and industrial mining in the Democratic Republic of the Congo”. In: *The Extractive Industries and Society* 6.3 (July 2019), pp. 915–939. ISSN: 2214-790X.

[34] B. Surewaard. *Obstacle Detection and Collision Avoidance for Deep Sea Bottom Mining*. Delft, Aug. 2021.

[35] H. Wang, J. Kearney, and K. Atkinson. “Arc-length parameterized spline curves for real-time simulation”. In: *Conference on Curves*. 2003, pp. 387–396. ISBN: 0-9728482-0-7.

[36] E. J. Warrant and N. A. Locket. “Vision in the deep sea”. In: *Biological Reviews of the Cambridge Philosophical Society* 79.3 (Aug. 2004), pp. 671–712. ISSN: 14647931.

[37] V. Wiberg et al. “Control of Rough Terrain Vehicles Using Deep Reinforcement Learning”. In: *IEEE Robotics and Automation Letters* 7.1 (Jan. 2022), pp. 390–397. ISSN: 23773766.

[38] W. Xu et al. “A real-time motion planner with trajectory optimization for autonomous vehicles”. In: *2012 IEEE International Conference on Robotics and Automation* (2012).

[39] J. Yuan. “Hierarchical Motion Planning for Multisteering Tractor-Trailer Mobile Robots with On-Axle Hitching”. In: *IEEE/ASME Transactions on Mechatronics* 22.4 (2017), pp. 1652–1662.

[40] K. Zhang et al. “Robot navigation of environments with unknown rough terrain using deep reinforcement learning”. In: *2018 IEEE International Symposium on Safety, Security, and Rescue* (2018).

[41] J. Ziegler and C. Stiller. “Spatiotemporal state lattices for fast trajectory planning in dynamic on-road driving scenarios”. In: *2009 IEEE/RSJ International Conference on Intelligent Robots and Systems* (Dec. 2009), pp. 1879–1884.

[42] L. Zoetmulder. *Developing concepts for the mine planning of deep-sea polymetallic nodules*. Delft, Oct. 2020.

A

Visualization of oracle global paths

The oracle global path is generated by using the global path planning algorithm described in 3.4.1 on the true obstacle map $\mathbf{E}_T$. The resulting paths for the main test area and the four larger test areas can be seen in figure A.1 and A.2. The oracle performance represents the possible performance if the collector starts mining with full and perfect knowledge of the environment.

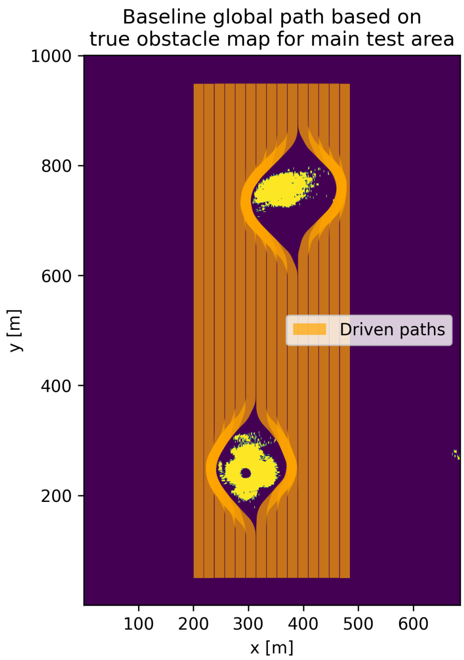

Figure A.1: Oracle global path on the main test area

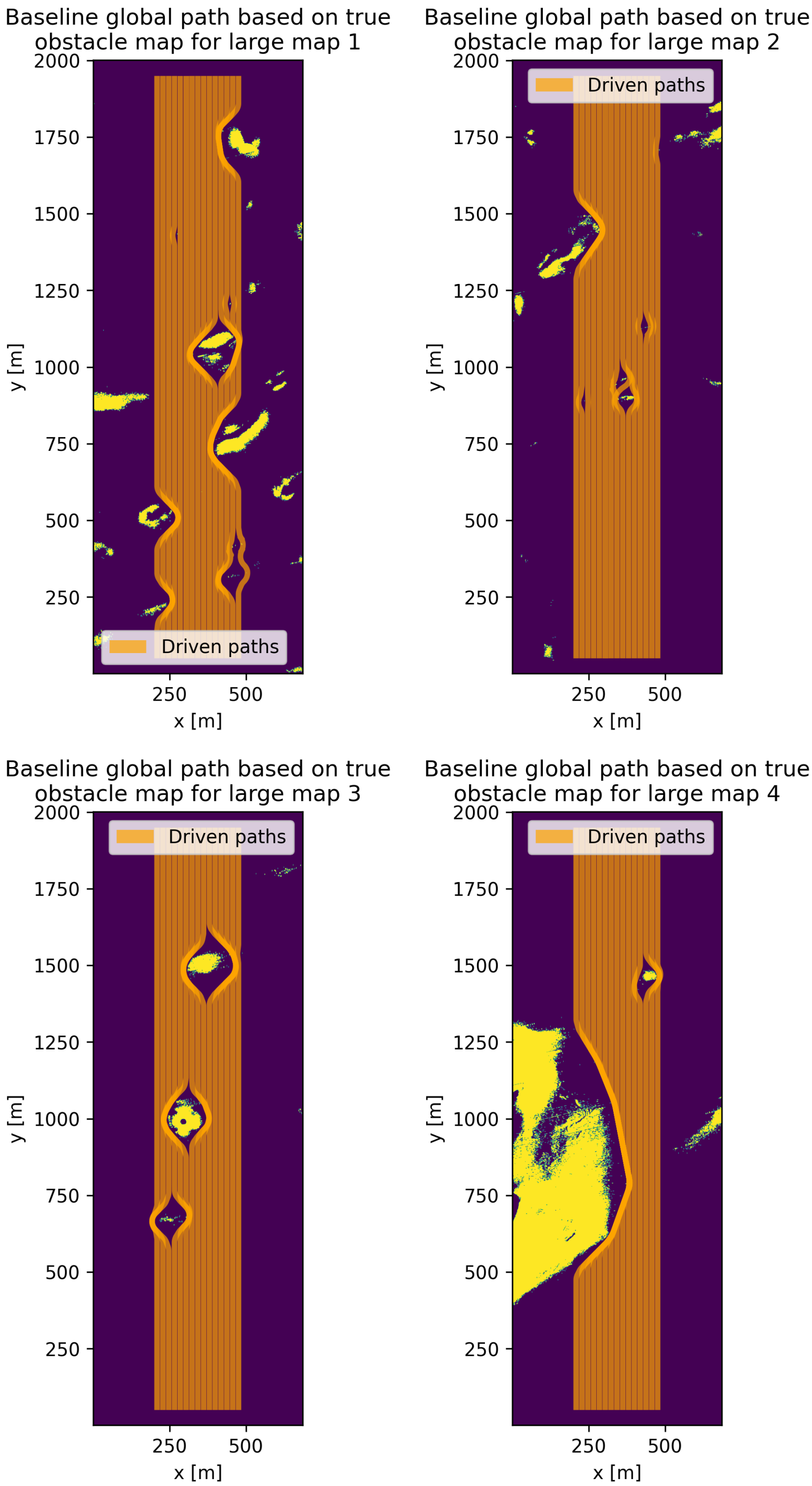

Figure A.2: Oracle global paths for the four large test areas.

B
System structure

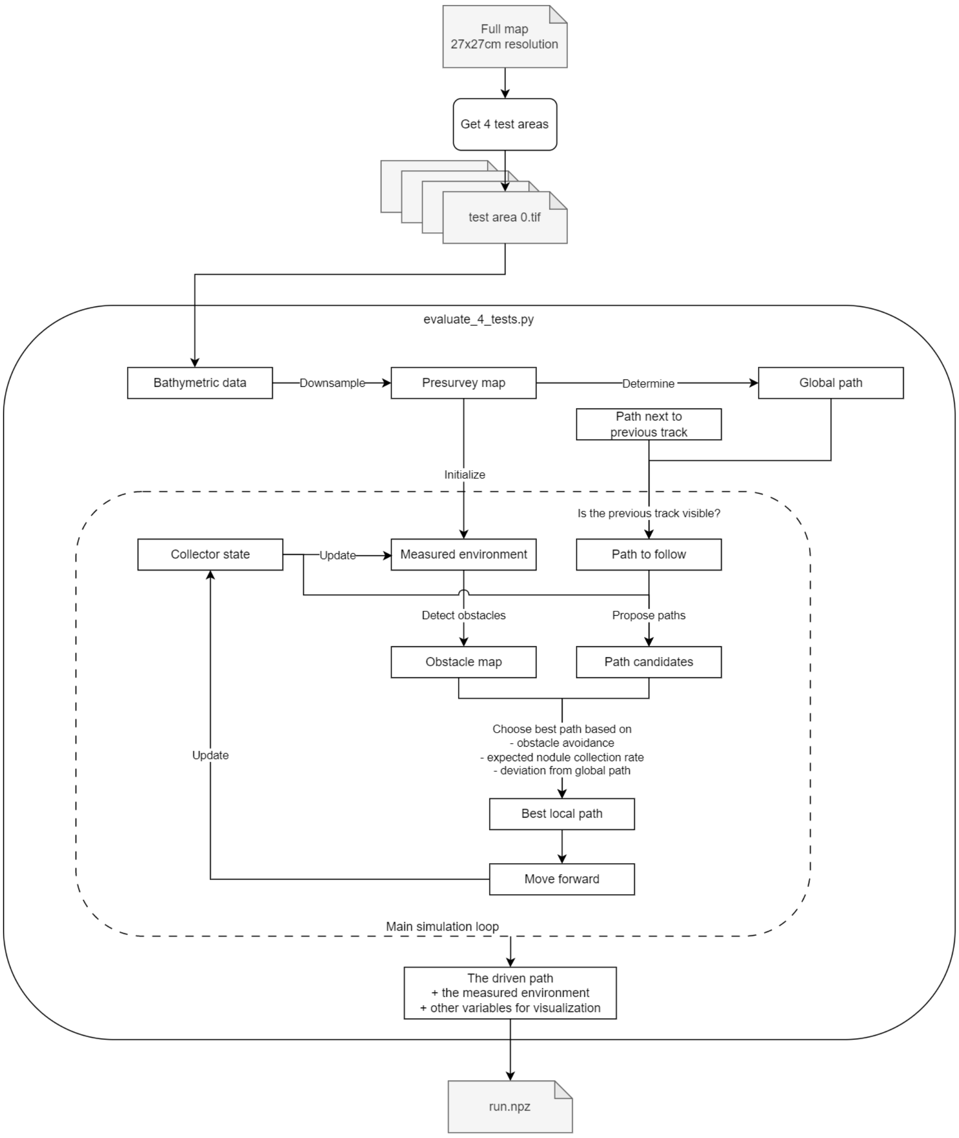

Figure B.1: System and file structure and overview of the main simulation loop.

C

Table results experiment 1

The tested path proposal methods are the local orthogonal (L. O.), global orthogonal (G. O.) and curvilinear (C.) path proposal methods. They are further defined in section 3.2.

u_c	ΔT	$D_{lookahead}$	Path proposal method	Collision	Total area coverage [m^2]	Total time [s]	Mean area coverage per second [m^2/s]
0.4	20	75	L. O.	FALSE	197898.3	38260	5.197
0.4	20	75	G. O.	FALSE	199267.7	36800	5.446
0.4	20	75	C.	FALSE	204709.0	38700	5.314
0.4	20	100	L. O.	TRUE	128631.2	21660	5.972
0.4	20	100	G. O.	FALSE	195174.7	35800	5.483
0.4	20	100	C.	FALSE	200193.8	38260	5.260
0.4	20	125	L. O.	TRUE	124537.0	21520	5.817
0.4	20	125	G. O.	FALSE	187859.5	36020	5.243
0.4	20	125	C.	TRUE	132468.6	23200	5.732
0.4	30	75	L. O.	FALSE	199069.1	36780	5.452
0.4	30	75	G. O.	FALSE	200226.6	38100	5.293
0.4	30	75	C.	FALSE	203912.9	38760	5.297
0.4	30	100	L. O.	TRUE	128740.2	21720	5.962
0.4	30	100	G. O.	FALSE	195890.1	36000	5.473
0.4	30	100	C.	TRUE	132620.2	23460	5.682
0.4	30	125	L. O.	TRUE	125082.7	21690	5.804
0.4	30	125	G. O.	FALSE	188155.3	36030	5.263
0.4	30	125	C.	FALSE	197152.2	37710	5.266
0.5	20	75	L. O.	FALSE	198800.9	35940	5.565
0.5	20	75	G. O.	FALSE	200143.5	36640	5.491
0.5	20	75	C.	FALSE	205495.1	37600	5.497
0.5	20	100	L. O.	TRUE	124888.1	21620	5.812
0.5	20	100	G. O.	FALSE	195302.0	35940	5.462
0.5	20	100	C.	FALSE	202688.1	37440	5.433
0.5	20	125	L. O.	TRUE	119923.8	21580	5.590
0.5	20	125	G. O.	FALSE	188753.1	35520	5.344
0.5	20	125	C.	TRUE	130230.3	23140	5.651
0.5	30	75	L. O.	FALSE	198831.0	36270	5.518
0.5	30	75	G. O.	FALSE	200093.3	36480	5.518
0.5	30	75	C.	FALSE	204836.8	39270	5.255
0.5	30	100	L. O.	TRUE	124977.1	21750	5.777
0.5	30	100	G. O.	FALSE	195769.7	36000	5.466
0.5	30	100	C.	FALSE	201692.0	37350	5.435
0.5	30	125	L. O.	TRUE	120279.4	21630	5.590
0.5	30	125	G. O.	FALSE	189159.7	35910	5.303

Table C.1 continued from previous page

u_c	ΔT	$D_{lookahead}$	Path proposal method	Collision	Total area coverage [m^2]	Total time [s]	Mean area coverage per second [m^2/s]
0.5	30	125	C.	FALSE	199150.1	37050	5.411
0.6	20	75	L. O.	FALSE	199827.1	35900	5.594
0.6	20	75	G. O.	FALSE	200449.0	36700	5.482
0.6	20	75	C.	FALSE	204331.6	37560	5.469
0.6	20	100	L. O.	TRUE	122940.7	21580	5.728
0.6	20	100	G. O.	FALSE	196789.3	35500	5.573
0.6	20	100	C.	FALSE	202406.4	37080	5.491
0.6	20	125	L. O.	TRUE	118676.2	21520	5.546
0.6	20	125	G. O.	FALSE	191054.3	35240	5.447
0.6	20	125	C.	TRUE	125076.7	23000	5.463
0.6	30	75	L. O.	FALSE	200337.6	36510	5.529
0.6	30	75	G. O.	FALSE	200881.3	36900	5.489
0.6	30	75	C.	FALSE	205328.1	37680	5.489
0.6	30	100	L. O.	TRUE	122948.0	21690	5.699
0.6	30	100	G. O.	FALSE	197080.4	36090	5.499
0.6	30	100	C.	FALSE	202711.1	37260	5.483
0.6	30	125	L. O.	TRUE	119524.2	21660	5.553
0.6	30	125	G. O.	FALSE	191860.1	35640	5.416
0.6	30	125	C.	FALSE	200495.0	36990	5.445

Table C.1: Results of experiment 1.

D

Table results experiment 2

All configurations use the global orthogonal path proposal method, as found in experiment 1.

u_c	ΔT	$D_{lookahead}$	Collision	Total area coverage [m^2]	Total time [s]	Mean area coverage per second [m^2/s]
0.4	5	75	FALSE	199824.1	36265	5.516
0.4	10	75	FALSE	200133.3	36700	5.463
0.4	15	75	FALSE	198983.6	36795	5.424
0.4	20	75	FALSE	199267.7	36800	5.446
0.4	25	75	FALSE	199662.9	37500	5.359
0.4	30	75	FALSE	200226.6	38100	5.293
0.4	45	75	FALSE	199557.7	38070	5.292
0.4	60	75	FALSE	200562.2	38820	5.238
0.6	5	75	FALSE	199332.1	36345	5.489
0.6	10	75	FALSE	199119.7	36230	5.506
0.6	15	75	FALSE	199932.2	36165	5.542
0.6	20	75	FALSE	200449.0	36700	5.482
0.6	25	75	FALSE	199134.0	36900	5.424
0.6	30	75	FALSE	200881.3	36900	5.489
0.6	45	75	FALSE	201419.9	36720	5.518
0.6	60	75	FALSE	201320.3	37920	5.380
0.4	5	100	FALSE	195369.4	35740	5.470
0.4	10	100	FALSE	194912.9	35610	5.485
0.4	15	100	FALSE	195310.2	35655	5.493
0.4	20	100	FALSE	195174.7	35800	5.483
0.4	25	100	FALSE	195573.7	36200	5.429
0.4	30	100	FALSE	195890.1	36000	5.473
0.4	45	100	FALSE	196187.3	36315	5.449
0.4	60	100	FALSE	196614.6	37740	5.293
0.6	5	100	FALSE	196788.5	35470	5.553
0.6	10	100	FALSE	196805.8	35700	5.522
0.6	15	100	FALSE	197048.8	35730	5.528
0.6	20	100	FALSE	196789.3	35500	5.573
0.6	25	100	FALSE	197221.2	35675	5.551
0.6	30	100	FALSE	197080.4	36090	5.499
0.6	45	100	FALSE	197603.8	36945	5.406
0.6	60	100	TRUE	122407.7	22380	5.549

Table D.1: Results of experiment 2.

E

Table results experiment 3

All configurations use the global orthogonal path planning method and $\Delta T = 20$ s, as found in experiment 1 and 2.

u_c	$D_{lookahead}$	Collision	Total area coverage [m^2]	Total time [s]	Mean area coverage per second [m^2/s]
0	50	TRUE	96138.9	17220	5.601
0.1	50	FALSE	200303.3	43580	4.621
0.2	50	FALSE	201854.4	39220	5.178
0.3	50	FALSE	202579.6	40720	4.990
0.4	50	TRUE	134768.2	23180	5.835
0.5	50	FALSE	203690.8	39380	5.192
0.6	50	FALSE	205276.6	37460	5.514
0.7	50	FALSE	202241.5	36500	5.565
0.8	50	FALSE	196513.7	36500	5.409
0.9	50	FALSE	196509.8	36500	5.408
1	50	FALSE	196509.8	36500	5.408
0	75	FALSE	188036.1	41840	4.508
0.1	75	FALSE	198393.9	37620	5.300
0.2	75	FALSE	197527.6	39280	5.051
0.3	75	FALSE	199066.8	37780	5.293
0.4	75	FALSE	199267.7	36800	5.446
0.5	75	FALSE	200143.5	36640	5.491
0.6	75	FALSE	200449.0	36700	5.482
0.7	75	FALSE	198092.8	35680	5.581
0.8	75	FALSE	195573.9	35680	5.512
0.9	75	FALSE	195573.9	35680	5.512
1	75	FALSE	195596.5	35620	5.521
0	100	FALSE	186522.2	40300	4.659
0.1	100	FALSE	195020.3	38000	5.155
0.2	100	FALSE	195239.8	36860	5.323
0.3	100	FALSE	193953.6	36040	5.411
0.4	100	FALSE	195174.7	35800	5.483
0.5	100	FALSE	195302.0	35940	5.462
0.6	100	FALSE	196789.3	35500	5.573
0.7	100	FALSE	196942.1	35460	5.580
0.8	100	FALSE	194085.3	35400	5.513
0.9	100	FALSE	194085.3	35400	5.513

Table E.1 continued from previous page

u_c	$D_{lookahead}$	Collision	Total area coverage [m^2]	Total time [s]	Mean area coverage per second [m^2/s]
1	100	FALSE	194085.3	35400	5.513
0	125	FALSE	178103.1	42940	4.169
0.1	125	FALSE	187171.9	37800	4.977
0.2	125	FALSE	187053.4	36920	5.090
0.3	125	FALSE	186687.9	36140	5.190
0.4	125	FALSE	187859.5	36020	5.243
0.5	125	FALSE	188753.1	35520	5.344
0.6	125	FALSE	191054.3	35240	5.447
0.7	125	FALSE	192935.7	35300	5.494
0.8	125	FALSE	190278.4	35220	5.428
0.9	125	FALSE	190278.4	35220	5.428
1	125	FALSE	190278.4	35220	5.428
0	150	TRUE	121133.4	25040	4.868
0.1	150	TRUE	127982.9	22340	5.753
0.2	150	TRUE	126433.5	22340	5.694
0.3	150	TRUE	124543.4	22240	5.632
0.4	150	TRUE	121208.0	22160	5.504
0.5	150	TRUE	116899.0	22080	5.328
0.6	150	TRUE	115878.5	22200	5.248
0.7	150	TRUE	115175.0	21980	5.275
0.8	150	TRUE	113389.7	22060	5.166
0.9	150	TRUE	113389.7	22060	5.166
1	150	TRUE	113389.7	22060	5.166

Table E.1: Results of experiment 3.

F

Table results experiment 4

As determined in experiments 1 to 3, the ICP uses the following configuration:

- Global orthogonal path proposal method.
- $\Delta T = 20$ s.
- $u_c = 0.6$.
- $D_{lookahead} = 100$ m.

Test area	Performance	Presurvey resolution [m]	Collision	Total area coverage [m^2]	Total time [s]	Mean area coverage per second [m^2/s]
1	Oracle	0	FALSE	458274.6	75987	6.031
1	Driven	5	FALSE	438344.9	74600	5.881
1	Baseline	5	FALSE	439551.6	75489	5.823
1	Driven	10	FALSE	439080.2	76100	5.775
1	Baseline	10	FALSE	449251.5	73995	6.071
1	Driven	15	FALSE	440063.0	76060	5.789
1	Baseline	15	FALSE	448545.6	74259	6.040
1	Driven	20	FALSE	438368.8	75880	5.785
1	Baseline	20	FALSE	446927.6	74286	6.016
1	Driven	25	FALSE	437815.6	75680	5.790
1	Baseline	25	FALSE	444607.3	74187	5.993
1	Oracle	0	FALSE	497150.8	75159	6.615
2	Driven	5	FALSE	484157.2	72380	6.695
2	Baseline	5	FALSE	488923.1	72561	6.738
2	Driven	10	FALSE	483923.8	72380	6.693
2	Baseline	10	FALSE	487205.7	72534	6.717
2	Driven	15	FALSE	482526.5	73680	6.555
2	Baseline	15	FALSE	490938.8	72462	6.775
2	Driven	20	TRUE	274507.2	40800	6.732
2	Baseline	20	FALSE	496146.9	72102	6.881
2	Driven	25	TRUE	276310.1	40940	6.756
2	Baseline	25	FALSE	497581.5	71685	6.941
1	Oracle	0	FALSE	473618.4	73854	6.413
3	Driven	5	FALSE	456215.8	74080	6.165
3	Baseline	5	FALSE	462251.8	73746	6.268
3	Driven	10	FALSE	455669.9	74540	6.119
3	Baseline	10	FALSE	465505.1	73581	6.326
3	Driven	15	FALSE	456307.2	75120	6.080
3	Baseline	15	FALSE	466468.9	73509	6.346
3	Driven	20	TRUE	11085.3	1540	7.198

Table F.1 continued from previous page

Test area	Performance	Presurvey resolution [m]	Collision	Total area coverage [m^2]	Total time [s]	Mean area coverage per second [m^2/s]
3	Baseline	20	FALSE	469464.0	73200	6.413
3	Driven	25	TRUE	11085.3	1540	7.198
3	Baseline	25	FALSE	466685.5	73278	6.369
1	Oracle	0	FALSE	425268.1	72717	5.848
4	Driven	5	FALSE	428469.5	75140	5.709
4	Baseline	5	FALSE	425267.3	72639	5.855
4	Driven	10	FALSE	428944.0	75760	5.669
4	Baseline	10	FALSE	425165.3	72663	5.851
4	Driven	15	FALSE	425845.1	78140	5.455
4	Baseline	15	FALSE	422831.4	72699	5.816
4	Driven	20	FALSE	426983.3	74520	5.734
4	Baseline	20	FALSE	421275.3	72735	5.792
4	Driven	25	FALSE	425901.2	74040	5.757
4	Baseline	25	FALSE	418960.0	72735	5.760

Table F.1: Results of experiment 4.

G

Table results experiment 5

Among all performed tests, experiment 5 used the following environmental and ICP configuration:

- Global orthogonal path proposal method.
- $\Delta T = 20$ s.
- $u_c = 0.6$.
- $D_{lookahead} = 100$ m.
- Presurvey resolution $\rho_{pre} = 5$ m.

Test area	T_{noise} [s]	$T_{noiseless}$ [s]	Total area coverage [m^2]	Total time [s]	Mean area coverage per second [m^2/s]	Total area coverage, percentage of oracle [%]	Mean area coverage per second, percentage of oracle [%]
1	0	100	433376.6	76260	5.700	94.6	94.5
1	300	300	434283.2	74040	5.879	94.8	97.5
1	100	10	437931.7	74600	5.881	95.6	97.5
2	0	100	478078.7	72580	6.601	96.2	99.8
2	300	300	481086.4	72880	6.615	96.8	100.0
2	100	10	483598.0	72380	6.695	97.3	101.2
3	0	100	450356.2	73840	6.114	95.1	95.3
3	300	300	453514.1	73620	6.173	95.8	96.3
3	100	10	455475.0	74080	6.165	96.2	96.1
4	0	100	421514.6	79900	5.285	99.1	90.4
4	300	300	422288.0	77260	5.482	99.3	93.7
4	100	10	428037.9	75140	5.709	100.7	97.6

Table G.1: Results of experiment 5

H

Experiment: Influence of presurvey resolutions

H.1. Setup

A separate experiment is performed to find the influence of the presurvey resolution. The following environmental and ICP configuration is used:

1. Global orthogonal path proposal method.
2. $\Delta T = 20$ s.
3. $u_c = 0.6$.
4. $D_{lookahead} = 100$ m.
5. $T_{noise} = 100$ s, $T_{noiseless} = 10$ s.
6. $\rho_{pre} \in \{5, 10, 15, 20, 25, 30, 35, 40, 45, 50\}$ m.

This experiment has been moved to the appendix, as experiment 4 tests the same parameter influence, but on more larger test areas.

H.2. Results

With a more accurate presurvey resolution, the global path can be planned slightly better, generally resulting in a slightly better area coverage, which is visible in figure H.1. However, as can be seen in figure H.2, the decline in area coverage per second is inconsistent over the presurvey resolutions. Based on this experiment, there is no clear correlation found between presurvey resolution and mean area coverage per second.

A visualization of the global paths for two different resolutions can be seen in figure H.3 and H.4. The resulting paths for the two different resolutions can be seen in figure H.5 and H.6.

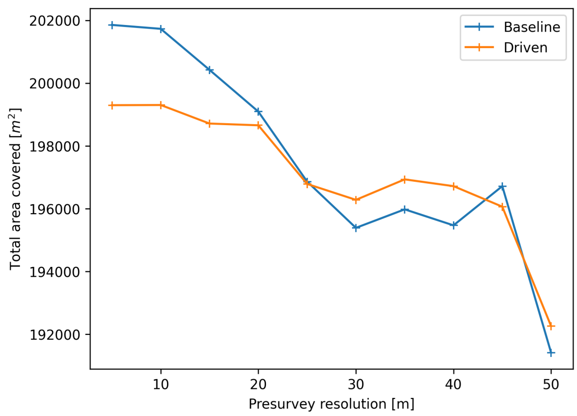

Figure H.1: Total area coverage of the global path and the driven path along several presurvey resolutions.

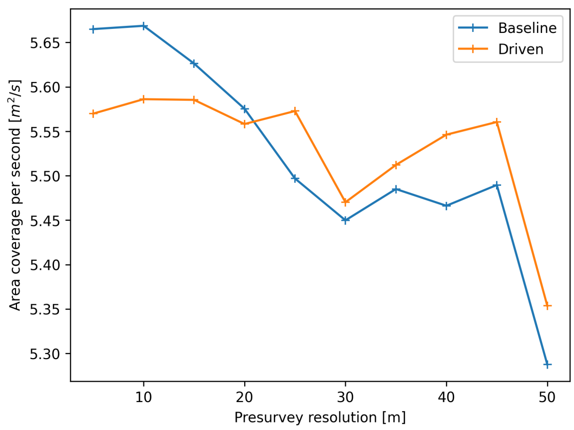

Figure H.2: Mean area coverage per second of the global path and the driven path along several presurvey resolutions.

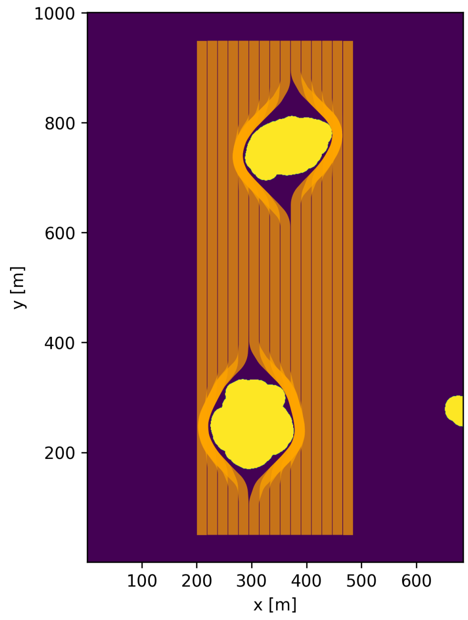

Figure H.3: Global paths with a presurvey resolution of 5 m

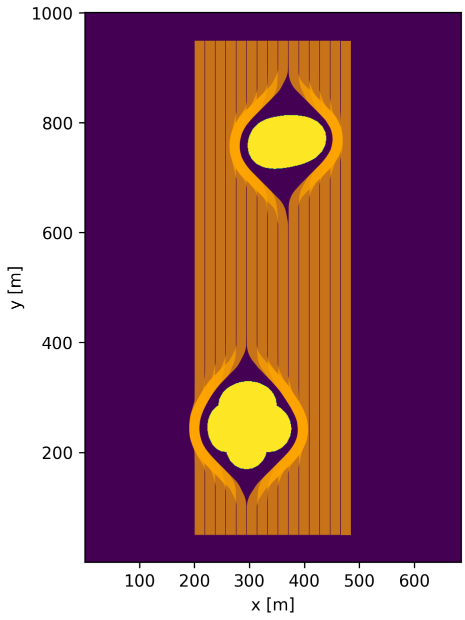

Figure H.4: Global paths with a presurvey resolution of 45 m

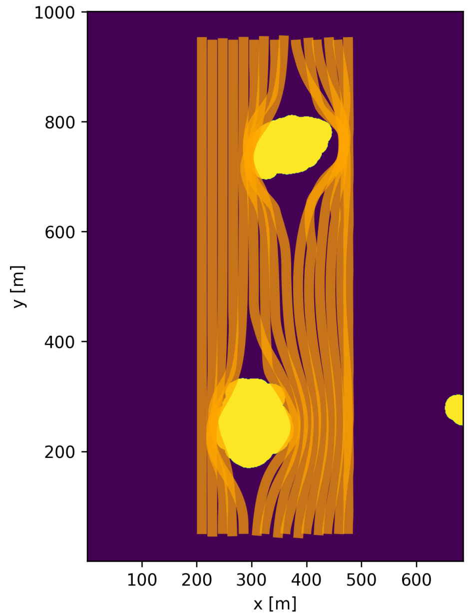

Figure H.5: Driven paths with a presurvey resolution of 5 m

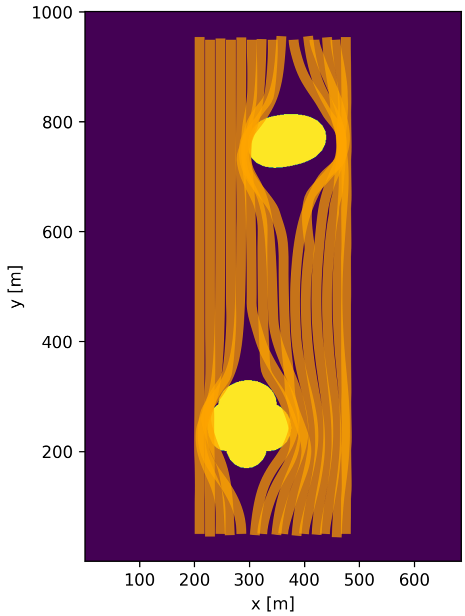

Figure H.6: Driven paths with a presurvey resolution of 45 m